Microscopic modeling of exciton transport in twisted Van der Waals heterostructures

Dissertation
zur
Erlangung des Doktorgrades
der Naturwissenschaften
(Dr. rer. nat.)

dem

Fachbereich Physiks
der Philipps-Universität Marburg

vorgelegt von

Willy Knorr

aus

Teterow

Marburg, March 22, 2024

Vom Fachbereich Physik der Philipps-Universität als Dissertation angenommen am:
21.02.2024

Erstgutachter: Prof. Dr. Ermin Malic
Zweitgutachter: Prof. Dr. Peter Lenz
Vorsitzende: Prof. Dr. Kerstin Volz

Tag der mündlichen Prüfung: 07.03.2024

Hochschulkennziffer: 1180

Contents

1

Introduction

In recent years, the exploration of transition metal dichalcogenides (TMDs) has emerged as a focal point in condensed matter physics, owing to their unique properties that make them intriguing candidates for diverse applications [1, 2]. TMDs, belonging to the family of two-dimensional nanomaterials, have demonstrated their significance in elucidating fundamental aspects of solid-state physics [3]. Excitons, as fundamental entities in condensed matter physics, play a pivotal role in determining the optical, dynamic, and transport properties of TMDs [4–7].

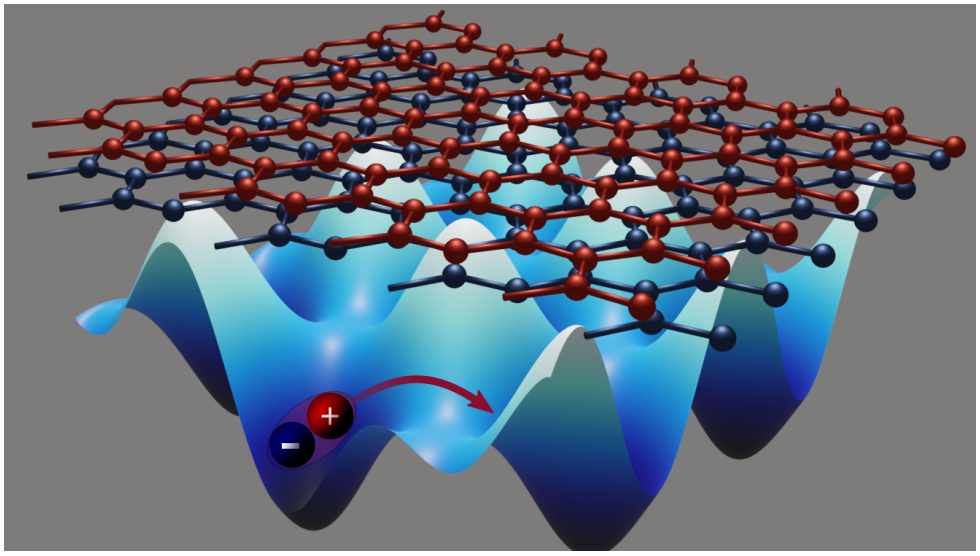

Figure 1.1: A schematic representation of two twisted monolayers, with the resulting moiré potential illustrated as the surface below. Excitons have the ability to move within this potential, transitioning between the minima depending on the twist angle.

The study of TMD monolayers, particularly their exciton propagation behavior un-

der various conditions such as strain and dielectric engineering, has opened avenues for tunable exciton transport, unveiling phenomena ranging from spatial rings (halos) to non-classical diffusion and even effective negative diffusion [8–20].
However, the true marvel lies in the exploration of van der Waals heterostructures formed by vertically stacking TMD monolayers. These heterostructures present a rich exciton energy landscape (see Fig 1.1), tunable through the twist angle [21–27]. The resulting moiré superlattice exhibits twist-angle-dependent energy landscapes, leading to the formation of trapped exciton states [28, 29]. This moiré physics has become a central focus, offering a platform to study different exciton transport regimes and presenting novel opportunities for technological applications [5, 23, 30, 31].
As this research unfolds, the role of polarons in the context of twisted TMD heterostructures has gained significant attention. Polarons, arising from the efficient coupling of excitons and lattice vibrations (phonons), have the potential to influence exciton transport in TMDs [26, 32–34]. Understanding how polaronic effects alter the band structure and the propagation behavior of moiré excitons, especially in scenarios where flat bands may emerge, is a captivating and essential inquiry [35–37]. This exploration not only deepens our understanding of fundamental solid-state physics but also holds implications for emergent phenomena like superconductivity, magnetism, and topological phases [38–40]. Moreover, the influence of polarons on charge transport, optical absorption spectra, and exciton dynamics could enable new pathways for technological applications of TMD materials [41–43].
This thesis delvs into the realms of TMD materials, exciton physics, moiré phenomena, and the intricate interplay of polarons. By employing theoretical frameworks and computational approaches, we aim to unravel the complexities of exciton transport in TMD van der Waals heterostructures, with a particular emphasis on the impact of moiré physics and the crucial role of polarons. This research is expected to enhance our fundamental understanding of condensed matter systems and possibly open avenues for practical applications utilizing the distinctive properties of TMD materials.

2
Many-Particle Hamilton Operator

The subsequent section outlines the overarching theoretical framework employed throughout this thesis. The first part introduces and examines the many-particle density matrix approach, while the second part centers on the approximations utilized to simplify the mathematical intricacies of the problem. In essence, this framework can be universally applied to model the excitation kinetics of various systems involving interacting electrons, phonons, and photons.

2.1 Generell Introduction

In this chapter, we will introduce various interaction Hamiltonians in second quantization. To establish a solid foundation, it is essential to commence by defining the general second quantization scheme, as elucidated in [44].
We define a single-particle state denoted as $|\alpha\rangle$, characterized by the quantum number α. While we focus on electronic states for upcoming sections, it is important to note that the definition aligns closely with that of bosonic states. The compound index $\alpha = (n\mathbf{k}\sigma)$ encompasses the band index n, momentum vector $\mathbf{k}$ and electron spin σ. The real space representation of this state is established through its projection

$$\Psi_\alpha(\mathbf{r}) = \langle \mathbf{r}|\alpha\rangle \,.$$

Our objective is to determine representations of single-particle operators, as exemplified by the Hamiltonian

$$\mathcal{H} = \sum_i h(\mathbf{r}_i).$$

In our pursuit of these representations, we create these operators by aggregating electronic single-particle contributions, such as those of the free electron Hamiltonian,

which will be examined in the following section. To establish general single-particle operators, we label the single-particle basis for the i-th electron at position $\mathbf{r}_i$ using the state $|\alpha_i\rangle$. This approach enables us to insert identity operators, specifically $\sum_\alpha |\alpha_i\rangle\langle\alpha_i| = 1$. These identity operators ensure that within the remaining Hilbert space, the operators $|\alpha_i\rangle\langle\alpha_i|$ function as the identity, streamlining the representation of single-particle operators. This technique enhances the manipulation and analysis of these operators within the context of many-body quantum systems, facilitating more efficient calculations and investigations. The equation results in

$$\mathcal{H} = \sum_i \sum_{\alpha\beta} \langle\alpha_i| h(\mathbf{r}_i) |\beta_i\rangle |\alpha_i\rangle \langle\beta_i| = \sum_{\alpha\beta} h_{\alpha\beta} a_\alpha^\dagger a_\beta. \tag{2.1}$$

Here, we've defined the matrix elements as

$$\begin{aligned} h_{\alpha\beta} &= \langle\alpha_i| h(\mathbf{r}_i) |\beta_i\rangle = \int d^3 r_i \int d^3 r_i' \, \langle\alpha_i|\mathbf{r}_i\rangle \langle\mathbf{r}_i| h(\mathbf{r}_i) |\mathbf{r}_i'\rangle \langle\mathbf{r}_i'|\beta_i\rangle \\ &= \int d^3 r \Psi_\alpha^*(\mathbf{r}) h(\mathbf{r}) \Psi_\beta(\mathbf{r}). \end{aligned}$$

Additionally, we have introduced creation and annihilation operators $a_m^\dagger / a_m$ which must adhere to the following conditions

$$[a_n, a_m^\dagger]_+ = \delta_{nm}, \qquad [a_n, a_m]_+ = 0.$$

It is worth noting that these operators inherently abide by the Pauli exclusion principle, ensuring that no two fermions can occupy the same quantum state. As a result, this approach underscores that the most general single-particle operators, which preserve particle number conservation, adopt the form of quadratic fermionic operators where the numbers of creation and annihilation operators are in balance.

2.2 Born-Oppenheimer Approximation

In the context of a crystal, the atomic structure involves a complex interplay between electrons and nuclei. While the mass difference implies negligible kinetic energy for the nuclei, completely disregarding the nucleus and, consequently, the electron-nucleus interaction would lead to the disintegration of the entire crystal. Therefore,

it is advantageous to take a closer look at this intricate interplay. For this purpose, we decompose the complete Hamiltonian into [44]

$$\begin{aligned} H &= H_0 + T_n(\mathbf{P'}) \qquad \text{with} \\ H_0 &= T_e(\mathbf{p'}) + V_{e-e}(\mathbf{r'}) + V_{n-n}(\mathbf{R'}) + V_{e-n}(\mathbf{r'}, \mathbf{R'}). \end{aligned}$$

Here, T_i represents kinetic energy, and V_{i-i} denotes various interaction processes, where n and e represents nuclei and electron indices, respectively. We introduce the impulses $\mathbf{p}/\mathbf{P}$ and spatial coordinates $\mathbf{r}/\mathbf{R}$ for electrons and nuclei, respectively. Leveraging the observation that the ions' positions remain nearly stationary, we employ a product ansatz, separating the full wave function

$$\psi(\mathbf{r}, \mathbf{R}) = \xi(\mathbf{R})\phi(\mathbf{r}, \mathbf{R}),$$

into electronic ψ and nuclear ξ parts. Examining the H_0 part of the Hamiltonian, we conclude that the Schrödinger equation associated with H_0 depends solely on the electron position $\mathbf{r}$, while the nuclei act as classical variables denoted by $\mathbf{R}$. Therefore, we stipulate that the electronic part is determined by [44]

$$\Big(T_e(\mathbf{p'}) + V_{e-e}(\mathbf{r'}) + V_{n-n}(\mathbf{R}) + V_{e-n}(\mathbf{r'}, \mathbf{R})\Big)\phi(\mathbf{r}, \mathbf{R}) = E_0(\mathbf{R})\phi(\mathbf{r}, \mathbf{R}). \tag{2.2}$$

Here, we observe that $V_{n-n}(\mathbf{R})$ generates an effective potential originating from the nuclei [44]. By incorporating these considerations into the complete problem, we derive the Schrödinger equation for the nuclei part as follows

$$\Big(E_0(\mathbf{R}) + V_{n-n}(\mathbf{R'}) - V_{n-n}(\mathbf{R}) + T_n(\mathbf{P'})\Big)\chi(\mathbf{R}) = E\chi(\mathbf{R}). \tag{2.3}$$

Please note that we neglect transition matrix elements between different electronic states in this context. Additionally, it is worth emphasizing that in this solution, the eigenvalues $E_0(\mathbf{R})$ can be interpreted as an effective potential arising from the nucleus surrounding electrons.

2.3 Non-Interacting Electron

In scenarios where electron interactions can be neglected, it is advantageous to address the single-particle Schrödinger equation. This equation can be effectively solved

by considering a background potential, which, as per the Born-Oppenheimer approximation (c.f. 2.2), arises from the electric potential generated by the stationary ions

$$H\Psi(\mathbf{r}) = \left(-\frac{\hbar^2}{2m}\Delta^2 + V(\mathbf{r})\right)\Psi(\mathbf{r}).$$

In this context, the symbol m denotes the mass of the electrons, and $V(\mathbf{r})$ signifies the potential that exerts an influence on the electrons. Notably, we assume that this potential exhibits periodicity, denoted as $V(\mathbf{r}+\mathbf{R}) = V(\mathbf{r})$, for all lattice vectors $\mathbf{R}$. This periodicity aligns with the characteristics of a Bravais lattice, which represents a regular arrangement of points in a crystal lattice structure.
In the realm of periodically driven ordinary differential equations, Floquet's theorem holds true. Analogously, for periodic potentials, there exists a theorem known as the Bloch theorem. The Bloch theorem states that in a periodic potential, the wavefunctions of electrons can be expressed as plane waves modulated by periodic functions, and it plays a fundamental role in understanding electronic states in crystalline materials

$$\Psi_{\mathbf{k}}(\mathbf{r}) = e^{i\mathbf{k}\cdot\mathbf{r}}u_{\mathbf{k}}(\mathbf{r}), \qquad u_{\mathbf{k}}(\mathbf{r}+\mathbf{R}) = u_{\mathbf{k}}(\mathbf{r}). \tag{2.4}$$

Here, $\mathbf{k}$ corresponds to the wave vector. In the case of eigenfunctions of H, shifting them by a lattice vector simply adds a phase. Consequently, the probability density of locating the electron at position $\mathbf{r}$ exhibits complete periodicity across the lattice, as the phase vanishes in its modulus

$$|\Psi_{\mathbf{k}}(\mathbf{r}+\mathbf{R})|^2 = |\Psi_{\mathbf{k}}(\mathbf{r})|^2.$$

Utilizing the Bloch theorem in the Schrödinger equation leads to

$$He^{i\mathbf{k}\cdot\mathbf{r}}u_{\mathbf{k}}(\mathbf{r}) = \left(-\frac{\hbar^2}{2m}\Delta^2 + V(\mathbf{r})\right)e^{i\mathbf{k}\cdot\mathbf{r}}u_{\mathbf{k}}(\mathbf{r}), \tag{2.5}$$

where we find ultimately an equation for only the periodic function $u_{n\mathbf{k}}(\mathbf{r})$

$$\left(\frac{\hbar^2}{2m}(-i\Delta + \mathbf{k})^2 + V(\mathbf{r})\right)u_{\mathbf{k}}(\mathbf{r}) = E_{\mathbf{k}}u_{\mathbf{k}}(\mathbf{r}).$$

To ensure the required periodicity of the function $u_{n\mathbf{k}}(\mathbf{r})$, our analysis is confined to an arbitrary elementary cell. Within this finite volume, the hermiticity of the eigenvalue problem results in an infinite series of discrete eigenvalues, $E_{\mathbf{k}}$, for each $\mathbf{k}$ value. These eigenvalues exhibit discrete variations in the quantum number, n, and continuous changes concerning $\mathbf{k}$. Notably, it is possible to choose $E_{\mathbf{k}}$ in a manner that aligns with the periodicity of the reciprocal lattice. These specific eigenvalues are commonly known as the electronic band structure of the solid. In summary, this approach allows us to classify the solutions and corresponding energy levels for individual (non-interacting) electrons within a periodic potential using two quantum numbers, n and $\mathbf{k}$.
Up to this point, we have neglected the spin component of the eigenfunction. However, in the case of electrons, the eigenfunction can be separated into a spin (σ) part and a spatial contribution. When applying these concepts to the second quantization scheme, we arrive at the following result [45]

$$H = \sum_{\mathbf{k},\mathbf{k}',\sigma,\sigma'} \langle \mathbf{k}\sigma | \left(-\frac{\hbar^2}{2m}\Delta^2 + V(\mathbf{r}) \right) |\mathbf{k}'\sigma'\rangle \, a^\dagger_{\mathbf{k}\sigma} a_{\mathbf{k}'\sigma'}.$$

Here, $|\mathbf{k}'\sigma'\rangle = \Psi_{\mathbf{k}}(\mathbf{r})$ represents the Bloch state in the Fock space representation. As the Bloch states form a complete set of orthonormal eigenvectors, we can derive the following expression from Eq.(2.5)

$$\langle \mathbf{k}\sigma | \left(-\frac{\hbar^2}{2m}\Delta^2 + V(\mathbf{r}) \right) |\mathbf{k}'\sigma'\rangle = E_{\mathbf{k}'}\delta_{\mathbf{k},\mathbf{k}'}\delta_{\sigma,\sigma'}.$$

Hence, we arrive at the following expression for the electronic Hamiltonian

$$H_{el} = \sum_{\mathbf{k}\sigma} E_{\mathbf{k}} a^\dagger_{\mathbf{k}\sigma} a_{\mathbf{k}\sigma}. \tag{2.6}$$

It is worth noting that in a crystal, the valley index can play a crucial role in describing electronic behavior. Additionally, in atomically thin bilayers, the layer index becomes significant for understanding the material's properties. Interestingly, all these additional degrees of freedom can be conveniently incorporated into the compound index m. This simplification allows us to obtain consistent and comprehensive results while considering various factors.

2.4 Coulomb Interaction

Expanding upon the preceding section, we will now investigate the implications of electron-electron interactions. The total Hamiltonian is described as follows

$$H = \sum_i \Big(-\frac{\hbar^2}{2m}\nabla_i^2 + V(\mathbf{r}_i)\Big) + \sum_{i<j} \mathcal{V}(\mathbf{r}_i - \mathbf{r}_j). \tag{2.7}$$

In this context, we sum over all electrons denoted by the index i, and the term $\mathcal{V}(\mathbf{r}_i - \mathbf{r}_j)$ signifies the electronic interaction potential between electrons at positions $\mathbf{r}_i$ and $\mathbf{r}_j$. The initial component of the Hamiltonian represents the individual contribution of single particles, which we discussed in the preceding section. However, the second part involves the expected interaction between two electrons. Microscopically, this interaction is primarily governed by Coulomb repulsion, thus referred to as Coulomb elements. In reality, various factors contribute to shaping this interaction, forming an effective electron-electron interaction. One example of such contributions is the strong binding of innermost electrons within an ion. It is indeed justifiable to treat the interaction between a conduction band electron and such an inner shell electron effectively as an interaction between the conduction band electron and the screened ion potential.We will delve further into the subject of screening in Section 2.4.1.
For now, we will once again employ the second quantization scheme. However, in this instance, we need to make slight adjustments to our procedure to accommodate the additional particle. Consequently, we commence with a general two-particle operator that can be disassembled into components that exclusively affect pairs of particles

$$H_{\text{Coul}} = \frac{1}{2}\sum_{i\neq j} \upsilon(\mathbf{r}_i, \mathbf{r}_j).$$

One possible operator is the Coulomb component as introduced in Eq.(2.7). By reintroducing identity operators, we can derive the following

$$H_{\text{Coul}} = \frac{1}{2}\sum_{i\neq j}\sum_{\alpha\beta\gamma\delta} \left\langle \alpha^i \right| \left\langle \beta^j \right| \upsilon(\mathbf{r}_i, \mathbf{r}_j) \left| \gamma^j \right\rangle \left| \delta^i \right\rangle \left| \alpha^i \right\rangle \left| \beta^j \right\rangle \left\langle \gamma^j \right| \left\langle \delta^i \right| .$$

It is essential to highlight that expressions like $\langle \alpha^i | \beta^j \rangle$ should not undergo further simplification due to the inequality $i \neq j$, as these operators operate in separate

Hilbert spaces. Nevertheless, the matrix element can be expressed as follows

$$\upsilon_{\alpha\beta\gamma\delta} = \left\langle \alpha^i \right| \left\langle \beta^j \right| \upsilon(\mathbf{r}_i, \mathbf{r}_j) \left| \gamma^j \right\rangle \left| \delta^i \right\rangle = \int d^3 r_i \int d^3 r_j \psi^*_\alpha(\mathbf{r}_i) \psi_\delta(\mathbf{r}_i) \psi^*_\beta(\mathbf{r}_j) \psi_\gamma(\mathbf{r}_j) \upsilon(\mathbf{r}_i, \mathbf{r}_j)$$
$$= \int d^3 r \int d^3 r' \psi^*_\alpha(\mathbf{r}) \psi_\delta(\mathbf{r}) \psi^*_\beta(\mathbf{r}') \psi_\gamma(\mathbf{r}') \upsilon(\mathbf{r}, \mathbf{r}').$$

Due to the indistinguishability of electrons, we note that the matrix elements are independent of i and j. This independence enables us to derive quadratic operators that conserve the particle number

$$H_{\text{Coul}} = \sum_{\alpha\beta\gamma\delta} \upsilon_{\alpha\beta\gamma\delta} a^\dagger_\alpha a^\dagger_\beta a_\gamma a_\delta. \tag{2.8}$$

Please note that, for the sake of simplicity, in this section, we have employed general compound indices. However, these indices naturally encompass all required quantum numbers, including spin and momentum, for example.

2.4.1 2D Dielectric Screening

In this chapter, we introduce a comprehensive theoretical framework applied consistently throughout this thesis. It consists of two major segments. The first part centers on the many-particle density matrix approach and its discussion, while the second part focuses on the approximations employed to reduce mathematical complexity. Importantly, this framework is versatile, as it can be applied to model the excitation kinetics of diverse systems composed of interacting electrons, phonons, and photons.
The Coulomb interaction matrix element in Eq.(2.8) can be decomposed into two primary components via a Fourier transformation of the interaction potential

$$\upsilon_{\alpha\beta\gamma\delta} = \sum_{\mathbf{q}} \upsilon_{\mathbf{q}} \mathcal{J}_{\alpha\beta}(\mathbf{q}) \mathcal{J}_{\gamma\delta}(-\mathbf{q}).$$

Here, the form factor $\mathcal{J}_{\alpha\beta}(\mathbf{q})$ characterizes the scattering cross-section for a transition from state α to state β under a momentum transfer $\mathbf{q}$. This work primarily considers band-conserving Coulomb processes, requiring the consideration of form factors with

$n_\alpha = n_\beta$. Additionally, we examine the influence of the non-trivial dielectric environment, considering a quasi-two-dimensional layer embedded in a three-dimensional world. The Coulomb potential significantly decays for large momenta $\mathbf{q}$. As such, we focus on cases where $\mathbf{q}$ is much smaller than $\mathbf{G}$ and neglect Coulomb-induced intervalley scattering. The remaining form factor

$$\mathcal{J}_{\alpha\beta}(\mathbf{q}) = \langle \mathbf{k}_\alpha | \, e^{i\mathbf{q}\cdot\mathbf{r}} \, | \mathbf{k}_\beta \rangle \tag{2.9}$$

can be evaluated using the Bloch representation Eq.(2.4) and as shown in Ref.[44] close to symmetry points become

$$\mathcal{J}_{\alpha\beta}(\mathbf{q}) \approx \delta_{\mathbf{q},\mathbf{k}_\alpha - \mathbf{k}_\beta}.$$

One of the fundamental distinctions between monolayers and conventional quasi-2D systems is the confinement of electrons to a 2D plane and the subsequent modification of dielectric screening [10, 46].

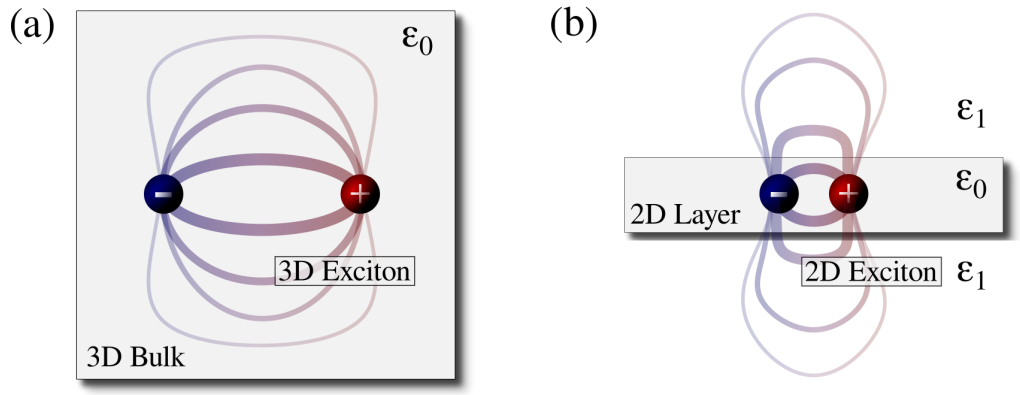

Figure 2.1: Schematic picture of the real-space representation of electrons and holes bound into excitons differs between the three-dimensional bulk (a) and the quasi-two-dimensional monolayer (b)[47]. This contrast is emphasized by differences in the dielectric environment, represented by distinct dielectric constants ϵ_0 within the bulk and ϵ_1 for the surrounding material.

In a bulk system (Fig. 2.1(a)), field lines between attracting charges penetrate the surrounding material, influenced by induced polarization. In contrast, for a 2D system (Fig. 2.1(b)), most field lines penetrate the space surrounding the monolayer, becoming less weakened, especially in a low dielectric environment. Moreover, the

effective Coulomb potential's distance behavior becomes a combination of 2D and 3D components. The potential is obtained through solving the Poisson equation

$$\nabla \cdot \Big(\epsilon(z) \cdot \nabla V(x, y, z - z')\Big) = \frac{e^2}{\epsilon_0}\delta(x, y, z - z').$$

In the subsequent analysis, we make the assumption of point charges localized at the center (z' = 0) of a homogeneous dielectric slab with thickness d [48, 49]. Furthermore, we introduce the concept of permittivity, denoted as $\epsilon(z)$. In this modeling, we consider the slab as having distinct in-plane ($\epsilon_{||}$) and out-of-plane ($\epsilon_{\perp}$) permittivity. The dielectric function of the slab is described using a step-function dependence on z.

$$\epsilon = \begin{cases} \epsilon_L^i & \text{for} \quad |z| \leq d/2 \\ \epsilon_{BG}^i & \text{for} \quad |z| < d/2 \end{cases}$$

Where ϵ_L^i denotes both in- and out-of-plane permittivity of the layer material, whereas ϵ_{BG}^i describes the background material. Utilizing this and ensuring that all boundary conditions for the continuity of the potential and the discontinuity of the gradient are fulfilled give us the following result

$$V_q = \frac{e^2}{2\epsilon_0 \tilde{\epsilon}(q) A q}. \tag{2.10}$$

We employ the following definitions

$$\tilde{\epsilon}(q) = \kappa_L \tanh(1/2(\alpha_L q d - \ln \tilde{\kappa}))$$
$$\tilde{\kappa} = \frac{\kappa_L - \kappa_{BG}}{\kappa_L + \kappa_{BG}} \qquad \kappa_i = \sqrt{\epsilon_i^{||}\epsilon_i^{\perp}} \qquad \alpha_L = \sqrt{\epsilon_L^{||}/\epsilon_L^{\perp}}.$$

For extremely small values of $\alpha_L q d$, the potential can be approximated using the Keldysh potential [48, 49]. The distance dependence of the effective potential undergoes a shift in behavior with varying wave vectors. It displays a 2D character for small wave vectors (associated with large distances) and transitions to a 3D behavior for larger wave vectors (corresponding to smaller distances). Please note that, throughout this work, dielectric constants for TMD monolayers are derived from DFT calculations, as reported in [50].

2.5 Electron-Phonon Interaction

In the endeavor to quantitatively describe lattice vibrations, we commence by conducting an in-depth examination of N mass points, which are representative of atomic nuclei or ions. These intricate dynamics, as prescribed by the rigorous Born-Oppenheimer approximation, are inherently shaped by an effective potential. This potential, in turn, emerges as a consequence of the complex interplay involving the surrounding electrons. When we consider slight deviations from the equilibrium, we can employ a harmonic approximation, which involves truncating the expansion after the quadratic terms. This approximation is valid because, at equilibrium positions, the first-order terms vanish due to the minimization of potential energy. To simplify our description further, we introduce new canonical coordinates Q_s and momenta P_s. By applying an orthogonal transformation to these new variables, we express the Hamiltonian operator in the harmonic approximation, ultimately leading to a diagonal Hamiltonian [44]

$$H = \sum_{i=s}^{f} \left(\frac{1}{2} P_s^2 + \frac{1}{2} \omega_i^2 Q_s^2 \right).$$

Each individual normal mode decouples into f independent, linear harmonic oscillators. The transformed generalized coordinates Q_i and momenta P_i also form canonically conjugate variables, with their commutator relation being

$$[Q_s, P_{s'}] = \delta_{ss'}.$$

Thus, we can immediately introduce creation and annihilation operators

$$b_s = \sqrt{\frac{\omega_j}{2\hbar}} Q_s + \frac{i}{\sqrt{2\hbar\omega_j}} P_s,$$
$$b_s^\dagger = \sqrt{\frac{\omega_j}{2\hbar}} Q_s - \frac{i}{\sqrt{2\hbar\omega_j}} P_s,$$

with $[b_s, b_{s'}^\dagger] = \delta_{ss'}$. In a Bravais lattice, instead of the summation index s, we have the wave vector $\mathbf{q}$ and the branch index j, which includes both acoustic and optical modes. The Hamiltonian operator in the occupation number representation is

$$H_{ph} = \sum_{j} \sum_{\mathbf{q}} \hbar\omega_j(\mathbf{q}) \left(b^{\dagger}_{\mathbf{q}j} b_{\mathbf{q}j} + \frac{1}{2} \right). \tag{2.11}$$

Thus far, our comprehension of solids has revolved around the subtleties of electrons and nuclei, encompassing the intricate task of accounting for electron-electron interactions and electron-nucleus interactions. As elucidated in the discourse on the Born-Oppenheimer approximation (c.f. Sec.2.2), we obtained valuable insights from the substantial disparity in mass between nuclei and electrons. This contrast allowed us to adopt a somewhat independent treatment of electrons and nuclei. Initially, we tackled the electronic Schrödinger equation, incorporating the classical positions of the nuclei as variables. Taking an alternative perspective, as expounded in the previous paragraph, we delved into the notion of an effective electronic potential, accompanied by predefined equilibrium positions for the nuclei situated at the lattice nodes. This approach, when expanded, engendered a harmonic potential governing the behavior of the nuclei. This harmonic potential, in turn, lent itself to quantization through the utilization of bosonic annihilation and creation operators. This pivotal development led us to the concept of phonons, which play a fundamental role in understanding the vibrational dynamics of solids. What remains to be incorporated into this framework is the consideration of deviations in the positions of the nuclei from their designated lattice sites. However, this time, these deviations need to be integrated into the equations governing the behavior of the electrons.
The position of the nth nucleus is expressed as

$$\mathbf{R}_n = \mathbf{R}^0_n + \mathbf{u}_n.$$

The displacement of the nth ion from its equilibrium position is denoted as $\mathbf{u}_n$. These displacements are relatively small, permitting us to perform an expansion of the potential around the equilibrium positions of the nuclei. However, a crucial distinction arises: In the case of the nuclei, our expansion was centered around their own equilibrium positions, leading to the first-order term vanishing. In contrast, for electrons, their equilibrium position does not align with the equilibrium position of the potential they experience. Consequently, the first-order term does not vanish, and it assumes a critical role in mediating the electron-phonon interaction. In detail

this means for the background potential

$$V(\mathbf{r}_i) = \sum_{n=1}^{N} v(\mathbf{r}_i - \mathbf{R}_n^0) - \sum_{n=1}^{N} \Big(\Delta v(\mathbf{r}_i - \mathbf{R}_n^0)\Big) \cdot \mathbf{u}_n + \mathcal{O}(\mathbf{u}_n^2).$$

The first term is already encompassed within the electronic eigenenergies. In contrast, the second part signifies the electron-phonon Hamiltonian in the context of first quantization. We are now equipped to calculate the electron-phonon interaction within the framework of second quantization. The resulting Hamiltonian is as follows

$$H_{el-ph} = -\sum_{n=1}^{N} \sum_{\mathbf{k}\mathbf{k}'\sigma} \langle \mathbf{k}' | \, V_{el-ph}(\mathbf{r}) \, | \mathbf{k} \rangle \, a^\dagger_{\mathbf{k}'\sigma} a_{\mathbf{k}\sigma}.$$

Here, the operators $a_m^\dagger$ and a_m correspond to creation and annihilation operators, respectively. Hence, we must calculate the matrix element of the operator.

$$\langle \mathbf{k}' | \, V_{el-ph}(\mathbf{r}) \, | \mathbf{k} \rangle = \sum_{l=1}^{N} \int d^3 r \Psi_{\mathbf{k}'}(\mathbf{r}) \Big(\Delta v(\mathbf{r}_i - \mathbf{R}_n^0)\Big) \cdot \mathbf{u}_n \Psi_{\mathbf{k}}(\mathbf{r}).$$

We can now map the displacement of the ion to the bosonic operators [44] with

$$\mathbf{u}_n = \frac{1}{\sqrt{N}} \sum_{\mathbf{q}j} \sqrt{\frac{\hbar}{2M\omega_j(\mathbf{q})}} \Big(b_{\mathbf{q}j} + b^\dagger_{-\mathbf{q}j}\Big) \mathbf{e}_j(\mathbf{q}) e^{i\mathbf{q}\mathbf{R}_l^0}.$$

In this expression, M represents the ion mass, and $\mathbf{e}_j$ denotes an eigenvector or polarization vector of branch j. When we substitute these values in the Hamiltonian above, we obtain the following result

$$H_{el-ph} = \sum_{\mathbf{k}\mathbf{q}} \sum_{j\sigma} \mathcal{D}^j_{\mathbf{q}} \Big(b_{\mathbf{q}j} + b^\dagger_{-\mathbf{q}j}\Big) a^\dagger_{\mathbf{k}+\mathbf{q}\sigma} a_{\mathbf{k}\sigma}. \tag{2.12}$$

The equations presented here involve electron-phonon matrix elements, denoted as $\mathcal{D}^j_{\mathbf{k},\mathbf{q}}$. These matrix elements quantify the strength of interaction between an electron with wave vector $\mathbf{k}$ and a phonon with momentum $\mathbf{q}$ in branch j. They play a fundamental role in characterizing the coupling between electrons and lattice vibrations, shedding light on the intricate interplay within condensed matter systems.

2.5.1 Electron-Phonon-Matrix Elements

These matrix elements depend on various factors, including the overlap of wave functions between the initial and final electronic states and the potential arising from the crystal's specific phonon mode oscillations. As a result, their values are influenced by various quantum numbers, including electronic band indices (which, for simplicity, were omitted in the equations above), phonon modes, and valley indices. While it may be feasible to establish simplified parameterizations for specific scattering scenarios, such as intravalley acoustic phonon scattering, accurately modeling electron-phonon interactions across the entire Brillouin zone necessitates the incorporation of parameters derived from rigorous ab initio calculations. To achieve this, we begin by examining the emerging phonon energies. Similar to the electronic band structure, the phonon dispersion is a material-specific feature that can be determined through first principles calculations. The typical shape of the phonon dispersion in TMD monolayers is illustrated along symmetry paths in Figure 2.2. We simplify our treat-

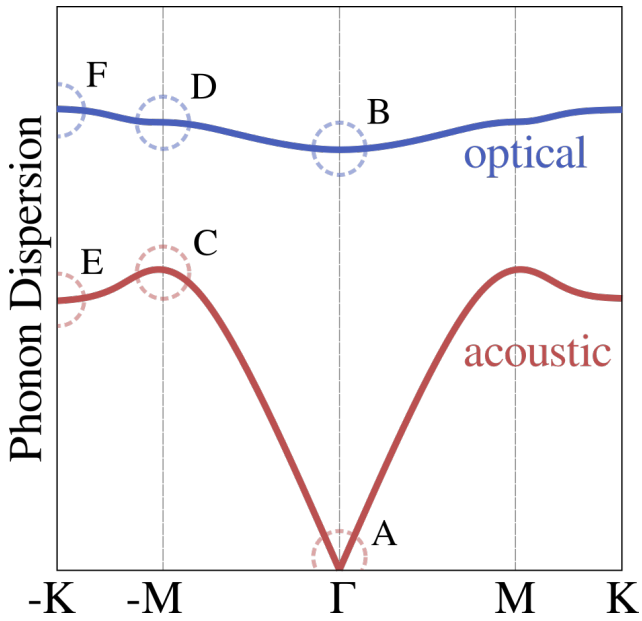

Figure 2.2: Diagram illustrating the typical phonon dispersion of acoustic and optical modes in TMDs, as described in [51]. Notably, in regions around the Γ point (A), a linear (Debye) approximation is applicable, while a constant (Einstein) approximation is reasonable in other regions (B-E).

ment of phonon energies by utilizing a Taylor expansion near high symmetry points. This allows us to include material-specific parameters in the phonon energies, which we naively introduced in the previous sections as $\omega_j^\alpha(\mathbf{q})$, and extend this definition to

$$\omega_j^\alpha(\mathbf{q}) = \begin{cases} c_\alpha \mathbf{q} & \text{for } \alpha = \Gamma \quad \& \quad j = \text{LA,TA} \\ \omega_j^\alpha & \text{else,} \end{cases} \tag{2.13}$$

where we introduced a valley index α, which represents the position along the symmetry points. We approximate long-range acoustic phonons, specifically those in close proximity of the Γ point (see A in Fig.2.2), with a linear dispersion described by sound velocities c_α, following the Debye approximation. On the other hand, we consider for optical modes and short-wavelength acoustic phonons (see B-E in Fig.2.2) constant energies ω_j^α, following the Einstein approximation. In this study, it is important to highlight that we consider both longitudinal and transverse acoustic modes (LA, TA), along with their respective optical modes (LO, TO), and the out-of-plane homopolar optical mode (A1). However, it is worth noting that the discussion of coupling to other out-of-plane modes falls outside the scope of this work. For comprehensive information regarding phonon energies and sound velocities in TMDs, please refer to Ref. [51, 52]
This approach allows us to evaluate the electron-phonon matrix elements. These matrix elements are derived using the deformation potential approximation, which entails a Taylor expansion, often taken to zeroth or first order, of the complete coupling element [51]. These parameters are invaluable for comprehending and predicting a wide array of physical properties within TMDs, especially in the context of electron-phonon interactions, which exert a substantial influence on phenomena such as electrical conductivity and transport. In Ref. [51], the matrix element is expressed as follows

$$\mathcal{D}^j_{\mathcal{K}_i\mathcal{K}_f,\mathbf{q}} \approx \sqrt{\frac{\hbar}{2M\omega_j(\mathbf{q})}}\widetilde{\mathcal{D}}^j_{\mathcal{K}_i\mathcal{K}_f,\mathbf{q}}. \tag{2.14}$$

The matrix element is represented in valley-local coordinates $\mathcal{K}$, which means it is expressed in the vicinity of the high symmetry points. The Taylor expansion we

previously discussed results in the following elements

$$\widetilde{\mathcal{D}}^{j}_{\mathcal{K}_i\mathcal{K}_f,\mathbf{q}} = \begin{cases} \widetilde{\mathcal{D}}^{j}_{\mathcal{K}}\mathbf{q} & \text{for } \mathcal{K}_i = \mathcal{K}_f = \mathcal{K} \quad \& \quad j = \text{LA,TA} \\ \\ \widetilde{\mathcal{D}}^{j}_{\mathcal{K}_i\mathcal{K}_f} & \text{else,} \end{cases}$$

It is important to emphasize that despite expressing the crystal and phonon momentum in these new coordinates, momentum conservation remains intact. Furthermore, it is important to point out that the parameters in [51] do not provide information about the phase or sign of the matrix elements. While the sign of the matrix element is typically inconsequential in electronic considerations, its significance becomes evident when we extend our theory to the excitonic basis, as discussed in Sec. 3.2. In this context, the exciton-phonon matrix element is profoundly influenced by its sign, as it hinges on the disparity between coupling strengths in the valence and conduction bands. To address this issue, we make an assumption that the coupling strength for acoustic modes in Ref. [51] primarily arises from the deformation potential mechanism [53]. Moreover, studies have demonstrated that in TMDs, the deformation potential exhibits opposite signs in the valence and conduction bands [54]. Consequently, the valence band matrix elements for the two acoustic branches are assigned a negative sign due to the opposing shifts of these bands under strain. In contrast, other modes retain their positive matrix elements, as they predominantly couple to electrons via the Fröhlich interaction, which exhibits the same sign in both bands. In Eq.(2.12), it should be noted that we adopted a representation using global coordinates. This particular choice is made in alignment with the primary focus of our work, which pertains to the investigation of transport properties within the K-K valley. Consequently, we have intentionally excluded the valley index $\mathcal{K}$ to streamline our analysis. A more comprehensive discussion regarding this matter will be presented in Section 3.3.

3

Exciton Picture

Excitons, bound electron-hole pairs, play a pivotal role in the optical and electronic properties of semiconductors. Understanding their dynamics and interactions is crucial for advancing various technological applications. In recent years, the exploration of excitonic basis transformations has become a focal point, offering deeper insights into the behavior of excitons in different semiconductor structures [3, 55, 56]. By employing advanced theoretical frameworks and experimental techniques, these studies pave the way for novel approaches in exciton manipulation and control. In this chapter, we will initially outline the intriguing steps involved in transitioning the energy landscape from an electronic framework to an excitonic one. Subsequently, we will leverage these insights to present a free excitonic Hamiltonian and the exciton-phonon Hamiltonian.

3.1 Wannier Equation

In this section, we explore a significant consequence of Coulomb interactions among electrons in semiconductors: the formation of bound states known as excitons, consisting of an electron in the conduction band and a hole in the valence band. To facilitate a qualitative understanding, we begin with a simplified model that focuses on the key aspects of this phenomenon. Our starting point is the general electronic solid-state Hamiltonian operator, which can be constructed by combining the non-interacting electron Hamiltonian with the Coulomb Hamiltonian (see Chapter 2) in second quantization. To simplify our analysis, we make several model assumptions [44]. Firstly, we consider only two bands, namely the valence band and the conduction band. Consequently, the non-interacting part of the Hamiltonian operator can

be expressed as the sum of a valence and a conduction band contribution

$$H_{el} = \sum_{\mathbf{k}} \Big(E^v_{\mathbf{k}} a^\dagger_{v\mathbf{k}} a_{v\mathbf{k}} + E^c_{\mathbf{k}} a^\dagger_{c\mathbf{k}} a_{c\mathbf{k}} \Big). \tag{3.1}$$

In this analysis, we assume that the excited states we aim to determine are spin independent, leading to the omission of the spin index. Secondly, in the context of electron-electron interactions, we concentrate our attention exclusively on interactions taking place between electrons in the conduction and valence bands. We do not take into account interactions among conduction or valence electrons themselves, as articulated in Eq.(2.8). In this context, we incorporate the Coulomb matrix elements introduced in Section 2.4.1. Further simplifying our approach, we later presume the presence of a direct gap at the Γ point (c.f. Fig 3.1 (a)). We describe the band structures near the upper valence and lower conduction band edges in terms of effective masses, leading to specific assumptions about these band structures

$$E^v_{\mathbf{k}} = -\frac{\hbar^2 \mathbf{k}^2}{2m_v}, \qquad E^c_{\mathbf{k}} = E_G + \frac{\hbar^2 \mathbf{k}^2}{2m_c}.$$

Where E_G represent the band gap energies, while m_v and m_c correspond to the respective effective masses. These assumptions provide a foundational framework for understanding excitons in semiconductors, albeit within the boundaries of this simplified model. While this model may not capture all intricate details, it serves as a valuable stepping stone for grasping the fundamental principles underlying exciton behavior. A missing electron with a negative effective mass can also be interpreted as a hole (electron vacancy) with a positive effective mass. A positively charged hole is generated when an electron is annihilated. Therefore, one can define creators and annihilators for holes in the valence band as follows

$$h^\dagger_{\mathbf{k}} = a_{v\mathbf{k}}, \qquad h_{\mathbf{k}} = a^\dagger_{v\mathbf{k}}.$$

The hole operators also obey the standard fermion exchange rules. Holes are, therefore, quasi-particles exhibiting fermionic characteristics, possessing a positive mass m_v, and carrying a positive charge. In the hole picture, the complete model Hamiltonian operator takes the following form [44]

$$H = E_0 + E_G + \sum_{\mathbf{k}} \frac{\hbar^2 \mathbf{k}^2}{2m_v} h^\dagger_{\mathbf{k}} h_{\mathbf{k}} + \sum_{\mathbf{k}} \frac{\hbar^2 \mathbf{k}^2}{2m_c} a^\dagger_{c\mathbf{k}} a_{c\mathbf{k}} - \sum_{\alpha\beta\gamma\delta} v_{\alpha\beta\gamma\delta} h^\dagger_{\mathbf{k}_\delta} h_{\mathbf{k}_\alpha} a^\dagger_{c\mathbf{k}_\beta} a_{c\mathbf{k}_\gamma}. \tag{3.2}$$

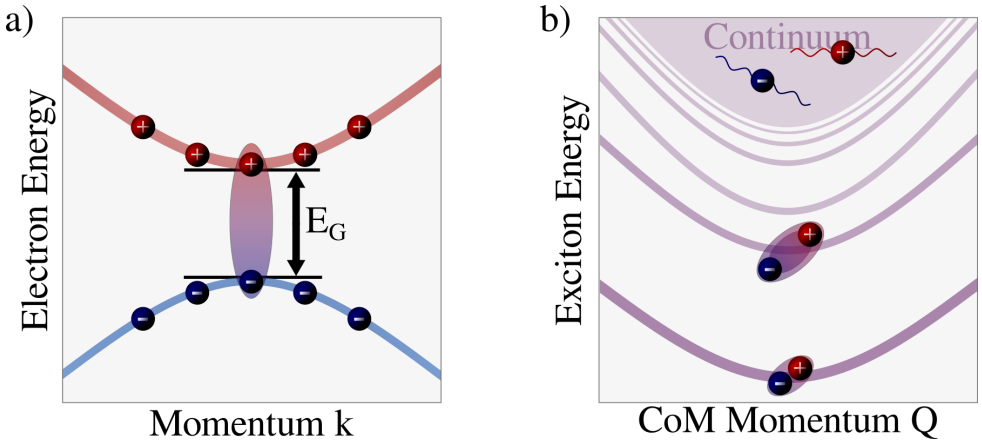

Figure 3.1: Comparison between the exciton in the free electron-hole pair basis (a) and after a basis transformation the excitonic representation (b)

Incorporating the earlier mentioned focus on electron interaction between the conduction and valence bands, we observe that, by applying fermion exchange rules straightforwardly, the originally repulsive Coulomb interaction transforms into an attractive force in the hole picture. This attraction occurs between an electron in the conduction band and a positive hole in the valence band. In the ground state, all valence band states are fully occupied, while all conduction band states remain unoccupied, resulting in a simple ground state energy, denoted as E_0. Excited states arise from the creation of electron-hole pairs, achieved through transitions from the valence to the conduction bands, leading to a superposition of these states. The Schrödinger equation reads

$$H\Psi(\mathbf{k}, \mathbf{k'}) = E\Psi(\mathbf{k}, \mathbf{k'}).$$

Utilizing the Hamiltonian in Eq.(3.2) on these excited states we are able to identify the excitation energy for the non-interaction part

$$\Delta E = E - E_0 = E_c(\mathbf{k}) - E_v(\mathbf{k}') = E_G + \frac{\hbar^2\mathbf{k}^2}{2m_c} + \frac{\hbar^2\mathbf{k'}^2}{2m_v}.$$

In the proximity of the minima and maxima of the conduction and valence bands, the quadratic approximation of their dispersions enables us to distinguish between the relative and center-of-mass motions. As a consequence, we introduce new coordinates

such as

$$\mathbf{Q} = \mathbf{k} - \mathbf{k}'$$
$$\boldsymbol{\kappa} = \alpha\mathbf{k} + \beta\mathbf{k}'.$$

This transforms the eigenvalue problem into relative vectors $\boldsymbol{\kappa}$ and center of mass (CoM) vectors $\mathbf{Q}$, where $\alpha = m_c/M$, $\beta = m_v/M$, and $M = m_c + m_v$. As a result, the equation becomes

$$\Delta E = E_G + \frac{\hbar^2\boldsymbol{\kappa}^2}{2m_r} + \frac{\hbar^2\mathbf{Q}^2}{2M}.$$

Where m_r denotes the reduced mass, with $1/m_r = 1/m_c + 1/m_v$. As the interaction term in Eq. (3.2) is Q-independent, we can decompose the wavefunction into relative and center-of-mass components as $\Psi(\boldsymbol{\kappa}, \mathbf{Q}) = \Phi(\boldsymbol{\kappa})\nu(\mathbf{Q})$. Which leads us to the separate eigenvalue problem including the Coulomb interaction

$$\frac{\hbar^2\boldsymbol{\kappa}^2}{2m_r}\Phi^\mu(\boldsymbol{\kappa}) - \sum_{\mathbf{q}} v_{\mathbf{q}}\Phi^\mu(\boldsymbol{\kappa} + \mathbf{q}) = E_B^\mu\Phi^\mu(\boldsymbol{\kappa}). \tag{3.3}$$

This equation is commonly known as the Wannier equation. It is worth noting that we have introduced the screened Coulomb potential as defined in Eq.(2.10). This equation provides the binding energy, denoted as E_B^μ, for the excitonic state μ, which does not depend on the center-of-mass momentum $\mathbf{Q}$. Nevertheless, this results in the emergence of a new center-of-mass energy for the full Hamiltonian

$$E_{\mathbf{Q}}^\mu = \frac{\hbar^2\mathbf{Q}^2}{2M} + E_G + E_B^\mu. \tag{3.4}$$

Hence, the Coulomb attraction between an electron in the conduction band and a hole in the valence band results in the formation of a novel quasiparticle, known as an exciton. These exciton-bound states (c.f. Fig. 3.1 (b)) exhibit characteristics similar to those of a hydrogen atom [44], rendering excitons akin to hydrogen atoms in certain aspects. Notably, the exciton as a whole can move freely, typically described by its momentum (Q). Consequently, the lower-energy excited states do not consist of quasi-free electrons in the conduction band and quasi-free holes in the valence band.

Instead, due to the Coulomb interaction, there exist lower-energy bound exciton states [44]. Excitons are crucial quasiparticles in solid-state physics, representing elementary electron-hole pairs formed during electronic transitions. Their behavior varies depending on the material while influencing optical and electronic properties.

3.2 Electron-Hole Pair Operator

The foundational step in formulating an excitonic Hamiltonian is the establishment of electron-hole pair operators, designated as $\mathcal{A}$. These operators are constructed from electrons residing in the conduction and valence bands. In order to express intraband transitions, such as $a^\dagger_{c\mathbf{k}\alpha}a_{c\mathbf{k}_\beta}$, in terms of interband operators $\mathcal{A}$, a suitable representation needs to be devised. We find

$$a^\dagger_{c\mathbf{k}_\alpha}a_{c\mathbf{k}_\beta} \Rightarrow \sum_i \mathcal{A}^\dagger_{\mathbf{k}_\alpha i}\mathcal{A}_{\mathbf{k}_\beta i}, \qquad a^\dagger_{v\mathbf{k}_\alpha}a_{v\mathbf{k}_\beta} \Rightarrow \sum_i \mathcal{A}^\dagger_{i\mathbf{k}_\alpha}\mathcal{A}_{i\mathbf{k}_\beta}. \tag{3.5}$$

It is essential to note that the system's many-particle dynamics are intricately linked to the commutation of these operators with the Hamiltonian. Therefore, the choice of operator representation can be adjusted while upholding the fundamental commutation relations that govern the system. Thus, we define our pair operators as

$$\mathcal{A}^\dagger_{\mathbf{k}\mathbf{k}'} = a^\dagger_{c\mathbf{k}}a_{v\mathbf{k}'}$$
$$\left[\mathcal{A}_{\mathbf{k}_\alpha\mathbf{k}_\beta}, \mathcal{A}^\dagger_{\mathbf{k}_\gamma\mathbf{k}_\delta}\right] \approx \delta_{\mathbf{k}_\alpha\mathbf{k}_\gamma}\delta_{\mathbf{k}_\beta\mathbf{k}_\delta}.$$

In this context, we disregard the fermionic substructure of the pair operators, which would typically lead to Pauli blocking. This simplification is justifiable because our current focus is on the low excitation regime [57]. Consequently, we arrive at a fully bosonic system for the commutation of electron-hole excitations.
These pair operators, representing bound electron-hole pairs, or excitons, mark a pivotal step towards the transformation process of the electronic Hamiltonian into the excitonic basis. In this transformation, the intraband Coulomb interaction, which has significance at higher electron densities due to its impact on energy renormalization and electron-electron scattering, is deliberately omitted. This omission is rooted in the understanding that, in the low excitation regime, the intraband Coulomb

interaction's influence on the system's dynamics is minimal. Once the exciton basis is defined, the Hamiltonian is reformulated in terms of excitonic operators, which govern the creation and annihilation of excitons. The specific transformation of pair operators is represented by the equation

$$\mathcal{A}^{\dagger}_{\mathbf{k}\mathbf{k}'} = \sum_{\mu} X^{\dagger}_{\mu,\mathbf{k}-\mathbf{k}'} \Phi^{\mu}(\alpha\mathbf{k} + \beta\mathbf{k}'). \tag{3.6}$$

Where the $\Phi^{\mu}(\alpha\mathbf{k} + \beta\mathbf{k}')$ represent the excitonic eigenmodes, as previously introduced in Eq.(3.3). Inserting this into the Hamiltonian

$$H = H_{\text{el}} \; + \; H_{\text{Coul}} = \sum_{\mathbf{k}} E_{\mathbf{k}} a^{\dagger}_{\mathbf{k}} a_{\mathbf{k}} + \sum_{\alpha\beta\gamma\delta} v_{\alpha\beta\gamma\delta} a^{\dagger}_{\alpha} a^{\dagger}_{\beta} a_{\gamma} a_{\delta}.$$

This transformation allows the Hamiltonian to shift from the electron-based representation to the excitonic basis. We utilize the understanding that the non-interacting portion of the Hamiltonian can be divided into valence and conduction band contributions, as previously illustrated in Eq.(3.1). When the general transformation into pair operators is applied, the Hamiltonian becomes

$$H = \sum_{\mathbf{k}\mathbf{k}'} \Big((E^{c}_{\mathbf{k}} - E^{v}_{\mathbf{k}'}) \mathcal{A}^{\dagger}_{\mathbf{k}\mathbf{k}'} - \frac{1}{2} \sum_{\mathbf{q}} V_{\mathbf{q}} \mathcal{A}^{\dagger}_{\mathbf{k}+\mathbf{q},\mathbf{k}'-\mathbf{q}} \Big) \mathcal{A}_{\mathbf{k}\mathbf{k}'}.$$

It is important to highlight that we have introduced the screened Coulomb potential $V_{\mathbf{q}}$, defined in Eq.(2.10). Employing the expansion introduced in Eq.(3.6), we arrive at

$$H = \sum_{\mathbf{Q}\mu} E^{\mu}_{\mathbf{Q}} X^{\dagger}_{\mu\mathbf{Q}} X_{\mu\mathbf{Q}}. \tag{3.7}$$

Here, $E^{\mu}_{\mathbf{Q}}$ denotes the excitonic energy introduced in Eq.(3.4). Notably, the Coulomb interaction is now entirely encapsulated within the single-particle energy of the exciton. In the electron-based perspective, the Hamiltonian included multi-particle interactions, giving rise to issues related to hierarchy and Coulomb correlations. However, by simplifying the pair operators and neglecting fermionic correction terms, we have effectively transitioned to a single-particle problem while retaining essential insights into the excitonic behavior.

3.3 Exciton Phonon Interaction

By emploing the same transformation procedure we are able to also transform the exciton phonon Hamiltonian into the exciton basis. For that purpose we start form the electron-phonon Hamiltonian we introduce in Eq.(2.12)

$$H_{\text{el-ph}} = \sum_{\mathbf{kq}\lambda j} \mathcal{D}_{\mathbf{q}}^{\lambda j} \Big(b_{\mathbf{q}j} + b_{-\mathbf{q}j}^{\dagger} \Big) a_{\lambda \mathbf{k}+\mathbf{q}}^{\dagger} a_{\lambda \mathbf{k}}.$$

Where we now introduced an electronic band index λ. By leveraging the operator relationships established in Section 3.2, we can now construct operators that take into account the momentum transfer represented by $\mathbf{q}$. This empowers us to articulate the impact of phonon interactions on our systems using these operators, facilitating a deeper and more thorough comprehension of the underlying phenomena

$$a_{c\mathbf{k}+\mathbf{q}}^{\dagger} a_{c\mathbf{k}} = \sum_{\nu\mu\mathbf{Q}} \Big(\Phi^{\nu *}(\mathbf{k} - \alpha\mathbf{Q}) \Phi^{\mu}(\mathbf{k} - \alpha\mathbf{Q} + \beta\mathbf{q}) \Big) X_{\mu \mathbf{Q}+\mathbf{q}}^{\dagger} X_{\nu \mathbf{Q}} \tag{3.8}$$

$$a_{v\mathbf{k}}^{\dagger} a_{v\mathbf{k}-\mathbf{q}} = -\sum_{\nu\mu\mathbf{Q}} \Big(\Phi^{\nu *}(\mathbf{k} + \beta\mathbf{Q}) \Phi^{\mu}(\mathbf{k} + \beta\mathbf{Q} - \alpha\mathbf{q}) \Big) X_{\mu \mathbf{Q}+\mathbf{q}}^{\dagger} X_{\nu \mathbf{Q}}. \tag{3.9}$$

Once more we focus on our observation on the conduction and valence band, which allows us to write the electron-phonon Hamiltonian as

$$H_{\text{el-ph}} = \sum_{\mathbf{kq}j} \Big(\mathcal{D}_{\mathbf{q}}^{cj} a_{c\mathbf{k}+\mathbf{q}}^{\dagger} a_{c\mathbf{k}} + \mathcal{D}_{\mathbf{q}}^{vj} a_{v\mathbf{k}+\mathbf{q}}^{\dagger} a_{v\mathbf{k}} \Big) \Big(b_{\mathbf{q}j} + b_{-\mathbf{q}j}^{\dagger} \Big).$$

Upon shifting the indices of the valence band and applying the operator relation introduced earlier, we derive the exciton-phonon Hamiltonian as follows

$$H_{\text{x-ph}} = \sum_{\mathbf{q}j} \sum_{\mathbf{Q}\mu\nu} D_{\mathbf{q}j}^{\mu\nu} X_{\mu \mathbf{Q}+\mathbf{q}}^{\dagger} X_{\nu \mathbf{Q}} \Big(b_{\mathbf{q}j} + b_{-\mathbf{q}j}^{\dagger} \Big). \tag{3.10}$$

Within this framework, we have introduced exciton-phonon interaction matrix elements, resulting in the expression $D_{\mathbf{q}j}^{\mu\nu} = \mathcal{D}_{\mathbf{q}}^{cj} \mathcal{J}_{\nu\mu}(\beta\mathbf{q}) - \mathcal{D}_{\mathbf{q}}^{vj} \mathcal{J}_{\nu\mu}(-\alpha\mathbf{q})$. Here, $\mathcal{J}_{\nu\mu}(-\alpha\mathbf{q})$ once again represents form factors (as discussed in Section 2.4.1). The matrix elements elucidate the strength of interaction between an exciton and a phonon

characterized by the momentum **q** and its branch j. Up to this point, our Hamiltonians have exclusively focused on intravalley excitons. However, it is essential to note that in solid-state systems, intervalley excitons also play a significant role as a phonon scattering channel. When addressing the Wannier equation, as elucidated in Section (3.3), the electron and hole momenta are consistently associated with the minimum of the parabolic band structure (valley). It is worth noting that, in principle, the electron's valley can differ from that of the hole, and yet the resulting Wannier equation remains unaltered. This is due to the fact that the Coulomb matrix element is invariant with respect to the separation of electron and hole in momentum space. As long as the electron and hole possess a positive reduced mass, they can coalesce to form a bound state, which we refer to as an "intervalley" or "indirect" exciton.

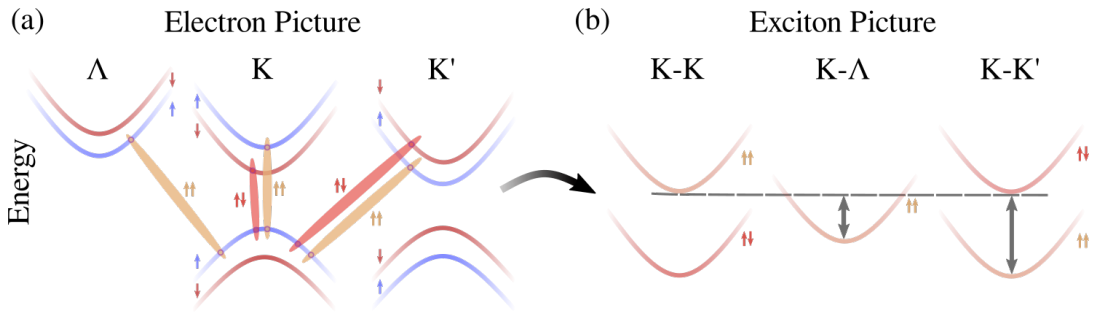

Figure 3.2: The schematic comprises two key elements: (a) the electronic band structure, which exhibits multiple minima and maxima in both the valence and conduction bands, and (b) the corresponding exciton center-of-mass dispersion. This dispersion includes not only the direct (K-K) exciton but also several intervalley excitons such as K-K' and K-Λ. The source of this figure is attributed to [33]

.

In Figure 3.2, you can see a graphical representation of the significant minima and maxima of valence and conduction bands. Additionally, it illustrates the dispersion of the center-of-mass for ground state excitons. It is worth noting that, owing to variations in binding energies and electronic band gaps, we observe a fascinating phenomenon: intervalley excitons such as K-Λ and K-K' can be found at energetically lower positions than the direct K-K exciton. Thus, we are facing the necessity to extend our theoretical framework. To this end, we include an additional valley quantum number γ. This new quantum number is easily incorporated into the

excitonic basis transformation (c.f. Eq.(3.6)). The operator relation reads

$$\mathcal{A}^{\dagger}_{\gamma\mathbf{k}\mathbf{k}'\gamma'} = \sum_{\mu} X^{\dagger}_{\mu,\gamma,\gamma',\mathbf{k}-\mathbf{k}'} \Phi^{\mu}_{\gamma\gamma'}(\alpha_{\gamma\gamma'}\mathbf{k} + \beta_{\gamma\gamma'}\mathbf{k}').$$

Since the electron and hole mass can differ between valley also the coeffients α and β become valley dependent coefficients. This procedure of extending our theoretical framework also applies for the Wannier equation. Hence, we are able to determine a valley dependent excitonic energie

$$E^{\mu\gamma\gamma'}_{\mathbf{Q}} = \frac{\hbar^2\mathbf{Q}^2}{2M_{\gamma\gamma'}} + E_G^{\gamma\gamma'} + E_B^{\mu\gamma\gamma'}.$$

In the equation presented above, we observe that the inclusion of the Coulomb interaction can lead to a reordering of the energy levels associated with direct and indirect transitions. In the electronic context, the energy of an interband transition can be straightforwardly determined as the band gap $E_G^{\gamma\gamma'}$, which represent as we determined in the previous section by the difference between the energy of the conduction band minimum and the valence band maximum. However, when taking the excitonic binding energy $E_B^{\mu\gamma\gamma'}$ into accound we observe for the same transition a redshift. Consequently, a momentum-indirect transition, which might be higher in terms of electronic energies compared to the direct transition, can exhibit a lower energy level in terms of excitonic energies. This intriguing observation underscores the significant impact of Coulomb interactions on the energy hierarchy of different electronic and excitonic transitions. As intervalley exciton states can potentially reside below the optically active K-K exciton [58, 59], they play a pivotal role in facilitating relaxation processes and significantly impact the optoelectronic characteristics in TMDs.

Expanding our theoretical framework involves exploring potential modifications in the exciton-phonon interaction. In this study, the primary mechanism for enabling significant momentum transfers between two valleys is the electron-phonon scattering process. To streamline our notation, we will incorporate the valley index, denoted as γ, into the excitonic composite index: $\mu = (n_\mu, \gamma_\mu, \gamma'_\mu)$, as well as into the phonon index, which we will transform into a compound index $j = (i_j, \gamma_j^{\mathrm{ph}})$. In this notation, n_μ represents the quantum number, while γ_μ/γ'_μ pertain to the electron/hole valley, respectively. In the phonon context, i_j characterizes the well-known phonon branch, and γ_j^{ph} indicates the valley where the phonon is situated. Within this notational

framework, the previously introduced electron-phonon Hamiltonian can be expressed as follows

$$H_{\text{el-ph}} = \sum_{\lambda \mathbf{k}\mathbf{q}\gamma\gamma' i} \mathcal{D}^{\lambda i}_{\gamma\gamma'\mathbf{q}} \Big(b_{\mathbf{q}i\gamma'-\gamma} + b^{\dagger}_{-\mathbf{q}i\gamma'-\gamma} \Big) a^{\dagger}_{\lambda\gamma'\mathbf{k}+\mathbf{q}} a_{\lambda\gamma\mathbf{k}}.$$

By following the identical procedure as previously outlined, we arrive at the exciton-phonon Hamiltonian

$$H_{\text{x-ph}} = \sum_{\mathbf{q}j} \sum_{\mathbf{Q}\mu\nu} D^{\mu\nu}_{\mathbf{q}j} X^{\dagger}_{\mu\mathbf{Q}+\mathbf{q}} X_{\nu\mathbf{Q}} \Big(b_{\mathbf{q}j} + b^{\dagger}_{-\mathbf{q}j} \Big). \tag{3.11}$$

Here, it is crucial to acknowledge that the exciton-phonon matrix elements now incorporate valley-dependent factors. The matrix elements read

$$\begin{aligned} D^{\mu\nu}_{\mathbf{q}j} = {} & \mathcal{D}^{cj}_{\gamma_\nu\gamma_\mu\mathbf{q}} \delta_{\gamma'_\nu\gamma'_\mu} \delta_{\gamma^{ph}_j,\gamma_\nu-\gamma_\mu} \mathcal{J}_{\nu\mu}(\beta\mathbf{q}) \\ & - \mathcal{D}^{vj}_{\gamma'_\nu\gamma'_\mu\mathbf{q}} \delta_{\gamma_\nu\gamma_\mu} \delta_{\gamma^{ph}_j,\gamma'_\nu-\gamma'_\mu} \mathcal{J}_{\nu\mu}(-\alpha\mathbf{q}). \end{aligned}$$

In this context, we employ super indices, emphasizing a consistent treatment of inter- and intravalley scattering. It is important to note that we have introduced delta functions to uphold the principles of conservation. Specifically, these delta functions serve two fundamental purposes. First, they ensure the preservation of the electron valley if the hole scatters with a phonon, and vice versa. Second, they guarantee the conservation of momentum, which necessitates that the phonon-valley configuration aligns with the electronic intervalley transition.

The expansion of our theoretical framework is crucial for comprehending various excitonic phenomena. This extension has been previously explored in works such as [33] and was later also extended to heterostructures by [27, 60]. Notably, these studies unveil a complex relationship between intervalley interactions, including the emergence of hybridized states, as seen in [33, 60]. In this context, Meneghini et al. have also scrutinized the intervalley relaxation dynamics. They observe that, in the $MoSe_2$-WSe_2 heterostructure, following an initialization at the K_WK_W valley in tungsten, excitons undergo various intermediary states as they relax to the interlayer K_WK_{Mo} valley. In the subsequent chapters of this work, we will place significant emphasis on heterostructures and interlayer excitons (see Chap.4).

It is noteworthy that in [27] already after 500 fs, the majority of excitons are found in the interlayer K_WK_{Mo} valley. Moreover, this state exhibits minimal hybridization (as

also shown in [27, 61, 62]). These two characteristics render this state particularly intriguing for our research. On the one hand, the relaxation processes occur on a significantly shorter timescale than the spatio-temporal dispersion we are investigating, which are typically on a ps to ns timescale. On the other hand, the negligible hybridization enables a clear definition of localized states. Therefore, we can summarize that intervalley processes are a central element in solid-state physics. However, within our framework they can be disregarded, since intervalley transitions have already been completed by the time spatio-temporal transport is initiated. Hence, in the subsequent chapters, we will omit the valley index. It is important to emphasize that these arguments hold true specifically for $MoSe_2$-WSe_2 heterostructures. For different materials, the lowest-energy valleys and the degree of hybridization can vary significantly.

4

Heterostructures

We briefly touched upon heterostructures and their significant impact on the energy landscape in the preceding chapter. Until now, our analysis has predominantly centered on monolayer TMDs and the diverse exciton states they harbor. However, a compelling avenue for expanding electronic possibilities involves stacking two monolayer TMDs vertically to create a bilayer structure. Homobilayers, which consist of two identical material layers, were once considered unremarkable byproducts of monolayer exfoliation. Yet, recent groundbreaking research conducted by Cao et al. has brought significant attention to the field of two-dimensional materials. They demonstrated unconventional superconductivity in magic-angle twisted bilayer graphene by stacking two graphene nanosheets with a relative twist of approximately 1.1° [63–65]. This concept of a "magic angle" was subsequently extended to graphene-like hexagonal boron nitride (h-BN) systems, where the twisting angle was controlled to modulate interactions within and between layers, sparking debates in the physics community [66]. These remarkable discoveries have given rise to the field of twistronics, where the manipulation of stacking arrangements in various two-dimensional materials opens up vast possibilities for tailoring material properties. Importantly, this approach can be used to engineer unique electronic behaviors by choosing different monolayer components and adjusting the relative stacking angles between layers, greatly expanding the scope of applications in many-particle physics. In particular, TMDs have garnered attention due to their exceptional optical, electrical, mechanical, and thermodynamic properties. Consequently, TMDs have found applications in a wide range of nanodevices, including optoelectronics, batteries, sensors, solar cells, and catalysis [67–77]. An essential distinction between bilayer structures and single layers is the presence of excitons, which can manifest as intralayer excitons, composed of electrons and holes within the same layer, or as interlayer excitons, where the electron and hole are spatially separated across both layers. In this section, we delve into the consequences of stacking two monolayers atop each other. We explore

the fascinating emergence of distinct stacking types and stacking areas within a bilayer. Additionally, we redefine our Coulomb potential to account for the Coulomb interaction with the second layer.

4.1 Stacking

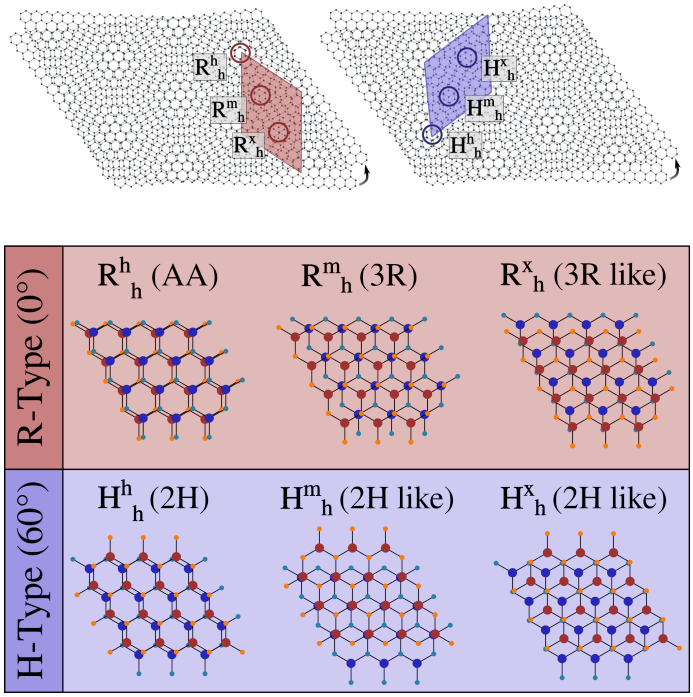

Figure 4.1: Schematic representation of distinct high-symmetry stacking configurations [78]

Monolayer materials, often referred to as van der Waals materials, derive their name from the characteristic of their bulk counterparts, consisting of atomic layers that interact weakly via van der Waals forces, while atoms within the same layer are bound together by robust covalent bonds. This distinction opens up avenues for innovative investigations, akin to those inspired by the concept of the magic angle. The control of stacking structures emerges as a promising strategy to fine-tune

interactions between electrons and holes. The act of stacking individual monolayers introduces adjustments to crystallographic alignments and interlayer interactions (as depicted in Figure 4.1), offering a highly valuable parameter for tailoring the electronic properties of nanomaterials. However, it is essential to recognize that the electronic structure of monolayers undergoes significant transformations when they are combined to form bilayers. For example, when a monolayer of tungsten disulfide (WS2) or tungsten diselenide (WSe2) is superimposed on a monolayer of molybdenum disulfide (MoS2), the bandgap undergoes a transition from direct to indirect or vice versa, resulting in the creation of heterostructures that exhibit extraordinary phenomena [79–82]. Furthermore, research has unveiled the influential role of the stacking sequence of monolayers in these heterostructures [60], particularly in shaping their photocatalytic activities and photovoltaic performance [76, 83]. Nevertheless, despite these structural modifications, it remains advantageous to employ the eigenstates of monolayers as the fundamental building blocks for the bilayer Hamiltonian.

In Chapter 2, we presented a model Hamiltonian tailored for monolayers. This simplified representation serves as a valuable tool for explaining many phenomena within a bilayer by employing a straightforward framework that treats two independent monolayers. Nonetheless, it is important to note that this simplification has its boundaries. To bridge the gap, we must introduce an extension that encompasses interlayer interactions. This extension can be intuitively understood within the monolayer basis by introducing a quantum number "l" to delineate between the lower layer ($l = 0$) and the upper layer ($l = 1$) terms within the Hamiltonian. In this context, the effective band masses maintain consistency with those of the monolayer. However, it is worth noting that the band gap and the precise alignment of the valence and conduction bands in both layers are intricately dependent on the specific materials chosen and the arrangement of the stacking. The stacking dependence arises from a rotational misalignment between the monolayer sheets, giving rise to an interference pattern in atomic positions referred to as a moiré pattern. In Chapter 5, we will delve deeper into moiré physics. This misalignment leads to spatially varying local stacking orders, and there are three specific locations where the local environment displays high symmetry, characterized by threefold rotational symmetry. These areas can be effectively represented by appropriately stacking the atoms within the primitive bilayer cell.

Figure 4.1 visually illustrates the atomic registries for various high-symmetry stackings. We have introduced a notation where R(H) signifies perfectly aligned lattices

with a 0° or 60° angle, as documented by Yu et al. [21]. In this alignment, the metal atoms of one layer are initially placed on top of the metal (chalcogen) atoms of the other layer, resulting in R_h^h (H_h^h) stacking, with 'h' indicating a hole or void. As we move along the high-symmetry line, further stacking configurations become apparent, as indicated by the circles in Figure 4.1. In these configurations, we observe either metal (m) or chalcogen atoms (x) positioned over holes in the second layer. It is worth noting that in the literature, the notation in brackets is also commonly used [78, 84]. However, we need to point out that this method is strictly valid only at very low twist angles, as for shorter periods, the atomic arrangement rapidly deviates from the high symmetry points. In homobilayers featuring R-type stacking, the electronic bands of the decoupled monolayers exhibit degeneracy. Nevertheless, in the event of a relative spatial rotation occurring in both layers, it leads to a corresponding adjustment in the orientation of the Brillouin zones within reciprocal space. Consequently, for layers rotated by 60°, the K point of one layer aligns with the K' point in the other layer. This rotation also causes an inversion in the spin ordering of bands in both layers. Consequently, we observe stacking-dependent selection rules [21, 85, 86].
In the context of a heterostructure, the differentiation between R- and H-type stacking remains applicable. However, it is important to note that when combining two dissimilar monolayers, they often possess distinct band gaps. The determination of the band alignment, which usually entails a constant offset, is a critical aspect of this analysis. This offset, stemming from variations in work functions (vacuum potentials) between the monolayers, is typically established through DFT calculations. These calculations shed light on the exciton landscape in the context of vertically stacked TMDs. Please note, due to the weak van der Waals forces between atoms in different layers compared to the strong in-plane bonds, we omit throughout this work stacking related phonon mode changes. Consequently, we add a layer index to the phonon quantum number, denoted as $j = (i_j, l_{\mathrm{ph}})$, while their energies and electron-phonon coupling elements remain unchanged. It is important to note that in this decoupled basis, direct phonon scattering between states in different layers is prohibited. In contrast to the electron-phonon interaction, the Coulomb potential of an electron in one layer extends into the other layer. Consequently, charges in different layers are subject to mutual Coulomb forces and can form interlayer excitons.

4.2 Coulomb Potential in Bilayers

The extension to bilayers introduces a significant Coulomb interaction between the layers, necessitating a redefinition of the Coulomb potential as introduced in Sec. 2.4.1. With our focus no longer restricted to a single material layer, we must adapt our initial definition to account for two homogeneous dielectric slabs. We make the assumption that these materials are stacked directly on top of each other, effectively reducing the interlayer distance to zero. This approximation holds true in practice since the actual distance is minuscule in comparison to the thickness of the materials, as supported by Merkl et al. (2019) [22]. As a result, we exclude this negligible distance from our macroscopic model, as it would be impractical to incorporate.
The dielectric environment is then defined as

$$\epsilon = \begin{cases} \epsilon^i_{BG} & \text{for} \quad z < -d_1 \\ \epsilon^i_{L} & \text{for} \quad -d_1 < z < 0 \\ \epsilon^i_{L'} & \text{for} \quad 0 < z < d_2 \\ \epsilon^i_{BG} & \text{for} \quad z > d_2 \end{cases}$$

When we place a point charge at the midpoint of one of the layers in a bilayer system, located at a height of $z_0 = \pm d_{(1/2)}/2$, we can use the established definition to set up boundary conditions for the electric field. This allows us to solve the Poisson equation and find the Coulomb potential, similar to what was done in Section 2.4.1 (reference [87]). As a result, we arrive at a familiar equation for the Coulomb potential in the bilayer system

$$V^{ll'}_{\mathbf{q}} = \frac{e^2}{2\epsilon_0 \tilde{\epsilon}_{ll'}(q) A q}. \tag{4.1}$$

In this equation, we have introduced the layer indices, denoted as l and l'. The key difference from the monolayer case is the presence of the layer-dependent dielectric function, $\tilde{\epsilon}_{ll'}$. This function can be divided into two essential cases: the interlayer and intralayer cases. For the interlayer case, the dielectric function is given by

$$\epsilon_{\text{inter}}(q) = \kappa_{BG} g_{12}(q) g_{21}(q) f(q).$$

Here, we have utilized the definition of κ from Section 2.4.1. To provide a more comprehensive overview, we also introduce the function $f(q)$ as follows

$$f(q) = 1 + \frac{1}{2}\Bigg(\Big(\frac{\kappa_1}{\kappa_{BG}} + \frac{\kappa_{BG}}{\kappa_1}\Big)\tanh(\delta_1 q) + \Big(\frac{\kappa_2}{\kappa_{BG}} + \frac{\kappa_{BG}}{\kappa_2}\Big)\tanh(\delta_2 q) + \Big(\frac{\kappa_1}{\kappa_2} + \frac{\kappa_2}{\kappa_1}\Big)\tanh(\delta_1 q)\tanh(\delta_2 q)\Bigg).$$

Additionally, we have the expression for $g_{ll'}$

$$g_{ll'} = \frac{\cosh(\delta_l q)}{\cosh\left(\frac{\delta_{l'} q}{2}\right)\left(1 + \frac{\kappa_{BG}}{\kappa_l}\tanh\left(\frac{\delta_l q}{2}\right)\right)}.$$

These equations highlight the increased complexity of the Coulomb potential in a bilayer system. The dielectric function and associated factors, including $f(q)$ and $g_{ll'}$, play a crucial role in determining the electrostatic interactions between charges in different layers, adding depth to our understanding of the system. Similarly, for the intra-layer case in the bilayer system, we can derive the dielectric function as follows

$$\epsilon^l_{\text{intra}}(q) = \frac{\kappa_{BG} g_{l'l'} f(q)}{\cosh\left(\frac{\delta_{l'} q}{2}\right) h_{ll'}}.$$

In this equation, we introduce the function $h_{ll'}$ to capture the intricacies of the intra-layer interactions

$$h_{ll'} = 1 + \frac{\kappa_{BG}}{\kappa_l}\tanh(\delta_l q) + \frac{\kappa_{BG}}{\kappa_{l'}}\tanh\left(\frac{\delta_{l'} q}{2}\right) + \frac{\kappa_l}{\kappa_{l'}}\tanh(\delta_l q)\tanh\left(\frac{\delta_{l'} q}{2}\right).$$

Here, we note that $\delta_i = \alpha_i d_i$, where α represents the dielectric constant, as defined in Section 2.4.1. Additionally, the variable d_i corresponds to the thickness of the respective layers. Essentially, the modified potential in the bilayer system introduces significant screening effects within the layers, leading to a further reduction in the

potential between charges in different layers, due to specific geometric constraints. The effective two-dimensional Coulomb potential, represented as $V_q^{ll'}$, accommodates this constraint through the dielectric functions $\epsilon^l_{\text{inter}}/\epsilon^l_{\text{intra}}$. This approach simplifies the treatment of the bilayer system as a 2D system while considering the intricacies of the spatial arrangement of states along the z-direction. The associated error in the binding energy, resulting from this approximation, is typically within 10%, corresponding to just a few meV. As such, for the purpose of modeling the Coulomb interaction, these variations can be safely disregarded, and as mentioned above the thickness parameters (d_i) for monolayers can be employed.

5

Moiré Physics

In the preceding chapter, we delved into the stacking of dissimilar monolayer materials (heterobilayer), particularly TMDs, revealing a variety of intriguing phenomena such as charge carrier dynamics and charge transport properties [4, 5, 88, 89]. These structures pose intriguing research questions due to their tunable exciton energy landscape dictated by the twist angle [21–25]. In the realm of twisted heterostructures, a moiré superlattice emerges—a superposition of the individual monolayers' geometries, strongly dependent on the twist angle [90–94]. This twist angle sensitivity leads to diverse energy landscapes, including the intriguing realm of trapped exciton states [28, 29]. Heterobilayer often exhibits a staggered (type II) band alignment, where electrons and holes reside in distinct layers. Our earlier discussion touched upon the generation of electron-hole pairs within a layer (intralayer excitons) and their transition to a more favorable charge-separated state (interlayer excitons), facilitated by a reduced interlayer band gap.
This section introduces a theoretical model for intra- or interlayer moiré excitons. We employ the concept of zone folding, widely employed in solid-state physics, to derive a microscopic model for the electrostatic potential experienced by electrons in one layer due to the presence of a second layer. This approach allows us to incorporate the intricate nature of moiré physics into our framework. It is crucial to note that our focus in this section is specifically on excitons at the K point, given that hybridization effects, already weak for homobilayers, are further suppressed by the band offset in a heterobilayer.

5.1 Zone Folding

Within crystalline materials, scattering phenomena often lead to a wave vector $\tilde{\mathbf{k}}$ extending beyond the confines of the first Brillouin zone (BZ). An illustrative instance

is electron-phonon scattering, as discussed in section 2.5, where we established that interaction with a phonon allows an electron to acquire momentum $\mathbf{k}$'=$\mathbf{k}$+$\mathbf{q}$, with $\mathbf{q}$ representing the phonon momentum. This resultant momentum, $\mathbf{k}$', may, however, fall outside the first Brillouin zone. Given the material's periodic nature, any point outside the first BZ can be equivalently represented as a point inside the zone, employing the reciprocal vector $\mathbf{G}$. Such processes, known as Umklapp processes or zone folding, exemplify the periodic wrapping of vectors to preserve the material's lattice periodicity. Figure 5.1 visually conveys this concept. On the right, the

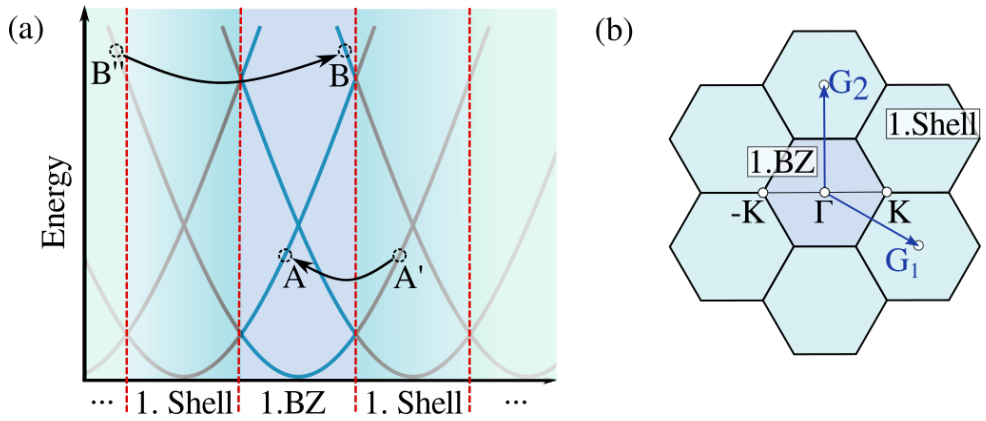

Figure 5.1: Schematic representation of the zone folding approach in 1D (a) and 2D (b). Additionally we introduce the concept of shells, which represent the neighboring BZ to the first BZ.

schematic illustrates the first Brillouin zone (BZ) and its adjacent zones, referred to as shells. These shells are displaced by the corresponding reciprocal vectors $\mathbf{G}_1$, $\mathbf{G}_2$, or linear combinations thereof. Figure 5.1(a) provides a detailed view of a 1-dimensional Umklapp process. The momentum $\mathbf{k}$'=$\mathbf{k}$+$\mathbf{q}$ may lead to an energy state at point A', yet this point is effectively represented by the same energy level at point A within the first BZ. Consequently, by introducing a reciprocal lattice vector, such that $\mathbf{k}$"=$\mathbf{k}$+$\mathbf{q}$+$\mathbf{G}$ resides within the first Brillouin zone, we can confine our analysis to BZ and still include in complete momentum space by applying multiples of $\mathbf{G}$, as exemplified by the transition from point B" to B. This approach gives rise to multiple subbands (see blue lines in Fig. 5.1(a)).

5.2 Interlayer Moiré Potential

While integrating the impact of stacking-induced moiré potential on the existing excitons, our initial step involves introducing the interaction to the electrons. To achieve this, we introduce an effective single-particle Hamiltonian designed for valence and conduction band electrons.

$$\hat{H} = -\frac{\hbar^2}{2m}\nabla^2 + \sum_l V_l(r),$$

where V_l represent the effective electrostatic potential created by the respective layer (l = 0,1). Extending this into second quantization we find the following Hamiltonian

$$H = \sum_{ll'\mathbf{k}\mathbf{k}'} \langle l\mathbf{k}| \hat{H} |l'\mathbf{k}'\rangle \, a^\dagger_{l\mathbf{k}} a_{l'\mathbf{k}'}. \tag{5.1}$$

We can separate this into three parts. First the in section 2.3 introduced non-interacting electron Hamiltonian. For the other two parts we can find more interesting interaction terms. The Hamiltonian yields

$$H = H_{\mathrm{el}} + H_{\mathrm{T}} + H_{\mathrm{M}}. \tag{5.2}$$

The Hamiltonian H_{T} denotes the interlayer tunneling Hamiltonian, which incorporates interaction components facilitating carrier transfer from $|l'k'\rangle$ to the adjacent layer $|lk\rangle$. For strongly interacting layers, such interactions can result in significant energy shifts [57]. However, despite the potential for intriguing developments in this context, it falls beyond the scope of this work. Our focus is solely on the latter part of the interaction, which characterizes the potential change arising from the presence of the potential originating from the other layer (referred to as 1-l). The Hamiltonian is expressed as follows

$$H_{\mathrm{M}} = \sum_{l\mathbf{k}\mathbf{q}} \mathcal{V}_l(\mathbf{q},\mathbf{k}) a^\dagger_{l\mathbf{k}+\mathbf{q}} a_{l\mathbf{k}}. \tag{5.3}$$

Here, $\mathcal{V}_l(\mathbf{q},\mathbf{k}) = \langle l\mathbf{k}+\mathbf{q}| V_{1-l} |l\mathbf{k}\rangle$ represents this potential in second quantization. Please note that, for simplicity, we omit the band index λ. In the context of type-II heterostructures, this moiré Hamiltonian gains increasing importance, as the previously mentioned tunneling Hamiltonian diminishes in significance due to the larger

gap between the layer energy bands. However, even in these heterostructures, there exists a substantial stacking-dependent energy landscape. Therefore, further exploration of the additional electrostatic potential in layer l is warranted. Thus, we first have to take a closer look at the potential

$$\mathcal{V}_l(\mathbf{q},\mathbf{k}) = \langle l\mathbf{k}+\mathbf{q}|\, V_{1-l}\, |l\mathbf{k}\rangle\,.$$

If we now utilize a tight binding expansion as well as the fact that we can express the effective lattice potential as a sum of it atomic contributions, which leads to the equation

$$V_l = \sum_{\mathbf{R}_l} v_l(\mathbf{r}-\mathbf{R}_l).$$

These steps lead us then to

$$\mathcal{V}_l(\mathbf{q},\mathbf{k}) = \frac{1}{N}\sum_{\mathbf{R}_l,\mathbf{R}_l',\mathbf{R}_{1-l}} e^{i(-(\mathbf{k}+\mathbf{q})\cdot\mathbf{R}_l+\mathbf{k}\cdot\mathbf{R}_l')}\int d^3\mathbf{r}\phi_l^*(\mathbf{r}-\mathbf{R}_l)v_{1-l}(\mathbf{r}-\mathbf{R}_{1-l})\phi_l(\mathbf{r}-\mathbf{R}_l').$$

This integral is only different from zero if $R_l = R_l'$. Furthermore, we are now able to index shift $r \to r+R_l$. On top of that we perform an in-plane Fourier transformation, which changes the potential to

$$\mathcal{V}_l(\mathbf{q},\mathbf{k}) = \frac{1}{A_{\mathrm{UC}}N^2}\sum_{\mathbf{R}_l,\mathbf{R}_{1-l}} e^{-i\mathbf{q}\cdot\mathbf{R}_l}\int d^2\mathbf{k}dz e^{i\mathbf{k}\cdot(\mathbf{R}_l-\mathbf{R}_{1-l})}\tilde{v}_{1-l}(\mathbf{k},z)\tilde{\rho}_l(-\mathbf{k},z).$$

Where A_{UC} represents the area of the unit cell and $\tilde{\rho}_l(-\mathbf{k},z)$ represents the Fourier transformed of the charge density $\rho_l(\mathbf{r}) = \phi_l^*(\mathbf{r})\phi_l(\mathbf{r})$. Please note, in equation above the integral over the real space was separated into an outer plain variable z and the remaining in plain contribution. The latter lead to $\int d^2\mathbf{r}\,\exp[i(\mathbf{k}-\mathbf{k}')\cdot\mathbf{r}] = \delta(\mathbf{k}-\mathbf{k}')$. This leads us ultimately to

$$\mathcal{V}_l(\mathbf{q}) = \sum_{\mathbf{G}_l,\mathbf{G}_{1-l}} m_l(\mathbf{G}_{1-l})e^{i(\mathbf{G}_l+\mathbf{G}_{1-l})\cdot\mathbf{D}_l/2}\delta_{\mathbf{q},\mathbf{G}_{1-l}-\mathbf{G}_l}. \tag{5.4}$$

Here, $m_l(\mathbf{q}) = 1/A_{UC}\int dz\tilde{v}_{1-l}(\mathbf{q},z)\tilde{\rho}_l(-\mathbf{q},z)$ representes the atomic interaction energy. While, we additionally utilized the identity

$$\frac{1}{N}\sum_{R_i} e^{i\mathbf{q}\cdot\mathbf{R}_i} = \sum_{\mathbf{G}_i} e^{i\mathbf{G}_i\cdot\mathbf{R}_i^0}\delta_{\mathbf{q},\mathbf{G}_i},$$

which ensures momentum preservation. Furthermore, we introduced the convention that the real space coordinate system is centered in the middle of a connection line between nearest neighbors of different layers, i.e. $\mathbf{R}_l^0 = -\mathbf{R}_j^0 = \mathbf{D}_i/2$. Considering the effective atomic potentials introduced earlier in our discourse, it is observed that these potentials in the adjacent layer exhibit characteristics typical of long-ranged potentials, owing to the van der Waals nature inherent in interlayer forces. As a consequence, the interaction length proves to be significantly larger than the unit cell, causing a rapid decrease in momentum space compared to $\mathbf{G}$.
This allows us to confine in Eq.(5.4) the summation over reciprocal lattice vectors $\mathbf{G}$ to the first shell. It is noteworthy that we choose to disregard the contributions of constant $G = 0$ terms. We attribute these terms to the band alignment components originating from the band structures of the two monolayers. This simplification is justified by the fact that such contributions result in spatially constant band shifts. Given that the atomic contributions of the potential remain unchanged under three-fold symmetry, it follows that the atomic interaction energy m_l also exhibits this invariance. Consequently, we can express m_l in terms of contributions from the metal (α) and chalcogen atoms (β). The energy expression is then given by

$$m_l = \alpha_l + e^{2\pi i \sigma_{1-l}/3}\beta_l. \tag{5.5}$$

Here, α and β represent two real parameters derived from ab initio calculations [95]. Additionally, we introduce the parameter σ_i, which encapsulates the stacking-dependent behavior of the resulting potential. The values of σ_i vary between $\sigma_i = 1$ for R-type stacking and $\sigma_i = (-1)^i$ for H-type stacking.
With these consideration we are now finally able to express the moiré Hamiltonian as

$$H_{\mathrm{M}} = \sum_{l\mathbf{kq}} \mathcal{V}_l(\mathbf{q}) a^\dagger_{l\mathbf{k}+\mathbf{q}} a_{l\mathbf{k}} + \mathrm{h.c.}, \tag{5.6}$$

$$\mathcal{V}_l(\mathbf{q}) = m_l \sum_{i=0}^{2} e^{iC_3^i(\mathbf{G}_l^{(0)}+\mathbf{G}_{1-l}^{(0)})\cdot\mathbf{D}_l/2}\delta_{\mathbf{q},C_3^i(\mathbf{G}_{1-l}^{(0)}-G_l^{(0)})}.$$

Please note that we have partitioned the sum over the reciprocal lattice vectors, which explicitly exhibits C_6 symmetry in the first shell, into two distinct parts. The first part involves a summation over $C_3^i \mathbf{G}^{(0)}$, while the residual portion has been integrated into the hermitian conjugated Hamiltonian. This enables us to introduce moiré reciprocal lattice vectors $\mathbf{g}_i = C_3^i(\mathbf{G}_1^{(0)} - \mathbf{G}_0^{(0)})$, and accordingly, the lattice vectors $\mathbf{a}_i$ in real space. These vectors must satisfy the condition $\mathbf{g}_i \cdot \mathbf{a}_j = 2\pi\delta_{ij}$.

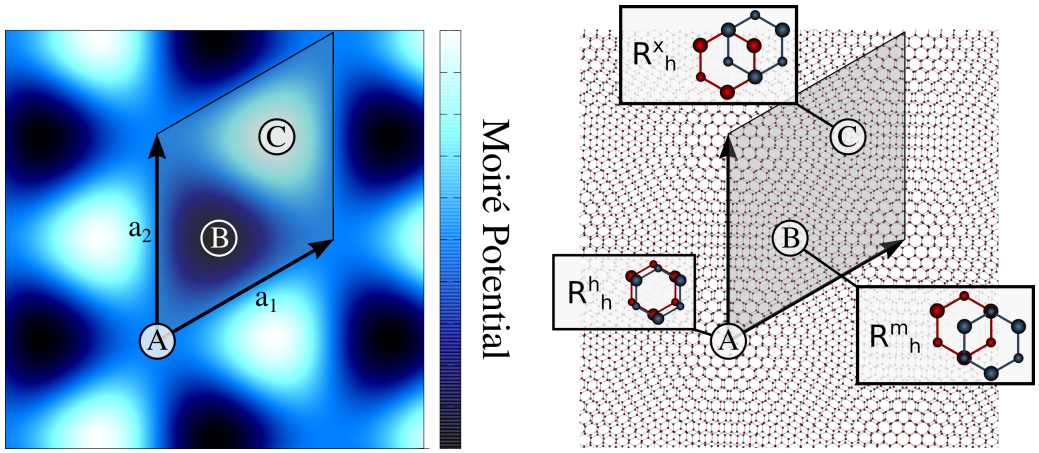

Figure 5.2: (a) Illustrates the spatial displacement of the interlayer moiré potential within a twisted heterostructure in real space. In this context, a_i denotes the fundamental lattice vectors in the moiré supercell. (b) Depicts the corresponding configurations of the twisted lattices. Three points of interest (A, B, C) are highlighted in both images. Upon comparison, it becomes evident how lattice mismatches result in the corresponding moiré potential. For instance, that R_h^m stacking corresponds to a potential minimum [23].

The microscopic model we have defined captures the intricate stacking dependence and correlates it with the moiré potential in a twisted bilayer. In Figure 5.2, (a) illustrates the resultant moiré potential in real space. By comparing this with (b), we can link the potential landscape to specific stacking configurations. Notably, potential minima are observed in a R-type-stacked interlayer heterostructure during R_h^m stacking. Conversely, the maxima are associated with R_h^x stacking [21, 23, 55, 96].

5.3 Moiré Exciton Transformation

In the preceding section, we established a moiré Hamiltonian that characterizes the impact of the effective lattice potential on an electron within the given layer. Build-

ing upon this foundation, the following section aims to broaden this Hamiltonian's scope by incorporating an excitonic basis. Our objective is to deduce an effective single-particle Hamiltonian and subsequently analyze the excitonic band structure within the context of a moiré potential. In the course of this study, we have incor-

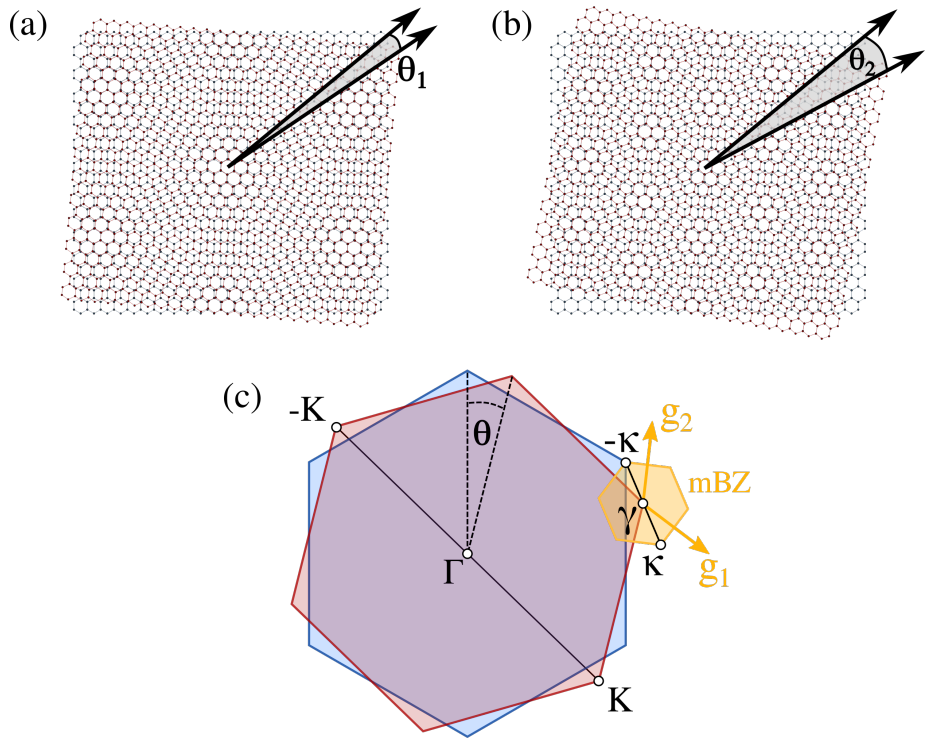

Figure 5.3: Real space representations of the observed moiré pattern in (a) and (b), depicting a decrease in moiré period with increasing twist angle Θ_i, indicating reduced distance between potential minima. (c) Illustrates the momentum space representation, showing overlapping first Brillouin zones and the formation of a mini-Brillouin zone (mBZ) with the corresponding moiré reciprocal lattice vector.

porated the notion of the moiré potential on multiple occasions. Figures 5.3 (a)-(b) provide visual representations of the observed moiré pattern. Notably, as the twist angle Θ_i increases, Figure 5.3 illustrates a decrease in the moiré period—signifying a reduction in the distance between potential minima. Extending this discussion, the diminishing moiré period implies a more pronounced influence of the moiré potential on the system.The nuanced dependence on the twist angle underscores the intricate

interplay between electronic behavior and the moiré pattern, serving as the driving force behind our explorations and considerations. To transform the newly formulated Hamiltonian into the excitonic basis, we introduced electron-hole pair operators in Sec.3.2 as follows $A^{\dagger}_{l\mathbf{k},l'\mathbf{k}'} = \sum_{\nu} X^{\nu\dagger}_{ll',\mathbf{k}-\mathbf{k}'}\psi^{\nu}_{ll'}(\alpha_{ll'}\mathbf{k}' + \beta_{ll'}\mathbf{k})$, where we expanded into excitonic eigenmodes [23]. Notably, the layer index l has now been incorporated. It is crucial to observe that the factors $\alpha_{ll'}/\beta_{ll'}$ encompass the respective electron and hole masses in the conduction/valence band. For a WSe_2-$MoSe_2$ bilayer, these values are $m_e/m_0 = 0.36(0.6)$ and $m_h/m_0 = 0.29(0.5)$, extracted from Ref.[97]. Initially, we proceed with the transformation of the moiré Hamiltonian from the electron basis to the exciton basis. This process involves leveraging our findings from Eq.(5.6). As a reminder, the Hamiltonian is expressed as follows

$$H_{\mathrm{M}} = \sum_{l\mathbf{k}\mathbf{q}\lambda} \mathcal{V}^{\lambda}_{l}(\mathbf{q}) a^{\dagger}_{\lambda l\mathbf{k}+\mathbf{q}} a_{\lambda l\mathbf{k}} + \mathrm{h.c.}.$$

By expressing the sum over the band index as separate parts for condition and valence band, we obtain

$$H_{\mathrm{M}} = \sum_{l\mathbf{k}\mathbf{q}} \left(\mathcal{V}^{c}_{l}(\mathbf{q}) a^{\dagger}_{cl\mathbf{k}+\mathbf{q}} a_{cl\mathbf{k}} + \mathcal{V}^{v}_{l}(\mathbf{q}) a^{\dagger}_{vl\mathbf{k}+\mathbf{q}} a_{vl\mathbf{k}} \right) + \mathrm{h.c.},$$

where we depict the electronic moiré potential $V^{v/c}_{l}$ in the valence and conduction band respectively. By shifting the index within the second part inside the bracket $(a^{\dagger}_{vl\mathbf{k}} a_{vl\mathbf{k}-\mathbf{q}})$, we can readily identify the transformations introduced in Sec.3.2. Specifically, we employ the relations given in Eq.(3.8) and Eq.(3.9). This leads us to

$$H_{\mathrm{M}} = \sum_{ll'\mathbf{q}} \sum_{\mathbf{Q}\mu\nu} \left(\mathcal{V}^{c}_{l}(\mathbf{q}) \mathcal{J}_{ll'}(\beta_{ll'}\mathbf{q}) - \mathcal{V}^{v}_{l'}(\mathbf{q}) \mathcal{J}^{*}_{ll'}(\alpha_{ll'}\mathbf{q}) \right) X^{\dagger}_{ll'\mathbf{Q}+\mathbf{q}} X_{ll'\mathbf{Q}} + \mathrm{h.c.}.$$

Here, we reintroduced the excitonic form factor $\mathcal{J}_{ll'}(\mathbf{q}) = \sum_{k} \psi^{*}_{ll'}(\mathbf{k})\psi_{ll'}(\mathbf{k}+\mathbf{q})$ (see Eq.(2.9)). We are now able to express the equation as

$$H_{\mathrm{M}} = \sum_{ll'\mathbf{Q}\mathbf{q}} \mathrm{M}^{ll'}_{\mathbf{q}} X^{\dagger}_{ll'\mathbf{Q}+\mathbf{q}} X_{ll'\mathbf{Q}} + h.c., \tag{5.7}$$

where we have introduced the abbreviation for the moiré matrix element $\mathrm{M}^{ll'}_{\mathbf{q}}$. Furthermore, we assume that our system is in the low-density limit. Hence, we

focus on the excitonic ground state 1s, and therefore, omit the excitonic states μ and ν. We adopt a microscopic approach to describe the electronic moiré potentials. Additionally, considering that the moiré potential establishes a superlattice with a periodicity $|\mathbf{G_0}|$ (as illustrated in the preceding sections), limiting the mixing to discrete center-of-mass momenta, we employ a zone-folding approach to capitalize on the properties of the new periodic lattice. This approach leads us to

$$H_{\mathrm{M}} = \sum_{L\mathbf{Q}n} \zeta_L X^\dagger_{L\mathbf{Q}+(-1)^{l_e}\mathbf{G}_n} X_{L\mathbf{Q}} \quad \text{with} \tag{5.8}$$

$$\zeta_L = \begin{cases} m^c_{l_e}\mathcal{J}_L(\beta_L\mathbf{G}_0) - m^v_{l_h}\mathcal{J}_L(\alpha_L\mathbf{G}_0) & \text{for } l_e = l_h \\ m^c_{l_e}\mathcal{J}_L(\beta_L\mathbf{G}_0) - m^{v*}_{l_h}\mathcal{J}_L(\alpha_L\mathbf{G}_0) & \text{for } l_e \neq l_h \end{cases},$$

where the parameters m^λ_l are extracted from first principle computations (see Eq.(5.5)). The free exciton Hamiltonian we introduced in Eq. 3.7 reads in the low density regime

$$H_{\mathrm{F}} = \sum_{ll'\mathbf{Q}} \varepsilon^{ll'}_{\mathbf{Q}} X^\dagger_{ll'\mathbf{Q}} X_{ll'\mathbf{Q}}.$$

where $\varepsilon^{ll'}_{\mathbf{Q}}$ again denotes the free exciton dispersion. This enables us to define a Hamiltonian for an exciton in a moiré potential $H = H_{\mathrm{F}} + H_{\mathrm{M}}$. By changing into a zone-folded eigenbasis, with operator relation $F^\dagger_{Ls\mathbf{Q}} = \tilde{X}_{L,\mathbf{Q}+\mathbf{G}_s}$, we obtain

$$H = \sum_{Ls\mathbf{Q}} \tilde{\varepsilon}_{L,\mathbf{Q}+s_1\mathbf{G}_1+s_2\mathbf{G}_2} F^\dagger_{Ls\mathbf{Q}} F_{Ls\mathbf{Q}} + \sum_{Lss'\mathbf{Q}} \tilde{\mathcal{M}}^L_{ss'} F^\dagger_{Ls\mathbf{Q}} F_{Ls'\mathbf{Q}}. \tag{5.9}$$

Here, the s and s'-index indicate the shells we include in our computations and $L = (l_e, l_h)$. As we learned in Sec. 5.1 this shell index can also be interpreted as a subband index. Additionally, we introduced a modified moiré mixing matrix element

$$\begin{aligned} \tilde{\mathrm{M}}^L_{ss'} = \zeta_L \Big(& \delta(s_1, s'_1 + (-1)^{l_e})\delta(s_2, s'_2) + \delta(s_1, s'_1)\delta(s_2, s'_2 + (-1)^{l_e}) \\ & + \delta(s_1, s'_1 - (-1)^{l_e})\delta(s_2, s'_2 - (-1)^{l_e}) \Big) \\ + \zeta^*_L \Big(& \delta(s_1, s'_1 - (-1)^{l_e})\delta(s_2, s'_2) + \delta(s_1, s'_1)\delta(s_2, s'_2 - (-1)^{l_e}) \\ & + \delta(s_1, s'_1 + (-1)^{l_e})\delta(s_2, s'_2 + (-1)^{l_e}) \Big). \end{aligned}$$

We change to the eigenbasis

$$Y^{\dagger}_{L\nu\mathbf{Q}} = \sum_{s} c^{\nu *}_{Ls}(\mathbf{Q}) F^{\dagger}_{Ls\mathbf{Q}}.$$

where the coefficients fulfill the eigenvalue equation

$$\tilde{\varepsilon}_{L,\mathbf{Q}+s_1\mathbf{G}_1+s_2\mathbf{G}_2} c^{\nu}_{Ls}(\mathbf{Q}) + \sum_{s'} \tilde{\mathrm{M}}^{L}_{ss'} C^{\nu}_{Ls'}(\mathbf{Q}) = E_{L\mu\mathbf{Q}} C^{\nu}_{Ls}(\mathbf{Q}).$$

This new basis leads us to the final diagonal Hamiltonian

$$H = \sum_{L\mu\mathbf{Q}} E_{L\mu\mathbf{Q}} Y^{\dagger}_{L\mu\mathbf{Q}} Y_{L\mu\mathbf{Q}}. \tag{5.10}$$

As we can see this Hamiltonian is diagonal for our new defined moiré excitons. This eigenvalue problem can be solved numerically. In our computation in order to make sure the eigenvalues are converged, we included the seven nearest neighboring shells. As a result we obtain the band structure as depicted in Fig.5.4. This picture shows the exemplary band structures of a interlayer exciton in a twisted $MoSe_2/WSe_2$ heterostructure encapsulated in hexagonal boron nitride (hBN) for $\theta = 1°$ as well as $\theta = 3°$.
At $\theta = 1°$ twist angle, we observe the emergence of several flat exciton bands, indicative of so called trapped exciton states in real space. This characteristic is particularly evident in momentum space, attributed to the compact size of the moiré Brillouin zone (mBZ) and the consequential extensive overlap of excitonic wavefunctions. The significant overlap results in a pronounced influence of the moiré potential, as evident in Eq.(5.10). Consequently, the group velocity $v_G = \sum_j 1/\hbar(\partial E_{\mathbf{Q}}/\partial Q_j)$ at these small twist angles experiences a significant reduction. This leads to a pronounced slowdown in the propagation of excitons for small twist angles [23]. Further elaboration in Sec. 7.5 will reveal a notably localized exciton distribution at this angle, impeding exciton propagation. Therefore, we characterize these states as trapped excitonic states.
Conversely, at a twist angle $\theta = 3°$, the bands display a parabolic dispersion, signifying greater mobility. The exciton delocalization observed at larger twist angles [23, 30] is a direct outcome of the zero-point energy associated with quantum-confined

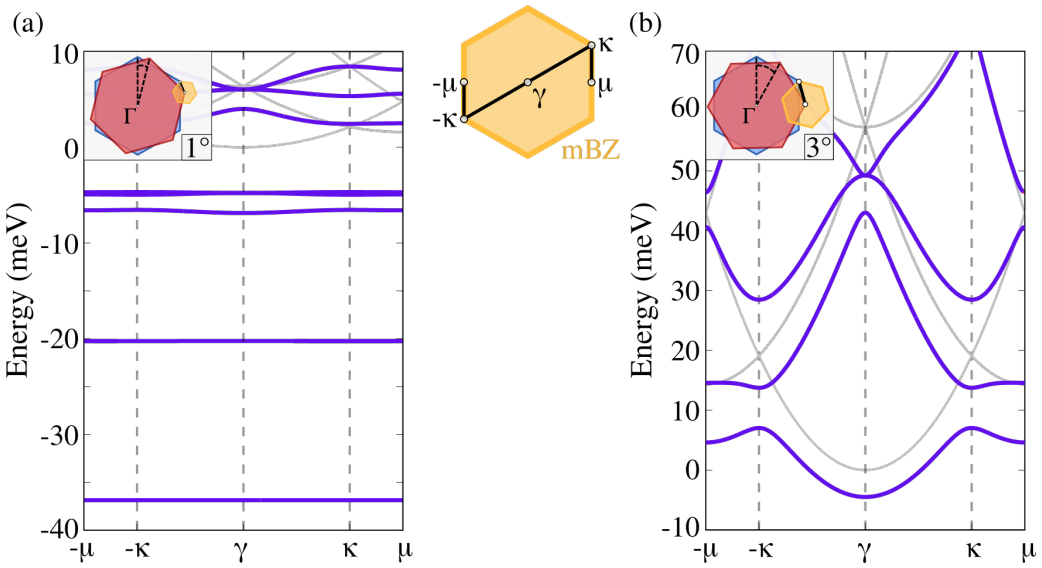

Figure 5.4: Moiré exciton subbands for interlayer excitons in the twisted $MoSe_2/WSe_2$ heterostructure at (a) $\theta = 1°$ and (b) $\theta = 3°$, respectively.

states. As the confinement length scale decreases (twist angle increases), the zero-point energy of the ground state exciton rises. At a critical confinement length, the zero-point energy surpasses the depth of the moiré potential, resulting in exciton delocalization and an associated increase in mobility. We can approach this observation from a more mathematical perspective. In Fig. 5.4, we present a schematic illustration of the mBZ in momentum space. Notably, as the twist angle increases, the mBZ also expands. Consequently, due to the reduced overlap of the excitonic wavefunction (see Eq.(5.8)), characterized by smaller form factors, the moiré matrix elements exhibit a decrease. This observation indicates that for larger twist angles, there is a convergence towards the behavior observed in the free excitonic case [23].

6

Polaron Transformation

In a previous section we explored the concept of an effective electronic potential. This potential was postulated to have equilibrium positions for the nuclei coinciding with the lattice nodes within a crystalline material. When we expanded this potential, it revealed a harmonic behavior with respect to the nuclear positions. This harmonic potential, crucial to understanding lattice vibrations, could be quantized through the introduction of bosonic annihilation and creation operators. This insightful framework laid the foundation for the concept of phonons, which are quanta of lattice vibrations in a crystal lattice. By applying a normal mode decomposition to this harmonic potential, we uncovered the existence of various phonon modes, notably acoustic and optical modes. These modes are distinctive in their characteristics and play pivotal roles in the material's thermal and optical properties. In Eq.(2.11), we derived the phonon Hamiltonian, a fundamental expression describing the energy and dynamics of phonons within the crystal.

$$H_{ph} = \sum_{\mathbf{q}j} \hbar\omega_{j\mathbf{q}} \Big(b^{\dagger}_{\mathbf{q}j} b_{\mathbf{q}j} + \frac{1}{2} \Big).$$

This Hamiltonian captures the intricate interplay between the nuclear positions and the corresponding phonon modes, providing a powerful tool for analyzing the behavior of lattice vibrations in crystalline materials. Understanding these phonon modes and their interactions is essential for comprehending various physical phenomena, such as heat conduction, optical properties and spatio temporal dispersion, in crystalline solids. Therefore, we employ the interaction Hamiltonian previously discussed in Eq.(2.12) which yields

$$H_{el-ph} = \sum_{\mathbf{k}\mathbf{q}j} \mathcal{D}^{j}_{\mathbf{q}} a^{\dagger}_{\mathbf{k}+\mathbf{q}} a_{\mathbf{k}} \Big(b_{\mathbf{q}j} + b^{\dagger}_{-\mathbf{q}j} \Big).$$

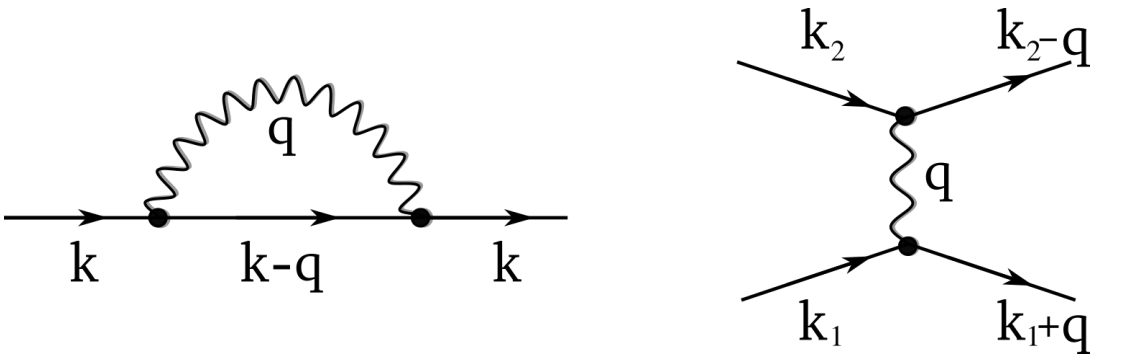

Figure 6.1: (a) Schematic on the coupling between excitons and lattice vibrations (phonons), resulting in the formation of polarons in a twisted TMD heterostructure. (b) Schematic illustration of the polaron-induced spatial narrowing of the excitonic wave function in presence of a moiré potential. This effect is temperature and twist-angle dependent and has a direct impact on the exciton band width and its propagation behaviour.

The electron-phonon Hamiltonian plays a crucial role in understanding and predicting various material properties and the fascinating interplay between electron and phonon, after being thoroughly discussed in prior sections. This leads us to the complete Hamiltonian

$$H = H_0 + H_{ph} + H_{el-ph}.$$

To better comprehend the Hamiltonian, it's valuable to employ diagrams that represent interaction processes. These so called Feynman diagrams illustrated elementary processes from absorption to emission of phonons and the corresponding influence on the regarding electron. Notably, such scattering processes play a pivotal role in understanding electrical resistance, particularly with phonon contributions prevailing at elevated temperatures. Combination of these elementary processes can lead into more complex diagrams with multiple vertices, facilitating the mediation of effective interactions. For instance, an electron might emit phonons and subsequently reabsorb them, as depicted in Fig. 6.1. This localized lattice polarization, which is associated with an electron, is known as a "polaron" and will be the main focus of this chapter. It constitutes a quasi-particle composed of a real particle (the electron) and another quasi-particle (the phonons). Alternatively, emitted phonons can be absorbed by another electron, giving rise to an effective scattering process involving two electrons, as shown in Fig. 6.1.

6.1 Lang Firsov Transformation

The polaron or Lang-Firsov transformation is a powerful method employed in quantum mechanics to simplify and analyze complex Hamiltonian systems, especially those involving the coupling of electrons to a non-interacting bosonic reservoir, such as phonons in a crystal lattice. This transformation provides a unitary mapping from an original Hamiltonian to an effective Hamiltonian, making it easier to study the system's behavior. A unitary mapping or unitary transformation is a type of linear transformation that preserves the inner product and, consequently, the normalization of quantum states. This transformation U has to satisfies the condition $UU^\dagger = U^\dagger U = I$, where $U^\dagger$ denotes the adjoint (or conjugate transpose) of U, and I is the identity operator. The Lang-Firsov transformations represents a specific types of unitary transformations. In the context of polaron transformation, an Hermitian operator A is introduced, operating within a distinct Hilbert space from the bosonic operators. The transformation operator U is defined as

$$U = e^{A(\alpha b - \alpha^* b^\dagger)}, \tag{6.1}$$

where α is a complex coefficient that can be chosen conveniently. This transformation proves particularly useful when dealing with electron-phonon interactions in solid-state physics. It allows for the incorporation of the phonon degrees of freedom into the electronic Hamiltonian, effectively dressing the electrons with phonon clouds. By doing so, the transformed Hamiltonian often simplifies, revealing new insights into the system's behavior. It is essential for understanding phenomena like the formation of polarons, where electrons in a crystal lattice distort the surrounding lattice due to their interaction with phonons.

6.2 Examplary Electronic Polaron Transformation

In this section we will give a short but comprehensive example for a polaron transformation performed for electronic dispersion. Utilizing the complete Hamiltonian introduced earlier, we are able to thoroughly describe and analyze the behavior and properties of this exemplary system. Please note that for the sake of simplicity, we omit the phonon mode index j. It's important to emphasize that while we do not

explicitly write out this index, it still exists and is applicable in our calculations. We employ the transformation to facilitate a unitary mapping of Hamiltonians.

$$\begin{aligned}\widetilde{H} &= e^{-S} H e^{S} \\ &= H + [S,H] + \frac{1}{2}\Big[S,[S,H]\Big] + \mathcal{O}(H^3) \\ &= H_0 + H_{\text{el-ph}} + [S,H_0] + [S,H_{\text{el-ph}}] + \frac{1}{2}\Big[S,[S,H]\Big] + \mathcal{O}(H^3).\end{aligned}$$

Please note, that we omit the above Baker-Campbell-Hausdorff in third order. Subsequently, we define the transformation operator

$$S = -\sum_{\mathbf{kq}} \mathcal{D}_{\mathbf{q}} \left(\frac{1}{E_{\mathbf{k+q}} - E_{\mathbf{k}} + \hbar\Omega} b^{\dagger}_{-\mathbf{q}} + \frac{1}{E_{\mathbf{k+q}} - E_{\mathbf{k}} - \hbar\Omega} b_{\mathbf{q}} \right) a^{\dagger}_{\mathbf{k+q}} a_{\mathbf{k}}. \tag{6.2}$$

As one can easily ascertain, the commutator relation below follows from this transformation

$$[S, H_0] = -H_{\text{ex-ph}}. \tag{6.3}$$

Thus, we obtain the new Hamiltonian

$$\widetilde{H} = H_0 + \frac{1}{2}[S, H_{\text{el-ph}}]. \tag{6.4}$$

Using many-particle Fock states of the unperturbed Hamiltonian, denoted as $|n\rangle \mathrel{\widehat{=}} |\mathbf{k}, n_{\mathbf{q}}\rangle$ with corresponding eigenvalues E_n, we can derive the matrix elements of the operator S in this eigenbasis from Equation (6.3)

$$\begin{aligned}\langle n| SH_0 |m\rangle - \langle n| H_0 S |m\rangle = \langle n| S |m\rangle (E_m - E_n) &= -\langle n| H_{\text{el-ph}} |m\rangle \\ \langle n| S |m\rangle &= \frac{\langle n| H_{\text{el-ph}} |m\rangle}{E_n - E_m}.\end{aligned} \tag{6.5}$$

With this in mind we can use equation (6.3) and insert $\mathbb{1} = \sum_n |n\rangle\langle n|$ which leads to

$$\begin{aligned}\widetilde{H} &= H_0 + \frac{1}{2}\sum_{ln} |l\rangle\langle l| \Big(S H_{\text{el-ph}} - H_{\text{el-ph}} S \Big) |n\rangle\langle n| \\ &= H_0 + \frac{1}{2}\sum_{lmn} \Big(\langle l| S |m\rangle\langle m| H_{\text{el-ph}} |n\rangle - \langle l| H_{\text{el-ph}} |m\rangle\langle m| S |n\rangle \Big) |l\rangle \langle n|, \end{aligned} \tag{6.6}$$

with Eq.(6.5) we obtain the new Hamiltonian [44, 98]

$$\widetilde{H} = H_0 - \frac{1}{2}\sum_{lmn} \langle l| H_{\text{el-ph}} |m\rangle \langle m| H_{\text{el-ph}} |n\rangle \left(\frac{1}{E_m - E_n} - \frac{1}{E_l - E_m}\right) |l\rangle \langle n| . \quad (6.7)$$

In order to obtain an effective Hamiltonian, we perform a trace over the phonons within a bath approximation. As a consequence, the initial states represented as $|n\rangle$ and the final states represented as $|l\rangle$ must maintain the same phonon configuration. This constrains the processes to involve a two-step sequence where a phonon is first absorbed and then subsequently emitted with the same momentum or vice versa (see Fig.6.1).
Additionally, we need to account for energy conservation in these processes. As an example, considering one of these processes, the energy change associated with the absorption of a phonon with energy $\omega_{\mathbf{q}}$ and the subsequent emission of a phonon with the same momentum

$$|n\rangle \mathrel{\widehat{=}} |\mathbf{k}, n_{\mathbf{q}}\rangle \Rightarrow |m\rangle \mathrel{\widehat{=}} |\mathbf{k}+\mathbf{q}, n_{\mathbf{q}} - 1\rangle \Rightarrow |l\rangle \mathrel{\widehat{=}} |\mathbf{k}, n_{\mathbf{q}}\rangle .$$

The energy can be expressed as follows, taking into account both the absorption of a phonon (indicated by $-\omega_{\mathbf{q}}$) and the subsequent reemission of a phonon (indicated by $+\omega_{\mathbf{q}}$)

$$E_m - E_n = E_{\mathbf{k}+\mathbf{q}} - E_{\mathbf{k}} - \omega_{\mathbf{q}} \qquad E_l - E_m = E_{\mathbf{k}} - E_{\mathbf{k}+\mathbf{q}} + \omega_{\mathbf{q}}.$$

This set of assumptions and considerations enables us to compute the expectation values in Eq.(6.7) and ultimately leads us to the final form of the Hamiltonian

$$\widetilde{H} = H_0 - \sum_{\mathbf{k},\mathbf{q}} |\mathcal{D}_{\mathbf{q}}|^2 \left(\frac{n_q}{\Delta E - \omega_{\mathbf{q}}} + \frac{n_q + 1}{\Delta E + \omega_{\mathbf{q}}}\right) a^{\dagger}_{\mathbf{k}} a_{\mathbf{k}}. \quad (6.8)$$

where $\Delta E = E_{\mathbf{k}+\mathbf{q}} - E_{\mathbf{k}}$. It is important to note that we intentionally neglect two-particle processes in our calculations, which result in an effective phonon-mediated electron-electron interaction. This interaction has the potential to lead to attractive electron-electron interactions, ultimately giving rise to the formation of Cooper pairs, a phenomenon extensively studied in the context of superconductivity but beyond the scope of this work.

6.3 Excitonic Polaron Transformation

Expanding upon the theoretical framework introduced earlier, we now extend it to the excitonic context presented in chapter 3. To achieve this, we revisit the exciton-phonon Hamiltonian previously introduced in Eq.(3.10). Since our focus centers on interlayer excitons in the K-valley, particularly within the lowest subband, we simplify the Hamiltonian by omitting the subband indices ν and μ. As a result, the Hamiltonian can be expressed in a more concise form as follows [57, 99]

$$H_{x-ph} = \sum_{\mathbf{Q},\mathbf{q}} D_{\mathbf{q}} X^{\dagger}_{\mathbf{Q}+\mathbf{q}} X_{\mathbf{Q}} (b_{\mathbf{q}} + b^{\dagger}_{-\mathbf{q}}).$$

In this context, $D_{\mathbf{q}}$ represents the exciton-phonon matrix element, characterizing the interaction magnitude between excitons and phonons having momentum $\mathbf{q}$. This coupling strength is determined through the transformation of the relevant electron-phonon matrix element, as obtained from DFT calculations [51], into the excitonic basis (as detailed in section 3.3). Following a similar procedure as in the electronic case, this results, in the low-density limit, in the following Hamiltonian

$$\widetilde{H} = H - \sum_{\mathbf{Q},\mathbf{q}} |D_{\mathbf{q}}|^2 \left(\frac{n_q}{\Delta\mathcal{E} - \omega_{\mathbf{q}}} + \frac{n_{\mathbf{q}} + 1}{\Delta\mathcal{E} + \omega_{\mathbf{q}}} \right) X^{\dagger}_{\mathbf{Q}} X_{\mathbf{Q}}. \tag{6.9}$$

with $n_{\mathbf{q}}$ representing the phonon occupation number and $\Delta\mathcal{E} = \mathcal{E}_{\mathbf{Q}+\mathbf{q}} - \mathcal{E}_{\mathbf{Q}}$. In our model, we only include the coupling to optical phonons $\omega_{\mathbf{q}} = \hbar\Omega$, since the continuous low energy spectrum of acoustic phonons gives rise to short phonon coherence times, which suppresses the coherent hybridization of excitons and phonons. We can identify a polaron renormalized energy as

$$\widetilde{\mathcal{E}}_{\mathbf{Q}} = \mathcal{E}_{\mathbf{Q}} - \sum_{\mathbf{q}} |D_{\mathbf{q}}|^2 \left(\frac{n_q}{\Delta\mathcal{E} - \hbar\Omega} + \frac{n_q + 1}{\Delta\mathcal{E} + \hbar\Omega} \right).$$

Performing a Taylor expansion on the second term for small $\mathbf{Q}$ we obtain

$$\widetilde{\mathcal{E}}_{\mathbf{Q}} = \mathcal{E}_{\mathbf{Q}} - \sum_{\mathbf{q}} |D_{\mathbf{q}}|^2 \left[\frac{n_q}{\mathcal{E}(\mathbf{q}) - \hbar\Omega} \left\{ 1 - \frac{\frac{\hbar^2}{m}\mathbf{Q}\cdot\mathbf{q}}{(\mathcal{E}(\mathbf{q}) - \hbar\Omega)} + \left(\frac{\frac{\hbar^2}{m}\mathbf{Q}\cdot\mathbf{q}}{(\mathcal{E}(\mathbf{q}) - \hbar\Omega)} \right)^2 \right\} \right.$$
$$\left. + \frac{(n_q + 1)}{\mathcal{E}(\mathbf{q}) + \hbar\Omega} \left\{ 1 - \frac{\frac{\hbar^2}{m}\mathbf{Q}\cdot\mathbf{q}}{(\mathcal{E}(\mathbf{q}) + \hbar\Omega)} + \left(\frac{\frac{\hbar^2}{m}\mathbf{Q}\cdot\mathbf{q}}{(\mathcal{E}(\mathbf{q}) + \hbar\Omega)} \right)^2 \right\} \right].$$

Upon integration over $\mathbf{q}$, the contributions linear in $\mathbf{q}$ vanish. Consequently, we are left with two key terms: one responsible for shifting the original exciton energy, denoted as $\mathcal{E}_{\text{Polaron}}$ (representing the polaron shift), and the other term corresponds to a mass renormalization factor denoted as λ. In a more concise form, we can express the new energy as

$$\widetilde{\mathcal{E}}_{\mathbf{Q}} = -\mathcal{E}_{\text{Polaron}} + \frac{\hbar^2\mathbf{Q}^2}{2m^*}, \tag{6.10}$$

with $m^* = (1 + \lambda)m$. The individual terms can be specified as follows

$$\mathcal{E}_{\text{Polaron}} = \sum_{\mathbf{q}} |D_{\mathbf{q}}|^2 \left(\frac{n_q}{\mathcal{E}(\mathbf{q}) - \hbar\Omega} + \frac{(n_{\mathbf{q}} + 1)}{\mathcal{E}(\mathbf{q}) + \hbar\Omega} \right) \tag{6.11}$$

$$\lambda = \frac{2\hbar^2}{m} \sum_{\mathbf{q}} |D_{\mathbf{q}}|^2 \mathbf{q}^2 \left(\frac{n_q}{(\mathcal{E}(\mathbf{q}) - \hbar\Omega)^3} \to 0 + \frac{(n_{\mathbf{q}} + 1)}{(\mathcal{E}(\mathbf{q}) + \hbar\Omega)^3} \right). \tag{6.12}$$

Observing the mass renormalization term, it becomes apparent that the first term vanishes during the integration over $\mathbf{q}$. This can be confirmed through a residue analysis. With the incorporation of polaron-renormalized energies we can now conduct an in-depth analysis of the influence of polaronic mass enhancements on the moiré exciton band structure. We commence by exploring the twist angle dependent effects of polaron-induced mass enhancement on the moiré exciton band structure. Our findings reveal a conspicuous trend of band flattening, signifying a significant reduction in bandwidth, as illustrated in Figs. 6.2(a)-(b). Notably, we observe that the absolute change in bandwidth diminishes by roughly 6 meV at larger twist angles (3°), while smaller twist angles (1°) exhibit changes as small as 20 μeV, attributed to their inherently flatter band structure.

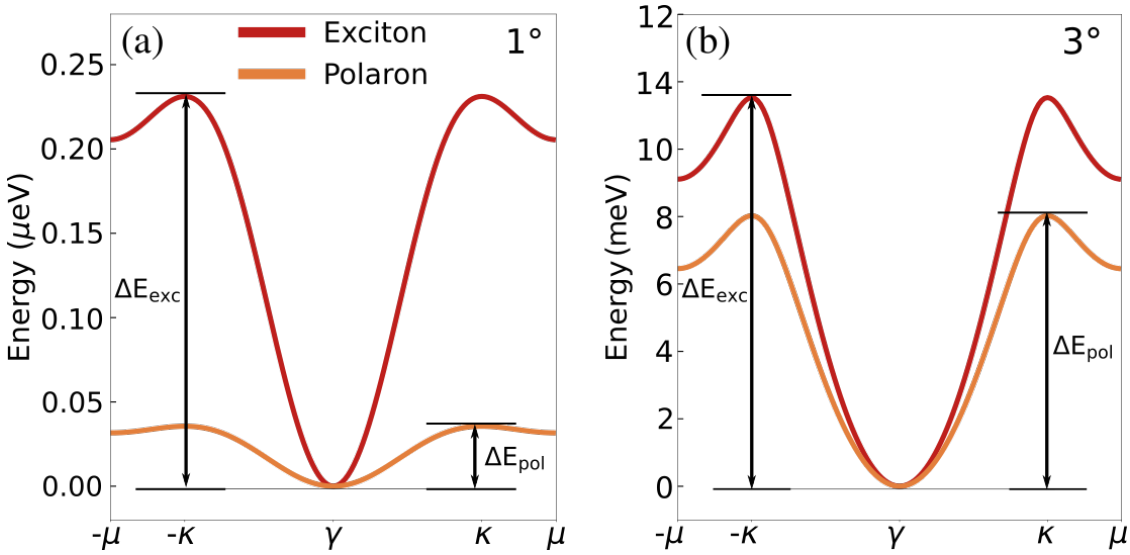

Figure 6.2: (a)-(b): A comparison of the lowest moiré exciton subband structure in the twisted MoSe2/WSe2 heterostructure, considering the incorporation of polarons (highlighted in orange), alongside the purely excitonic scenario without phonon interactions (depicted in red). The data is normalized to their respective minima. The impact of this interaction is quantified by examining changes in both the exciton energy (ΔE_{exc}) and the polaron bandwidth (ΔE_{pol}).

We further scrutinize the impact of temperature on the polaron-induced bandwidth alterations. To achieve this, we calculate the relative change in bandwidth, denoted as $\Delta = 1 - \Delta E_{\mathrm{pol}}(T)/\Delta E_{\mathrm{pol}}(0)$, with $\Delta E_{\mathrm{pol}}(0)$ representing the polaronic bandwidth at T=0K as a reference (refer to Fig. 6.3). Our observations reveal an intriguing temperature-dependent behavior stemming from elevated phonon occupation numbers $n_{\mathbf{q}}$ at higher temperatures. Consequently, we discern an increase in effective excitonic mass, as elucidated by Eq.(6.10), which promotes the pronounced flattening of the band structure (also evident in Fig. 6.2(a)-(b)).
The most substantial change in bandwidth occurs at elevated temperatures and smaller twist angles, resulting in a remarkable 50% increase at 1° and room temperature. In contrast, at 3°, the relative change is notably smaller, at approximately 10%. Despite the fact that polaron formation is not intrinsically dependent on the twist angle, the interaction between polarons and the moiré potential imparts a pronounced twist-angle dependence on bandwidth. This behavior emerges because minor alterations in band flattening, attributed to polaron formation, engender a

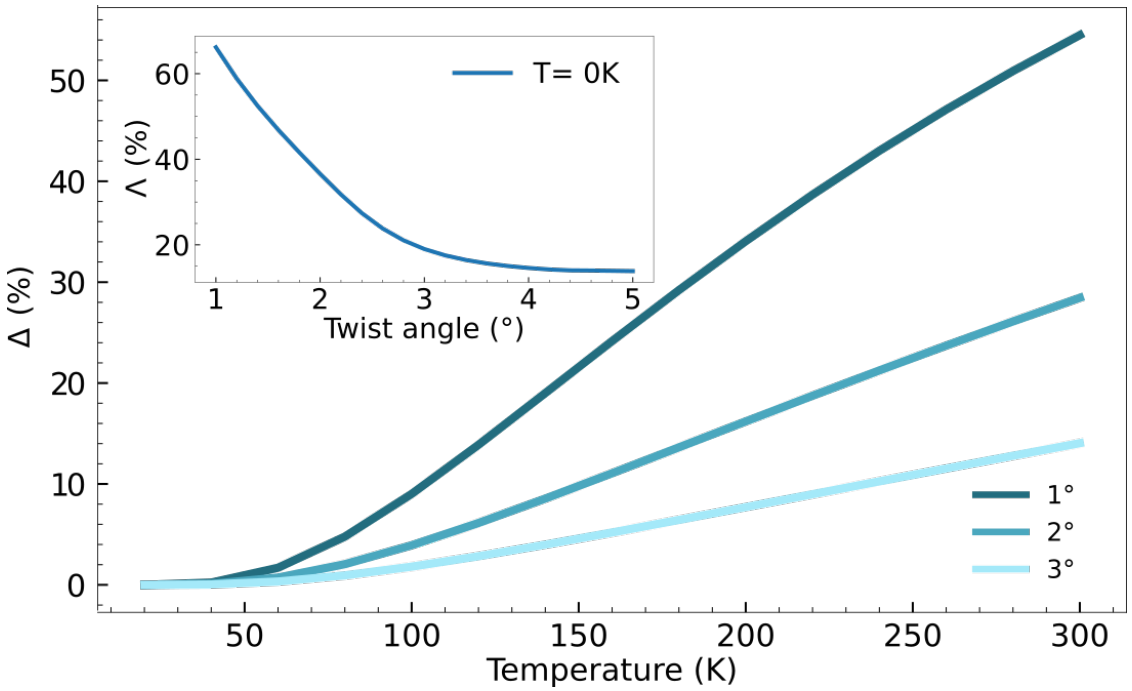

Figure 6.3: The figure displays the relative change in polaron bandwidth, denoted as $\Delta = 1 - \Delta E_{pol}(T)/\Delta E_{pol}(0)$, as a function of temperature for varying twist angles, with $\Delta E_{pol}(T = 0)$ as the reference point. Notably, at a twist angle of 1°, a substantial polaron bandwidth change exceeding 50% is observed. The inset provides further insight, illustrating the twist-angle-dependent relative change in polaron bandwidth, denoted as $\Lambda = 1 - \Delta E_{pol}(0)/\Delta E_{exc}(0)$, concerning the exciton bandwidth at a fixed temperature of T=0 K.

substantial relative change in already considerably flat bands. Conversely, in cases with larger bandwidths, even slight changes in band structure yield less pronounced effects.

These observations underscore that smaller twist angles are considerably more influenced by polaron formation. This effect is emphasized when we examine the relative change in band structure compared to the unperturbed exciton ($\Lambda = 1 - \Delta E_{pol}/\Delta E_{exc}$), as illustrated in the inset of Fig. 6.3. The change in bandwidth is particularly pronounced at smaller twist angles, with relative changes exceeding 60% (at T = 0K and 1°). As the twist angle increases, the magnitude of this effect diminishes significantly, with differences dropping below 20%. While the polaronic mass enhancement is generally independent of the twist angle, its impact on moiré

trapping is highly contingent on the length scale of the trapping potential. The previous observations of exciton delocalization at larger twist angles [23, 30] stem from the zero-point energy of quantum-confined states. As the confinement length scale decreases (twist angle increases), the zero-point energy of the ground state exciton rises. At a critical confinement length, the zero-point energy surpasses the depth of the moiré potential, leading to exciton delocalization and an increase in bandwidth. However, the zero-point energy of a quantum-confined state is inversely proportional to particle mass. Consequently, the polaronic mass enhancement exerts different effects on moiré bandwidth in the trapped regime (small twist angles) compared to the delocalized regime (large twist angles).

7

Spatio-Temporal Exciton Dynamics

In the preceding section, we explored the intricacies of exciton energy landscapes, highlighting its reliance at the small angle limit on hopping mechanisms within the moiré potential. To comprehensively capture and elucidate these hopping dynamics, we introduce a Hubbard-like model—a well-established theoretical framework commonly employed to analyze charge carriers' motion within lattices. This theoretical framework has been successfully applied to describe the dynamics of bosonic atoms within optical lattices, as demonstrated in studies such as [100, 101]. Additionally, it has played a crucial role in modeling quantum phase transitions, specifically those from superfluid to Mott insulators [100, 102]. Furthermore, we aim to obtain a deeper understanding of exciton propagation by deriving a numerical exact solution, which allows us to extract the time-dependent excitonic wavefunction, providing a comprehensive depiction of the spatiotemporal dynamics governing exciton motion. Through the interplay of these two models, we navigate the complex landscape of exciton transport, identifying and characterizing distinct transport regimes. Our analysis sheds light on the nuanced behaviors exhibited during exciton propagation within the moiré potential, unraveling a spectrum of transport phenomena. In the subsequent sections, we delve into a detailed discussion of these different transport regimes, offering insights into the underlying mechanisms and their implications for practical applications.

7.1 Tight Binding Method (Wannier states)

In the realm of solid-state physics, various approaches are employed to model binding mechanisms. One such approach is the quasi-free electron model, where we assume a weak effective periodic potential generated by atoms. This allows for a qualitative understanding of the energy landscape within solids. We will utilize this method in

Sec. 2.3. However, this assumption breaks down in the case of localized electrons, where the interaction with atoms becomes strong, binding the electron closely to the atom itself. This scenario is aptly described by the tight-binding model.
In the initial step, we consider an isolated atom at position $\mathbf{R}$, leading to the atomic problem [44]

$$\Big(\frac{\mathbf{p}^2}{2m} + V(\mathbf{r}-\mathbf{R})\Big)\phi(\mathbf{r}-\mathbf{R}) = E\phi(\mathbf{r}-\mathbf{R}).$$

Here, $V(\mathbf{r}-\mathbf{R})$ represents the atomic potential felt by an electron at position $\mathbf{R}$. Bringing multiple atoms closer together results in the crystal Hamiltonian. While, in the free electron case, we could express atomic wave functions in a Bloch basis, the constructed Bloch states, denoted as $\psi_{\mathbf{k}}(\mathbf{r})$, in the tight-binding model do not form an orthonormal system [44]. Consequently, an additional basis transformation is required. The orthonormal basis in the tight-binding model is represented by the Wannier basis, which can be constructed from the aforementioned Bloch states as follows

$$W(\mathbf{r}-\mathbf{R}) = \frac{1}{\sqrt{N}}\sum_{\mathbf{k}} e^{-i\mathbf{k}\cdot\mathbf{R}}\psi_{\mathbf{k}}(\mathbf{r}). \tag{7.1}$$

In Section 7.2, we will explore how interactions within a moiré potential can lead to strongly localized states. Thus, the tight-binding model introduced here in an atomic context can also be applied in interaction with a periodic moiré potential.

7.2 Hubbard-like Model

As demonstrated in Sec. 5.3, the twist angle within heterostructures significantly influences the energy landscape. We have previously noted that these distinct energy configurations characterize trapped states for small angles and delocalized excitonic states for larger twist angles. Considering the hindrance of excitonic movement due to the decrease in group velocity, particularly pronounced at very small angles where the exciton band structure is flat (refer to Sec. 5.3), suggesting a transport dominated by hopping (see Fig. 7.1).
To address this, we introduce a moiré inter-cell tunneling model, a robust approach

for calculating the dynamics of strongly localized, hopping-driven states. This modeling technique has previously found success in describing the dynamics of bosonic atoms in optical lattices [100, 101] and quantum phase transitions from superfluid to Mott insulators [100, 102].

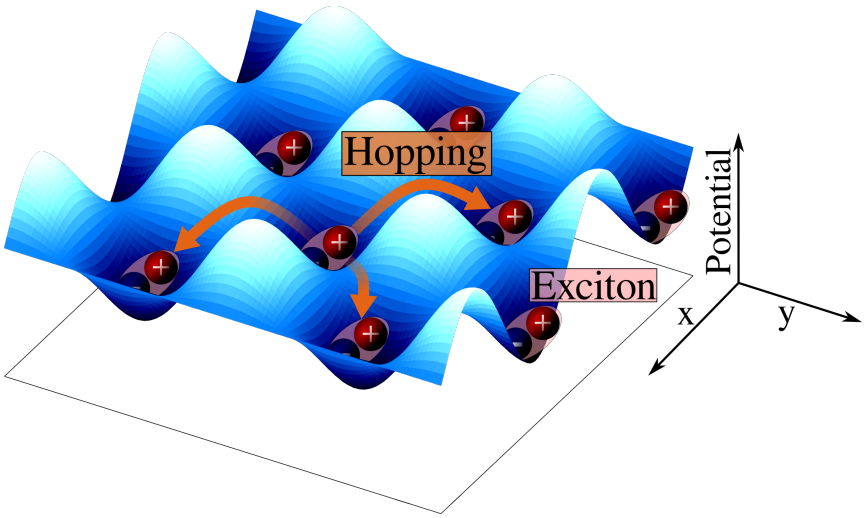

Figure 7.1: Illustration of the hopping movement of excitons inside the moiré potential minima.

For this purpose, we exploit the already introduced moiré exciton Hamiltonian in Eq.(5.10)

$$H = \sum_{\mu\mathbf{Q}} E_{\mu\mathbf{Q}} Y^{\dagger}_{\mu\mathbf{Q}} Y_{\mu\mathbf{Q}}.$$

For simplicity, let's consider a single layer index L. By transforming the operators into a Wannier basis (c.f. Sec. 7.1), denoted as $b^{\dagger}_{\nu,n} = \frac{1}{\sqrt{N}} \sum_{\mathbf{Q}} \exp(i\mathbf{Q}\cdot\mathbf{R}n) Y^{\nu\dagger}_{\mathbf{Q}}$, where $\mathbf{R}_n$ represents the n-th moiré superlattice minimum. In this basis, the Hamiltonian operator is expressed as

$$H = \sum_{\mu\mathbf{Q}} \sum_{n,m} \frac{1}{N} e^{i\mathbf{Q}\cdot(\mathbf{R}_m - \mathbf{R}_n)} E_{\mu\mathbf{Q}} b^{\dagger}_{\mu,n} b_{\mu,m}.$$

This can be rewritten as follows

$$H = \sum_{n,m,\mu} t^{\mu}_{n,m} b^{\dagger}_{\mu,n} b_{\mu,m}. \tag{7.2}$$

Here, $t^{\nu}_{n,m}$ represents the hopping term, and it can be computed by evaluating the overlap of the Wannier wavefunctions $W_n(\mathbf{r}) = 1/\sqrt{N} \sum_{\mathbf{Q},s} e^{-i\mathbf{Q}\cdot\mathbf{R}_n} c^{\nu}_s(\mathbf{Q}) \exp\{-i(\mathbf{Q}+\mathbf{G}_s)\cdot\mathbf{r}\}$ at different lattice positions n and m. This matrix element yields

$$t^{\mu}_{n,m} = \int d^2r \; W^*_n(\mathbf{r}) H W_m(\mathbf{r}) = \frac{1}{N} \sum_{\mathbf{Q}} e^{i\mathbf{Q}\cdot(\mathbf{R}_m - \mathbf{R}_n)} E_{\mu\mathbf{Q}}. \tag{7.3}$$

The band structure $E_{\mu\mathbf{Q}}$ is inherently influenced by the twist angle. Consequently, the hopping element or hopping term also exhibits a dependency on the twist angle.

7.2.1 Hopping rate

The hopping matrix elements offer valuable insights into the transport properties of our system. To delve deeper into this aspect, we will examine in detail the dependence of these matrix elements on the twist angle.
Figure 7.2 provides a representative depiction of the intralayer hopping term with respect to the twist angle θ. The ground state ($\mu = 0$) is represented by green lines, while the excited state ($\mu = 1$) is depicted in blue. The analysis accounts for both nearest neighbor (solid lines) and next-nearest neighbor (dashed lines) interactions. At small θ, the hopping term approaches zero, signifying complete exciton trapping. This occurs because, at these angles, there is minimal overlap of excitonic orbital functions, resulting in negligible transport. The moiré superlattice constant increases for small twist angles, creating a substantial potential barrier for tunneling between neighboring sites. Conversely, at larger twist angles, the hopping term steadily increases, mirroring the growing delocalization of Wannier orbitals. This results in an expanded orbital overlap, as illustrated in the insets of Fig. 7.2 for $\theta = 1°$ and $\theta = 3°$, showing the orbitals of two neighboring sites within the moiré potential. This trend aligns with the twist-angle evolution of the moiré subbands, as demonstrated in Fig.5.4(a) and (b). For 1°, a flat band structure is observed, corresponding to negligible group velocity. In contrast, for 3°, the bands exhibit a parabolic dispersion, indicating increased mobility.
An noteworthy distinction between nearest-neighbor (NN) and next-neighbor (2NN)

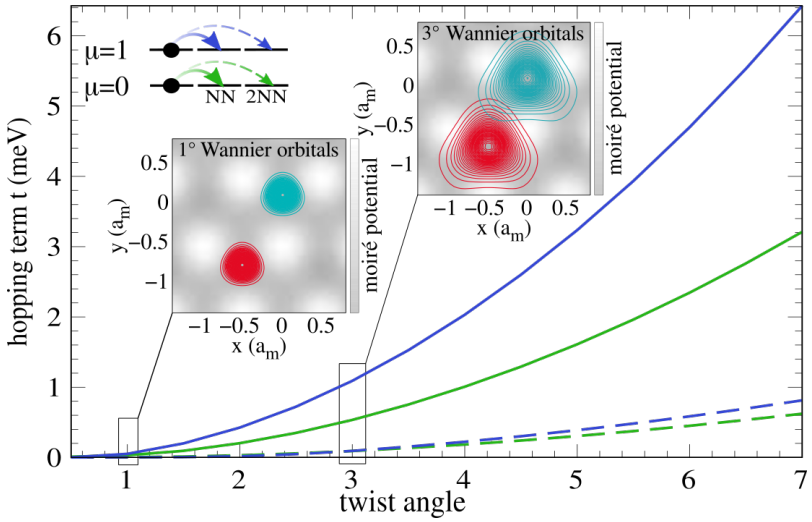

Figure 7.2: Hopping term over the twist angle θ for nearest neighbor (NN) and next-neighbor (2NN) interaction. We depict the hopping term for the ground and first excited exciton states, i.e. $\mu = 0, 1$. Due to the more pronounced overlap between the Wannier wavefunction (insets) the nearest neighbor interaction is the dominant term for the hopping interaction.

hopping (solid vs dashed lines) is the rate of their increase concerning the twist angle, as shown in Fig. 7.2. Hopping due to nearest-neighbor interaction increases more rapidly owing to the larger overlap of directly adjacent sites. Furthermore, 2NN hopping becomes significant only at larger twist angles, being negligible for angles smaller than $\theta < 2°$. Considering the hopping term for different exciton subbands, the lowest and first excited states (green and blue lines) exhibit a similar overall behavior. However, the first excited state demonstrates more efficient hopping due to its less stringent binding and more delocalized wave functions, resulting in a larger overlap.

7.2.2 Polaron impact on hopping rates

In the realm of exciton transport, the hopping rate $|t|$ (as indicated in Eq.(7.3)), as explored in the preceding section, emerges as a critical parameter influencing the propagation of excitons. Now, incorporating the polaron interaction discovered in Section 6 between excitons and phonons, we gain the capability to delineate the impact of this significant interaction on the hopping rate and, consequently, on the

excitonic transport properties. As previously established, focusing on the nearest-neighbor interactions, which are paramount due to their significantly larger wavefunction overlap, reveals that the hopping rate is directly tied to the moiré exciton band structure and the overlap of the Wannier wavefunctions (refer to Eq.(7.3)). With the introduction of phonon interaction, this relationship remains valid. However, the intriguing question arises: How does the increased effective excitonic mass, resulting from the interaction with phonons, influence the overall mobility? In this

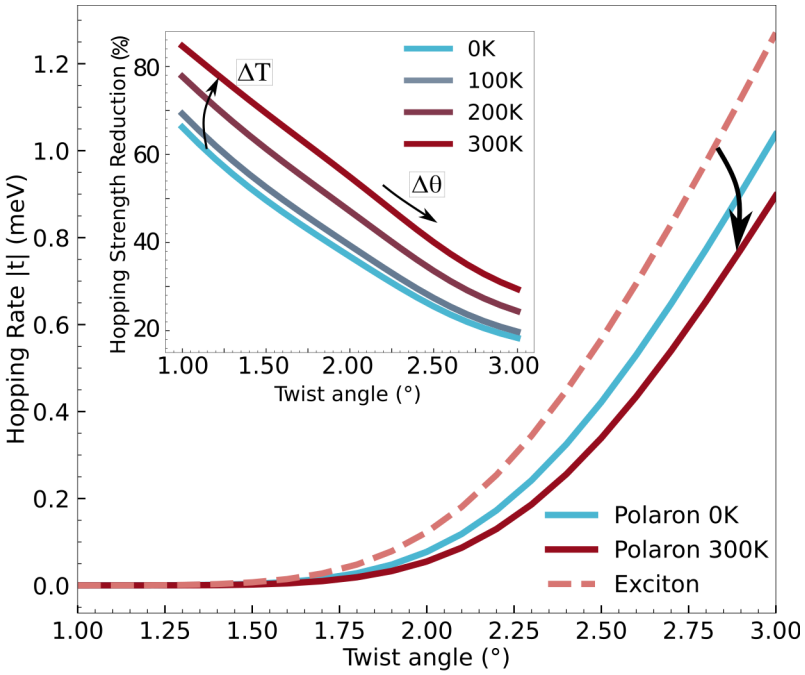

Figure 7.3: The hopping rate $|t|$ decreases significantly with polarons present, especially at smaller twist angles and room temperature, where the reduction exceeds 80%.

analysis, we examine once more the behavior of the hopping rate ($|t|$) as a function of the twist angle. The dashed line in Fig. 7.3 represents the nearest-neighbor hopping for an interlayer exciton in a twisted heterostructure. Similar to intralayer excitons (cf. Figure 7.2), at small angles, the hopping is negligible, indicating flat moiré exciton bands and trapped states. As the twist angle increases, excitons gain more mobility, consistent with the well-established trend for intralayer excitons.
However, the introduction of polarons transforms this behavior. The solid lines in

Fig. 7.3 demonstrate a significant reduction in the hopping rate due to polarons, attributed to the polaron-induced mass enhancement hindering exciton motion. Even at T=0K, polarons lead to a clear decrease in the hopping rate (blue line) compared to the purely excitonic case (dashed line). With increasing temperature, exciton-phonon interaction becomes more efficient, resulting in a larger mass enhancement and a greater reduction in the hopping rate (red line). Equation (6.10) establishes a direct relationship between the polaron mass and the phonon occupation number, implying that the exciton mass increases with rising temperature, hindering exciton mobility. Therefore, phonon-mediated interaction plays a pivotal role in modifying the material's transport characteristics.
Moreover, we observe an angle-dependent impact of polarons on the hopping rate. The absolute decrease in the rate due to polarons is more substantial at higher twist angles, as shown in Fig. 7.3. There is a general increase in exciton mobility with an increasing twist angle, reflecting the diminishing effect of the moiré potential. Interestingly, polarons counteract this trend by enhancing the effective exciton mass and reducing the exciton bandwidth (Figs. 6.2 (a)-(b)), shifting the transition from moiré-trapped to delocalized phases [23] to larger twist angles.
In the inset of Fig. 7.3, we illustrate the relative polaron-induced changes in the hopping rates (compared to the free excitonic case) as a function of the twist angle for various fixed temperatures. Even at T=0K, the polaron effect is pronounced, leading to a substantial deviation from the free exciton hopping rate due to self-interaction via virtual phonons [103]. These deviations exceed 60% at 1°, underscoring the significant reduction in the hopping rate and emphasizing the pivotal role of polarons in altering the transport properties of excitons in TMD-based materials. As the temperature increases, the contribution of thermal energy to the effective exciton mass becomes relevant through the increased phonon occupation in Eq.(6.10). This results in even larger changes in the hopping rates, with relative deviations exceeding 80% at 1° from the undisturbed excitonic case at elevated temperatures. While the absolute rate reduction was found to increase with the twist angle (main Fig. 7.3), the relative difference is most pronounced at small twist angles (inset of Fig. 7.3).
With an increasing twist angle, the band flattening becomes less pronounced due to a stronger localization of the excitonic wavefunction in momentum space, resulting in a reduced influence of the moiré potential. Specifically, the reduction in the hopping rate at a twist angle of 3° is approximately 20% at T=0K and up to 30% at T=300K, in contrast to the more substantial reductions observed at 1° (>60% and >80%, respectively). This trend underscores the intriguing role that the twist angle

plays in moiré exciton transport.

7.3 Exact Solution

After identifying the excitonic eigenstates within the moiré potential in Chapter 5, the computation of the time-dependent real-space wave function for a given initial distribution becomes feasible through the utilization of the time evolution operator. The general form of a time-dependent wave function can be articulated as follows

$$|\psi(t)\rangle = U(t)\,|\psi(0)\rangle\,.$$

In the context of the Schrödinger picture, the evolution of quantum states over time is dictated by the Hamiltonian operator. This leads to the derivation of an exponential expression that encapsulates the time-dependent evolution of a quantum state. The time evolution of a quantum state $|\psi(t)\rangle$ is governed by the Hamiltonian operator H, and it is expressed through the following exponential form

$$|\psi(t)\rangle = e^{-\frac{i}{\hbar}Ht}\,|\psi(0)\rangle\,.$$

Here, $|\psi(0)\rangle$represents the state at the initial time, t denotes the elapsed time, H is the Hamiltonian operator. This exponential term embodies the time evolution operator in the Schrödinger picture. By incorporating the diagonalized moiré Hamiltonian as given in Equation (5.10), we arrive at the following expression

$$|\psi(t)\rangle = e^{-\frac{i}{\hbar}\sum_{\mu'\mathbf{Q}'} E_{\mu'\mathbf{Q}'} Y^{\dagger}_{\mu'\mathbf{Q}'} Y_{\mu'\mathbf{Q}'} t}\,|\psi(0)\rangle\,.$$

This expression reflects the evolution of the quantum state within the moiré potential, shedding light on the intricate dynamics governed by the diagonalized Hamiltonian. By incorporating the identity operator $\sum_{\mu\mathbf{Q}} |\mu\mathbf{Q}\rangle\langle\mu\mathbf{Q}|$, the equation for the time-dependent excitonic wavefunction in real space can be expressed as follows

$$\psi(\mathbf{r},t) = \sum_{\mathbf{Q},\nu} \tilde{\psi}_{\nu}(\mathbf{Q},0)\chi_{\mathbf{Q},\nu}(\mathbf{r}) \exp\left(-\frac{i}{\hbar}E^{\nu}_{\mathbf{Q}}t\right). \tag{7.4}$$

Here, we utilize the the Bloch wavefunction $\chi_{\mathbf{Q},\nu}(\mathbf{r}) = \sum_s c^{\nu}_s(\mathbf{Q})\exp(-i(\mathbf{Q}+\mathbf{G}_s)\mathbf{r})$ and the projection of the initial state $\tilde{\psi}_{\nu}(\mathbf{Q},0) = \langle\nu,\mathbf{Q}|\psi(0)\rangle$. In experimental scenarios, Gaussian-shaped laser pulses are commonly employed to shape the initial exciton

distribution, with the real space width on the order of the excitation wavelength, typically in the μm-range [14]. This width is large compared to the moiré lattice vector ($<$ 100nm for the twist angles $> 1^\circ$ considered in this work [104]). Consequently, a Taylor expansion of the twist angle dependent band structure around the γ-point is performed, yielding isotropic and parabolic bands with $E_Q \approx \hbar^2 Q^2/(2m_{\text{eff}})$, where $1/m_{\text{eff}} = 1/\hbar^2 \partial^2 E_Q/\partial Q^2$ represents the effective mass. Within this quadratic approximation, the integral in Eq.(7.4) can be solved analytically, leading to the exciton density distribution.

$$\rho(\mathbf{r}, t) = \frac{1}{2\pi\sigma^2(t)} \exp\left(-\frac{\mathbf{r}^2}{2\sigma^2(t)}\right). \tag{7.5}$$

Considering the time-dependent variance $\sigma^2(t) = \sigma_0^2\left(1 + 4\hbar^2 t^2/(m_{\text{eff}}^2\sigma_0^4)\right)$, where σ_0^2 represents the variance of the initial density distribution, the numerical computation of the time evolution of the wave packet is performed using the full band structure $E_{\mathbf{Q}}$ and the exact expression for the wave function given in Eq.(7.4). Therefore, instead of relying solely on Eq.(7.5), we are able to give a more comprehensive analysis of the moiré exciton propagation in experimentally relevant situations by comparing the obtained results from both equation. This enables us to extract an effective mass for the propagation of moiré excitons. This analysis provides valuable insights into the dynamic behavior of moiré excitons in experimental conditions, offering a quantitative measure of their effective mass under the influence of the moiré potential.

7.4 Heisenberg Equation of Motion and Dispersion Parameter

In the context of our investigation, we employ two different approaches to study the spatiotemporal dynamics of moiré excitons. Within the approximation we introduced in Sec 7.2, we calculate the exciton density for the lowest exciton subband ($\mu = 0$) in the Wannier basis. The exciton density $\rho(\mathbf{r}, t)$ is defined as the expectation value

of the density operator, given by

$$\rho(\mathbf{r},t) = \langle \psi^\dagger(\mathbf{r})\psi(\mathbf{r})\rangle = \sum_{n,m} W_m^*(\mathbf{r}) W_n(\mathbf{r}) \rho_{nm}(t),$$

where $\psi^\dagger(\mathbf{r}) = \sum_n W_n(\mathbf{r}) b_n^\dagger$ are the field operators expressed in terms of Wannier orbitals. The density matrix ρ_{nm} governs the temporal evolution of the exciton density and is determined by solving the Heisenberg equation of motion

$$\dot{\rho}_{nm} = -\frac{i}{\hbar} \sum_i \left(t_{mi}\rho_{ni} - t_{in}\rho_{im} \right). \tag{7.6}$$

To quantify the transport behavior for both trapped and delocalized excitons, we utilize the second central moment, $\sigma^2(t) = \int d^2r \mathbf{r}^2 \rho(\mathbf{r},t)$, of the exciton distribution. This variance provides a measure of how much a given distribution broadens its width within a specific time period. While this quantity already holds intrinsic value, it is commonly employed to define a dispersion length. The dispersion length is defined as $\xi(t) = \sqrt{\sigma^2(t) - \sigma_0^2}$ offering insight into the characteristic length over which dispersive effects become significant. Here, σ_0^2 represents the variance of the initial density distribution [105]. To quantify the dispersion and characterize the rate of change of the dispersion length, we introduce a parameter α, defined as the time derivative of the dispersion length, and we refer to it as the dispersion velocity

$$\alpha = \frac{\sigma_0^2}{2} \partial_t \xi(t). \tag{7.7}$$

For a parabolic dispersion (cf. Eq. (7.5)), $\alpha = \hbar/m_{\text{eff}}$ allowing for the unambiguous determination of the effective mass m_{eff} as a function of the twist angle. To ensure comparability between the tunneling model and the exact solution, both simulations are initialized with conditions where only the lowest moiré subband is occupied, employing a superposition of ground state Wannier orbitals with a Gaussian envelope

$$\rho_{nm}(t=0) = \delta_{nm} \mathcal{G}(\sigma_0, |\mathbf{R}_n - \mathbf{R}_0|),$$

and

$$\tilde{\psi}_\nu(\mathbf{Q},0) = \delta_{\nu,0} \int d^2r \chi^*_{\mathbf{Q},\nu}(\mathbf{r}) \sqrt{\mathcal{G}(\sigma_0, r)},$$

where $\mathcal{G}(\sigma_0, r)$ is a Gaussian envelope with width σ_0. This comprehensive approach enables a detailed investigation of the nuanced spatiotemporal behavior of moiré excitons under different approximations, offering valuable insights into their transport dynamics.

7.5 Dispersive and Hopping Regime

In the upcoming analysis, we delve into distinct transport regimes within TMD heterostructures featuring a moiré potential that can be tuned by the twist angle. Figure 7.4 visually captures the spatiotemporal exciton dynamics using the precise expression from Eq. (7.4) for two varying twist angles. The background contour lines depict the corresponding moiré potentials, illustrating a reduction in supercell size with an increase in the twist angle. For a small twist angle of $\theta = 2°$, our observations reveal that only a few moiré sites are initially occupied at $t = 0$fs, and these sites appear almost isolated and well-localized. In contrast, when considering a larger twist angle of $\theta = 5°$ with the same initial Gaussian distribution, a significantly larger number of sites are excited, indicating a more delocalized exciton distribution. As time progresses to $t = 2.4$ps, we observe a noticeable broadening of the exciton distribution for both twist angles. However, a distinct difference in exciton transport behavior becomes evident. For the smaller twist angle, exciton occupation remains localized at individual sites, while for the larger angle, excitons propagate in various directions. To quantify the propagation rate and gain a deeper understanding of the different characteristics of these distinct exciton transport regimes, we introduced the dispersion parameter α in Eq.(7.7). This parameter provides valuable insights into the dynamics of exciton dispersion, allowing us to analyze and compare the transport regimes under different twist angles.

The dispersion parameter α serves as a constant of motion, offering a quantification of the propagation velocity. This parameter allows us to explore and compare the efficiency of exciton transport across different regimes. Figure 7.5 illustrates α as a function of the twist angle θ, extracted from the exact solution (red solid line), the solution for completely free excitons (dashed line), and the tunneling solution

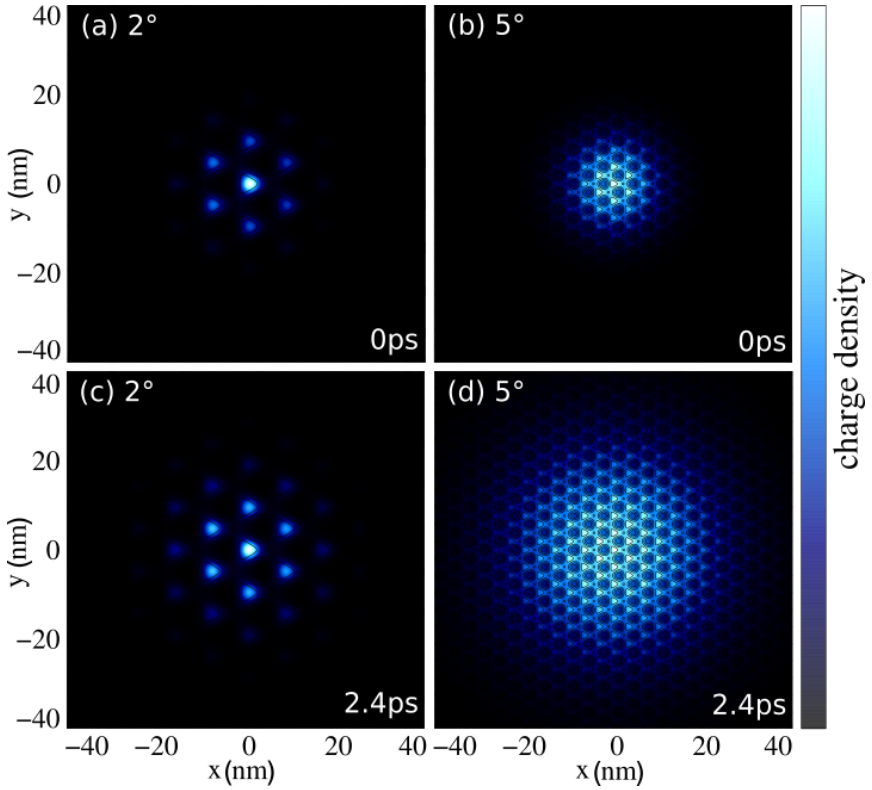

Figure 7.4: Exciton propagation in a twisted $MoSe_2/WSe_2$ heterostructure. (a)-(b) The initial exciton density distribution at 2° and 5°, respectively. The contour lines represent the moiré potential. (c)-(d) Exciton distribution after 2.4ps. For smaller twist angles excitons are strongly localized leading to a suppressed propagation compared to larger angles, where the Wannier orbitals have a larger overlap.

(green line). Notably, we observe a rapid increase in the dispersion parameter α up to a value of approximately 0.25 nm^2/fs, which is reached at a twist angle of around 4°. As the twist angle continues to increase beyond this point, α remains constant, reflecting the consistent dispersion parameter for free excitons (depicted by the dashed line). In this scenario, the exciton distribution becomes delocalized over a large number of supercells, closely resembling the effective mass limit. This behavior is evident in the inset for 7° in Fig. 7.5. Exciton propagation in a moiré potential with a large twist angle mirrors the dispersion of a quantum-mechanical wave packet. Accordingly, we denote this transport regime as dispersive.

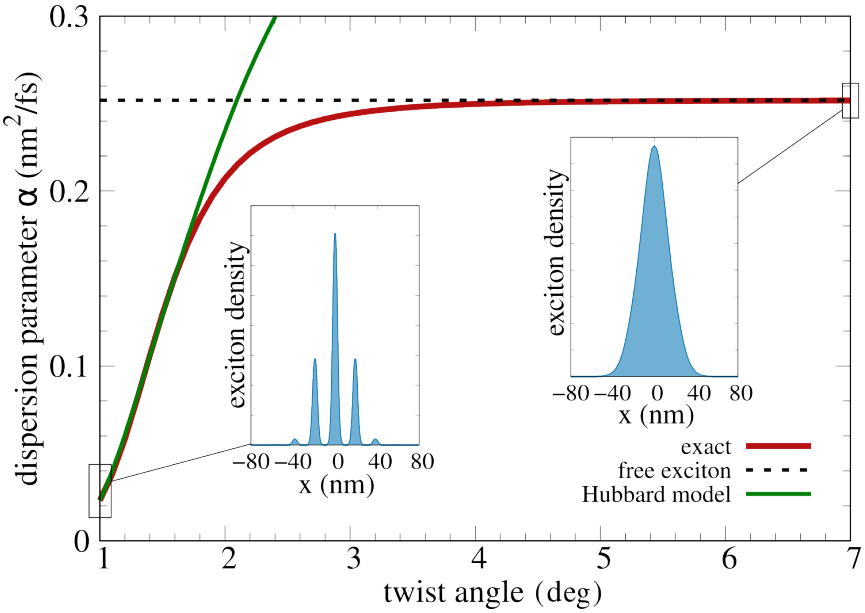

Figure 7.5: Dispersion parameter α plotted against the twist angle θ, providing a direct comparison between the exact numerical solution for exciton propagation in a moiré potential (red line), the moiré tunneling model, and the free-exciton solutions. The exact solution converges to the free solution (dashed line) for $\theta > 4°$, representing the dispersive regime characterized by a delocalized exciton distribution (as shown in the inset at 7°). As the twist angle decreases to $\theta > 1.8°$, the exact solution transitions to the tunneling solution, indicative of a localized exciton distribution (as illustrated in the inset at 1°).

For smaller twist angles, the exact solution distinctly diverges from the free solution and transitions into the tunneling solution (depicted by the green line) for $\theta > 1.8°$. In this range, the efficiency of propagation is significantly reduced, as also evident in Fig. 7.4. At a twist angle of 1°, the dispersion parameter has dropped to more than one order of magnitude, reaching $\alpha \approx 0.023$ nm^2/fs. This pronounced deceleration in exciton transport velocity stems from the band flattening in the exciton dispersion (see Fig. 5.4). This corresponds to trapped exciton states in real space, resulting in a substantially reduced group velocity v_G. Consequently, for small twist angles, exciton propagation is markedly slowed down [23].
In this particular regime, we observe a highly localized exciton distribution (refer to the inset for 1° in Fig. 7.5). Continuous and regular exciton propagation is not feasible; instead, it necessitates hopping between different, largely isolated moiré

sites. Consequently, we denote this behavior as a hopping regime. The moiré tunneling model proves to be a suitable representation to describe this hopping behavior. Notably, the nearest neighbor approximation (green line) aligns perfectly with the exact solution (red line) for small twist angles $\theta < 1.8°$. The dispersion parameter exhibits an increase with the angle, indicating that the overlap of exciton wavefunctions becomes larger, leading to a more efficient hopping term. However, for larger twist angles $\theta > 1.8°$, a distinct deviation from the exact solution becomes evident. Hence, we conclude that the hopping model, formulated in the Wannier basis and assuming that nearest neighbor hopping is the sole efficient channel, is excellent for small angles characterized by localized states. Nevertheless, this assumption fails for larger angles where states are strongly delocalized.

7.5.1 Moiré Exciton Mass

In the context of an external periodic potential, excitons exhibit Bloch wave-like propagation akin to crystal electrons. For sufficiently large wavepackets compared to the cell size, this propagation can be conceptualized as a variation in effective mass. The effective masses are contingent on the surrounding potential, which, in monolayers, arises from the atomic lattice. However, in heterostructures, the exciton mass undergoes natural changes due to the moiré potential, making it notably sensitive to the twist angle. While one could potentially derive the effective mass by interpolating the energy dispersion, such a mass would represent the band curvature only within a specific momentum range.

In contrast, by harnessing the definition of the dispersion parameter α in Eq.(7.7), we derive a more general and transport-relevant effective mass, denoted as

$$m_{\text{eff}}(\theta) = \hbar/\alpha(\theta). \tag{7.8}$$

For larger angles $\theta > 4°$, the effective exciton mass converges toward the value of the free exciton mass (with a deviation of $< 1\%$ for $\theta > 4°$), as illustrated in Fig. 7.6. However, upon decreasing θ, a significant surge in the effective mass by nearly one order of magnitude is evident at 1°. This enhancement mirrors the band flattening observed in the excitonic band structure in the presence of a moiré potential at small twist angles (refer to Fig. 5.4). In scenarios with completely flat bands, the effective mass would theoretically approach infinity. Nonetheless, for angles smaller than 1°, considerations of atomic reconstruction effects [106] become pertinent, although such effects are beyond the scope of this study.

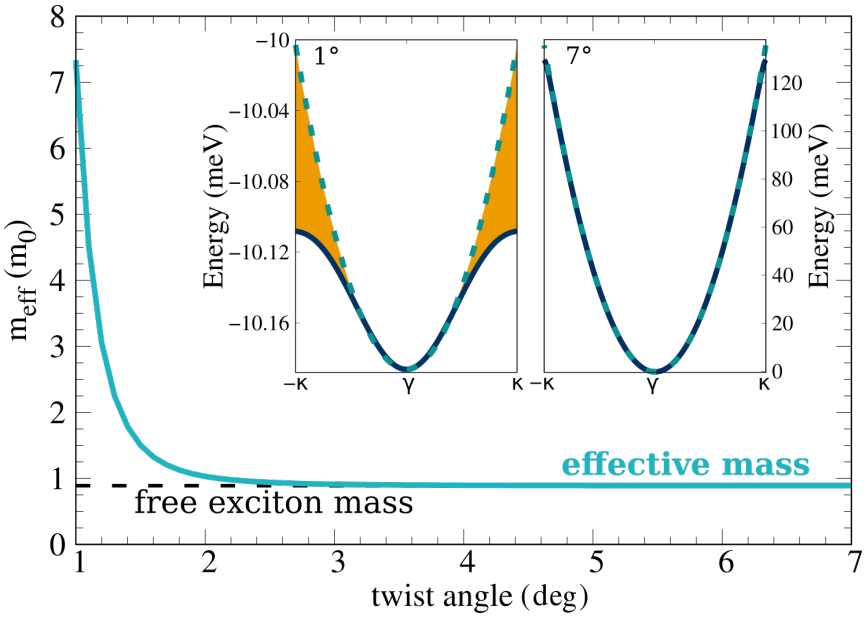

Figure 7.6: Effective exciton mass as a function of the twist angle ϑ. For larger angles, we find that the effective mass corresponds to the free exciton mass. The insets illustrate that the parabolic approximation (dashed line) fails for small twist angles (here 1°), while it is a perfect assumption at larger angles (here 7°).

7.6 Polaron Impact on Spatio-Temporal Dynamics

In the preceding Chapter 6, we delved into the exciton-phonon interaction, illustrating its profound impact on the energy landscape. Notably, we demonstrated that polarons play a pivotal role in modulating the bandwidth, with this influence being markedly temperature-dependent. Consequently, as explored in Section 7.2.2, we observed significant deviations in the hopping rates from the phonon-free excitonic case, particularly as the temperature increased. While we anticipate these effects to extend to transport properties, the extent of this influence remains uncertain. In this section, we embark on an exploration of the polaronic impact on spatiotemporal dynamics, aiming to unravel the intricacies of this influence.

Figure 7.7(a) visually illustrates the spatial evolution of exciton density at fixed times, specifically at a twist angle of $\theta = 2°$ and room temperature. Commencing with an initial Gaussian distribution at $t = 0$ ps, we track the propagation of excitons

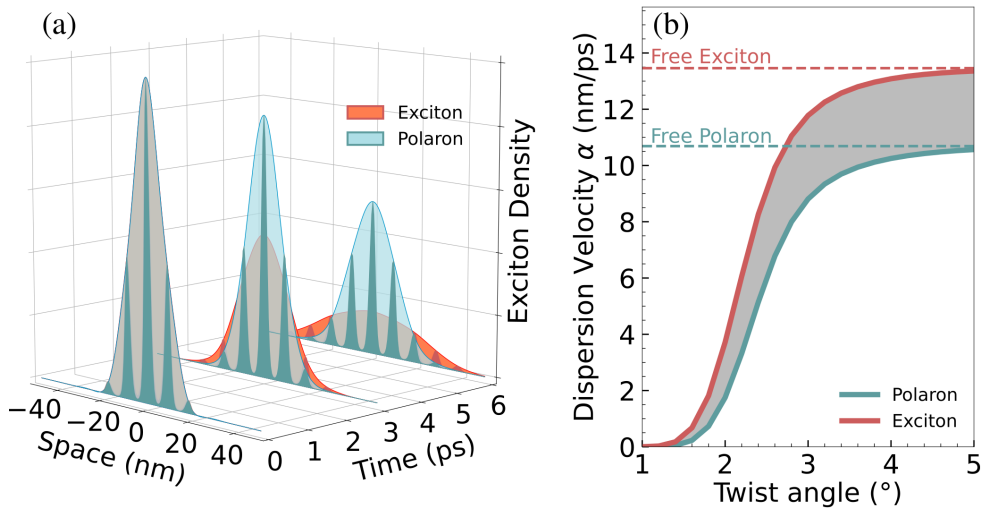

Figure 7.7: a) Spatial evolution of exciton density at 2° (shaded area) for exciton and polaron cases at fixed times. Notably, polarons exhibit a distinctly decelerated spatial propagation. (b) Dispersion parameter α (Eq.(7.7)) plotted against twist angle, facilitating a direct comparison between undisturbed exciton and polaron cases. Both converge to the free exciton/polaron case at larger twist angles, where the moiré potential becomes negligible.

in space. The localized peaks (darker shading) signify localized states at the given angle. To enhance clarity in comparing the propagation behavior, we introduce an envelope function and normalize the initial distributions of excitons with and without polarons to be identical (represented by red and blue shading). At $t = 3$ps and more prominently at $t = 6$ps, a distinct difference in propagation speed between free excitons and polarons is observed (cf. Fig 7.7(a)). This observation aligns with our earlier findings, indicating that polarons contribute to a slower exciton propagation. This deceleration is attributed to the increased effective mass of excitons due to polarons, resulting in reduced hopping rates and diminished mobility.

For a quantitative analysis of moiré exciton propagation, we employ the dispersion velocity parameter α from Eq.(7.7). The analysis reveals a clear trend: as the twist angle increases, both excitons and polarons converge toward their respective free excitonic/polaron solutions (Fig. 7.7(b)). Beyond a critical angle of approximately $\theta = 3°$, the dispersion parameter α saturates, indicating a constant dispersion characteristic for free excitons/polarons. Exciton propagation within a moiré potential characterized by a large twist angle mirrors the dispersion behavior of a quantum-

mechanical wave packet. Put differently, the observed motion, akin to free particle motion, persists even in the presence of polarons, as detailed in Section 7.5. In contrast, for small twist angles, exciton propagation becomes severely limited due to band flattening in the exciton dispersion. This twist-angle effect is accentuated by the formation of polarons, which lead to an increase in mass and consequently a flattening of the band. This band flattening hinders the convergence processes observed in the unperturbed case, where excitons are delocalized. As a result, the polaronic dispersion velocity is lower than in the purely excitonic case. Furthermore, a delay in the velocity increase is evident (indicated by the grey area in Fig 7.7 (b)). The relative difference in dispersion velocity between free excitons and polarons at large twist angles is estimated to be around 53%.

8

Conclusion

This thesis delves deeply into the microscopic intricacies of exciton dynamics within a heterostructure systems: twisted van der Waals structures and moiré configurations in $MoSe_2/WSe_2$. The investigation explores the nuanced interplay of factors influencing exciton transport, unraveling novel phenomena and contributing significantly to the broader field of condensed matter physics.

After introducing fundamental concepts, which covered essential components such as the non-interacting electron model, Coulomb matrix elements, and the exciton picture—with emphasis on concepts like the electron-hole pair operator and basis transformations—we delved into key aspects of heterostructure analysis. This included a comprehensive redefinition of the Coulomb potential in bilayers and an exploration of Moiré physics, encompassing zone folding and an investigation into the development and influence of the interlayer Moiré potential.

We focused in the thesis on two specific case studies. First, the study investigates spatio-temporal exciton dynamics in twisted van der Waals heterostructures. Distinct transport regimes emerge based on twist angles: at large angles ($\vartheta > 4°$), excitons propagate akin to wave packets in a dispersion regime, while at smaller angles, the hopping regime prevails ($\vartheta < 2°$) with exciton motion accurately described by a tunneling model. The study unveils the twist-angle dependence of exciton propagation, providing invaluable microscopic insights.

In the second case study, the thesis explores the influence of polaron-induced exciton mass enhancement on moiré exciton transport in a twisted $MoSe_2/WSe_2$ heterostructure. The presence of polarons leads to a distinct flattening of moiré exciton bands and a significant reduction in bandwidth. At small twist angles, the predicted changes in energy bandwidth exceed 60%, and hopping rates are substantially diminished by up to 80% due to weakened wavefunction overlap. Despite generally improved exciton mobility at higher twist angles, the counteracting effects of polarons impede exciton motion in TMD heterostructures.

Collectively, these studies enrich our understanding of exciton dynamics in diverse heterostructure scenarios. The research work forms the basis for the development of materials with customized exciton properties and may pave the way for applications in optoelectronics and quantum technology. The knowledge gained in this work serves as a catalyst for future studies and advances in the manipulation and control of exciton transport in complex condensed matter systems. A potential next step involves considering exciton-exciton interactions, as explored in earlier studies [107, 108]. A subsequent investigation could focus on discerning the impact of these interactions on exciton dynamics. Recent research indicates that with an increasing exciton density, previously trapped moiré excitons become delocalized [109]. Within our framework, it would be valuable to determine whether polaron formation counteracts this effect or represents the dominant contribution.

Another possible next step involves exploring local strain modulation, a method effectively used to create potential traps and localize intralayer excitons in TMD monolayers [110, 111]. Previous research has delved into the impact of strains on indirect excitons in TMD heterostructures, revealing evidence for the formation of potential traps and the trapping of interlayer excitons within these heterostructures [112]. Investigating whether this behavior is reproducible within our theoretical framework would be of particular interest. As it could potentially open up new avenues for applications in photonic and optoelectronic devices.

Finally, a third intriguing subsequent study could involve incorporating an external electric field. Existing literature indicates that such a field can induce significant changes in the electronic band structure [113]. In this thesis, our focus is on a specific material, $MoSe_2/WSe_2$, and relevant studies for this material reveal that an applied external electric field profoundly affects the electronic landscape [114]. Examining the influence of such a field on spatio-temporal exciton dynamics could deepen our fundamental understanding and potentially contribute to advancements in electronic devices.

Zusammenfassung

Diese Dissertation taucht tief in die mikroskopischen Feinheiten der Exzitondynamik in Heterostruktursystemen ein: verdrehte van-der-Waals-Strukturen und Moiré Konfigurationen in $MoSe_2/WSe_2$. Die Untersuchung erkundet das nuancierte Zusammenspiel von Faktoren, die den Exzitonen-Transport beeinflussen, deckt neue Phänomene auf und trägt wesentlich zur Festkörperphysik bei.
Nach der Einführung grundlegender Konzepte, die wesentliche Komponenten wie das Modell der nicht wechselwirkenden Elektronen, Coulomb-Matrixelemente und das Exziton-Bild einschließen – wobei besonderes Augenmerk auf Konzepten wie dem Elektron-Loch-Paar-Operator und Basis-Transformationen liegt – vertieften wir uns in Schlüsselaspekte der Heterostrukturanalyse. Dies umfasste eine umfassende Neudefinition des Coulomb-Potentials in Doppelschichten und eine Untersuchung der Moiré-Physik, die Zone-Folding einschloss und die Entwicklung und den Einfluss des Moiré-Potentials zwischen den Schichten untersuchte.
In der Dissertation konzentrieren wir uns auf zwei spezifische Fallstudien. Zunächst untersucht die Studie die räumlich-zeitliche Exzitondynamik in verdrehten van-der-Waals-Heterostrukturen. Unterschiedliche Transportregime entstehen auf der Grundlage von Verdrehungswinkeln: Bei großen Winkeln ($\vartheta > 4°$) breiten sich Exzitonen ähnlich wie Wellenpakete in einem Dispersionsregime aus, während bei kleineren Winkeln das Hopping-Regime überwiegt ($\vartheta < 2°$) und die Exziton-Bewegung genau durch ein Tunnelmodell beschrieben wird. Die Studie enthüllt die Verdrehungswinkel-Abhängigkeit der Exziton-Propagation und liefert unschätzbar wertvolle mikroskopische Einblicke. In der zweiten Fallstudie untersucht die Dissertation den Einfluss der durch Polaronen verursachten Verstärkung der Exzitonmasse auf den Exzitontransport in einer verdrehten $MoSe_2/WSe_2$-Heterostruktur. Die Anwesenheit von Polaronen führt zu einer deutlichen Abflachung der Moiré-Exziton-Bänder und einer erheblichen Reduzierung der Bandbreite. Bei kleinen Verdrehungswinkeln übertreffen die vorhergesagten Änderungen der Energiebandbreite 60%, und die Hoppungsraten sind aufgrund einer geschwächten Überlappung der Wellenfunktionen erheblich reduziert. Trotz allgemein verbesserter Exzitonmobilität bei höheren Verdrehungswinkeln be-

hindern die gegenläufigen Effekte von Polaronen die Exzitonbewegung in TMD-Heterostrukturen.
Zusammenfassend bereichern diese Studien unser Verständnis der Exzitondynamik in verschiedenen Heterostrukturszenarien. Die Forschung bildet die Grundlage für die Entwicklung von Materialien mit maßgeschneiderten Exzitoneigenschaften und könnte den Weg für Anwendungen in der Optoelektronik und Quantentechnologie ebnen. Das in dieser Arbeit gewonnene Wissen dient als Ausgangspunkt für zukünftige Studien und Fortschritte bei der Manipulation und Kontrolle des Exzitontransports in komplexen kondensierten Materiesystemen. Ein möglicher nächster Schritt könnte die Berücksichtigung von Exziton-Exziton-Wechselwirkungen sein, wie sie in früheren Studien untersucht wurden [107, 108]. Eine anschließende Untersuchung könnte sich darauf konzentrieren, die Auswirkungen dieser Wechselwirkungen auf die Exzitondynamik zu klären. Aktuelle Forschung zeigt, dass mit zunehmender Exzitondichte zuvor gefangene Moiré-Exzitonen delokalisiert werden [109]. In unserem Rahmen wäre es wertvoll zu bestimmen, ob die Bildung von Polaronen diesem Effekt entgegenwirkt oder den dominanten Beitrag darstellt. Ein weiterer möglicher nächster Schritt bezieht sich auf die lokale Dehnungsmodulation, die als effektive Methode zur Erzeugung von Potenzialfallen und zur Lokalisierung von intralayer Exzitonen in TMD-Monolagen genutzt wurde [110, 111]. Frühere Forschungen haben die Auswirkungen von Spannungen auf indirekte Exzitonen in TMD-Heterostrukturen untersucht, wobei Anzeichen für die Bildung von Potenzialfallen und die Einschließung von Interlayer-Exzitonen vorliegen [112]. Die Untersuchung, ob dieses Verhalten in unserem theoretischen Model reproduzierbar ist, wäre von besonderem Interesse. Da es potenziell neue Anwendungsmöglichkeiten in photonischen und optoelektronischen Geräten eröffnen könnte. Schließlich könnte eine dritte interessante Folgestudie die Integration eines externen elektrischen Feldes beinhalten. Die vorhandene Literatur deutet darauf hin, dass ein solches Feld signifikante Veränderungen in der elektronischen Bandstruktur induzieren kann [113]. In dieser Arbeit konzentrieren wir uns auf ein spezifisches Material, $MoSe_2/WSe_2$, und relevante Studien für dieses Material zeigen, dass ein angelegtes externes elektrisches Feld einen tiefgreifenden Einfluss auf die elektronische Landschaft hat [114]. Die Untersuchung des Einflusses eines solchen Feldes auf die räumlich-zeitliche Exzitondynamik könnte unser grundlegendes Verständnis vertiefen und möglicherweise zu Fortschritten in elektronischen Geräten beitragen.

Bibliography

[1] Kin Fai Mak, Changgu Lee, James Hone, Jie Shan, and Tony F Heinz. Atomically thin mos 2: a new direct-gap semiconductor. *Physical review letters*, 105(13):136805, 2010.

[2] Kostya S Novoselov, Andre K Geim, Sergei V Morozov, De-eng Jiang, Yanshui Zhang, Sergey V Dubonos, Irina V Grigorieva, and Alexandr A Firsov. Electric field effect in atomically thin carbon films. *science*, 306(5696):666–669, 2004.

[3] Qing Hua Wang, Kourosh Kalantar-Zadeh, Andras Kis, Jonathan N Coleman, and Michael S Strano. Electronics and optoelectronics of two-dimensional transition metal dichalcogenides. *Nature nanotechnology*, 7(11):699–712, 2012.

[4] Gang Wang, Alexey Chernikov, Mikhail M Glazov, Tony F Heinz, Xavier Marie, Thierry Amand, and Bernhard Urbaszek. Colloquium: Excitons in atomically thin transition metal dichalcogenides. *Reviews of Modern Physics*, 90(2):021001, 2018.

[5] Thomas Mueller and Ermin Malic. Exciton physics and device application of two-dimensional transition metal dichalcogenide semiconductors. *npj 2D Materials and Applications*, 2(1):1–12, 2018.

[6] Raul Perea-Causin, Daniel Erkensten, Jamie M Fitzgerald, Joshua JP Thompson, Roberto Rosati, Samuel Brem, and Ermin Malic. Exciton optics, dynamics, and transport in atomically thin semiconductors. *APL Materials*, 10(10), 2022.

[7] Roberto Rosati, Frank Lengers, Christian Carmesin, Matthias Florian, Tilmann Kuhn, Frank Jahnke, Michael Lorke, and Doris E Reiter. Electron dynamics in a two-dimensional nanobubble: A two-level system based on spatial density. *Nano Letters*, 21(23):9896–9902, 2021.

[8] Iris Niehues, Robert Schmidt, Matthias Druppel, Philipp Marauhn, Dominik Christiansen, Malte Selig, Gunnar Berghäuser, Daniel Wigger, Robert Schneider, Lisa Braasch, et al. Strain control of exciton–phonon coupling in atomically thin semiconductors. *Nano letters*, 18(3):1751–1757, 2018.

[9] Ozgur Burak Aslan, Minda Deng, and Tony F Heinz. Strain tuning of excitons in monolayer wse 2. *Physical Review B*, 98(11):115308, 2018.

[10] Simone Latini, Thomas Olsen, and Kristian Sommer Thygesen. Excitons in van der waals heterostructures: The important role of dielectric screening. *Physical Review B*, 92(24):245123, 2015.

[11] Roberto Rosati, Robert Schmidt, Samuel Brem, Raül Perea-Causín, Iris Niehues, Johannes Kern, Johann A Preuß, Robert Schneider, Steffen Michaelis de Vasconcellos, Rudolf Bratschitsch, et al. Dark exciton anti-funneling in atomically thin semiconductors. *Nature Communications*, 12(1):1–7, 2021.

[12] Zahra Khatibi, Maja Feierabend, Malte Selig, Samuel Brem, Christopher Linderälv, Paul Erhart, and Ermin Malic. Impact of strain on the excitonic linewidth in transition metal dichalcogenides. *2D Materials*, 6(1):015015, 2018.

[13] Maja Feierabend, Alexandre Morlet, Gunnar Berghäuser, and Ermin Malic. Impact of strain on the optical fingerprint of monolayer transition-metal dichalcogenides. *Physical Review B*, 96(4):045425, 2017.

[14] Marvin Kulig, Jonas Zipfel, Philipp Nagler, Sofia Blanter, Christian Schüller, Tobias Korn, Nicola Paradiso, Mikhail M Glazov, and Alexey Chernikov. Exciton diffusion and halo effects in monolayer semiconductors. *Physical review letters*, 120(20):207401, 2018.

[15] Raul Perea-Causin, Samuel Brem, Roberto Rosati, Roland Jago, Marvin Kulig, Jonas D Ziegler, Jonas Zipfel, Alexey Chernikov, and Ermin Malic. Exciton propagation and halo formation in two-dimensional materials. *Nano letters*, 19(10):7317–7323, 2019.

[16] Koloman Wagner, Jonas Zipfel, Roberto Rosati, Edith Wietek, Jonas D Ziegler, Samuel Brem, Raül Perea-Causín, Takashi Taniguchi, Kenji Watan-

abe, Mikhail M Glazov, et al. Nonclassical exciton diffusion in monolayer wse 2. *Physical Review Letters*, 127(7):076801, 2021.

[17] Roberto Rosati, Raül Perea-Causín, Samuel Brem, and Ermin Malic. Negative effective excitonic diffusion in monolayer transition metal dichalcogenides. *Nanoscale*, 12(1):356–363, 2020.

[18] Anton Matthijs Berghuis, TV Raziman, Alexei Halpin, Shaojun Wang, Alberto G Curto, and Jaime Gómez Rivas. Effective negative diffusion of singlet excitons in organic semiconductors. *The journal of physical chemistry letters*, 12(4):1360–1366, 2021.

[19] Edith Wietek, Matthias Florian, Jonas M Göser, Takashi Taniguchi, Kenji Watanabe, Alexander Högele, Mikhail M Glazov, Alexander Steinhoff, and Alexey Chernikov. Non-linear and negative effective diffusivity of optical excitations in moir\'e-free heterobilayers. *arXiv preprint arXiv:2306.12339*, 2023.

[20] Fedele Tagarelli, Edoardo Lopriore, Daniel Erkensten, Raül Perea-Causín, Samuel Brem, Joakim Hagel, Zhe Sun, Gabriele Pasquale, Kenji Watanabe, Takashi Taniguchi, et al. Electrical control of hybrid exciton transport in a van der waals heterostructure. *Nature Photonics*, pages 1–7, 2023.

[21] Hongyi Yu, Gui-Bin Liu, Jianju Tang, Xiaodong Xu, and Wang Yao. Moiré excitons: From programmable quantum emitter arrays to spin-orbit–coupled artificial lattices. *Science advances*, 3(11):e1701696, 2017.

[22] Philipp Merkl, Fabian Mooshammer, Philipp Steinleitner, Anna Girnghuber, K-Q Lin, Philipp Nagler, Johannes Holler, Christian Schüller, John M Lupton, Tobias Korn, et al. Ultrafast transition between exciton phases in van der waals heterostructures. *Nature materials*, 18(7):691–696, 2019.

[23] Samuel Brem, Christopher Linderälv, Paul Erhart, and Ermin Malic. Tunable phases of moiré excitons in van der waals heterostructures. *Nano letters*, 20(12):8534–8540, 2020.

[24] Sara Shabani, Dorri Halbertal, Wenjing Wu, Mingxing Chen, Song Liu, James Hone, Wang Yao, Dmitri N Basov, Xiaoyang Zhu, and Abhay N Pasupathy. Deep moiré potentials in twisted transition metal dichalcogenide bilayers. *Nature Physics*, 17(6):720–725, 2021.

[25] Philipp Merkl, Fabian Mooshammer, Samuel Brem, Anna Girnghuber, Kai-Qiang Lin, Leonard Weigl, Marlene Liebich, Chaw-Keong Yong, Roland Gillen, Janina Maultzsch, et al. Twist-tailoring coulomb correlations in van der waals homobilayers. *Nature communications*, 11(1):1–7, 2020.

[26] David Schmitt, Jan Philipp Bange, Wiebke Bennecke, AbdulAziz AlMutairi, Giuseppe Meneghini, Kenji Watanabe, Takashi Taniguchi, Daniel Steil, D Russell Luke, R Thomas Weitz, et al. Formation of moiré interlayer excitons in space and time. *Nature*, 608(7923):499–503, 2022.

[27] Giuseppe Meneghini, Samuel Brem, and Ermin Malic. Ultrafast phonon-driven charge transfer in van der waals heterostructures. *Natural Sciences*, 2(4):e20220014, 2022.

[28] Hyeonjun Baek, Mauro Brotons-Gisbert, Zhe Xian Koong, Aidan Campbell, Markus Rambach, Kenji Watanabe, Takashi Taniguchi, and Brian D Gerardot. Highly energy-tunable quantum light from moiré-trapped excitons. *Science advances*, 6(37):eaba8526, 2020.

[29] Kyle L Seyler, Pasqual Rivera, Hongyi Yu, Nathan P Wilson, Essance L Ray, David G Mandrus, Jiaqiang Yan, Wang Yao, and Xiaodong Xu. Signatures of moiré-trapped valley excitons in mose2/wse2 heterobilayers. *Nature*, 567(7746):66–70, 2019.

[30] Willy Knorr, Samuel Brem, Giuseppe Meneghini, and Ermin Malic. Exciton transport in a moiré potential: From hopping to dispersive regime. *Physical Review Materials*, 6(12):124002, 2022.

[31] Zidong Li, Xiaobo Lu, Darwin F Cordovilla Leon, Zhengyang Lyu, Hongchao Xie, Jize Hou, Yanzhao Lu, Xiaoyu Guo, Austin Kaczmarek, Takashi Taniguchi, et al. Interlayer exciton transport in mose2/wse2 heterostructures. *ACS nano*, 15(1):1539–1547, 2021.

[32] Malte Selig, Gunnar Berghäuser, Archana Raja, Philipp Nagler, Christian Schüller, Tony F Heinz, Tobias Korn, Alexey Chernikov, Ermin Malic, and Andreas Knorr. Excitonic linewidth and coherence lifetime in monolayer transition metal dichalcogenides. *Nature communications*, 7(1):1–6, 2016.

[33] Samuel Brem, August Ekman, Dominik Christiansen, Florian Katsch, Malte Selig, Cedric Robert, Xavier Marie, Bernhard Urbaszek, Andreas Knorr, and Ermin Malic. Phonon-assisted photoluminescence from indirect excitons in monolayers of transition-metal dichalcogenides. *Nano letters*, 20(4):2849–2856, 2020.

[34] Samuel Brem, Malte Selig, Gunnar Berghäuser, and Ermin Malic. Exciton relaxation cascade in two-dimensional transition metal dichalcogenides. *Scientific reports*, 8(1):8238, 2018.

[35] Giacomo Mazza and Adriano Amaricci. Strongly correlated exciton-polarons in twisted homobilayer heterostructures. *Physical Review B*, 106(24):L241104, 2022.

[36] Tsung-Sheng Huang, Yang-Zhi Chou, Christopher L Baldwin, Fengcheng Wu, and Mohammad Hafezi. Mott-moiré excitons. *Physical Review B*, 107(19):195151, 2023.

[37] Aidan J Campbell, Mauro Brotons-Gisbert, Hyeonjun Baek, Valerio Vitale, Takashi Taniguchi, Kenji Watanabe, Johannes Lischner, and Brian D Gerardot. Exciton-polarons in the presence of strongly correlated electronic states in a mose2/wse2 moiré superlattice. *npj 2D Materials and Applications*, 6(1):79, 2022.

[38] Alexander Sergeevich Alexandrov and Aleksandr Borisovich Krebs. Polarons in high-temperature superconductors. *Soviet Physics Uspekhi*, 35(5):345, 1992.

[39] A Mauger. Magnetic polaron: Theory and experiment. *Physical Review B*, 27(4):2308, 1983.

[40] Fang Qin, Xiaoling Cui, Wei Yi, et al. Polaron in a p+ i p fermi topological superfluid. *Physical Review A*, 99(3):033613, 2019.

[41] Koen Vandewal, Johannes Benduhn, Karl Sebastian Schellhammer, Tim Vangerven, Janna E Rückert, Fortunato Piersimoni, Reinhard Scholz, Olaf Zeika, Yeli Fan, Stephen Barlow, et al. Absorption tails of donor: C60 blends provide insight into thermally activated charge-transfer processes and polaron relaxation. *Journal of the American Chemical Society*, 139(4):1699–1704, 2017.

[42] G Van Der Laan. Polaronic satellites in x-ray-absorption spectra. *Physical Review B*, 41(17):12366, 1990.

[43] Anders A Johansson and Sven Stafström. Nonadiabatic simulations of polaron dynamics. *Physical Review B*, 69(23):235205, 2004.

[44] Gerd Czycholl. *Theoretische Festkörperphysik Band 1: Grundlagen: Phononen und Elektronen in Kristallen*. Springer-Verlag, 2015.

[45] Wolfgang Nolting. *Grundkurs theoretische physik 7: viel-teilchen-theorie (springer-lehrbuch)(german edition)*. Springer Spektrum, 2015.

[46] Pierluigi Cudazzo, Ilya V Tokatly, and Angel Rubio. Dielectric screening in two-dimensional insulators: Implications for excitonic and impurity states in graphane. *Physical Review B*, 84(8):085406, 2011.

[47] Alexey Chernikov, Timothy C Berkelbach, Heather M Hill, Albert Rigosi, Yilei Li, Burak Aslan, David R Reichman, Mark S Hybertsen, and Tony F Heinz. Exciton binding energy and nonhydrogenic rydberg series in monolayer ws 2. *Physical review letters*, 113(7):076802, 2014.

[48] Natalia S Rytova. Screened potential of a point charge in a thin film. *arXiv preprint arXiv:1806.00976*, 2018.

[49] LV Keldysh. Coulomb interaction in thin semiconductor and semimetal films. *Soviet Journal of Experimental and Theoretical Physics Letters*, 29:658, 1979.

[50] Akash Laturia, Maarten L Van de Put, and William G Vandenberghe. Dielectric properties of hexagonal boron nitride and transition metal dichalcogenides: from monolayer to bulk. *npj 2D Materials and Applications*, 2(1):6, 2018.

[51] Zhenghe Jin, Xiaodong Li, Jeffrey T Mullen, and Ki Wook Kim. Intrinsic transport properties of electrons and holes in monolayer transition-metal dichalcogenides. *Physical Review B*, 90(4):045422, 2014.

[52] Kristen Kaasbjerg, Kristian S Thygesen, and Antti-Pekka Jauho. Acoustic phonon limited mobility in two-dimensional semiconductors: Deformation potential and piezoelectric scattering in monolayer mos 2 from first principles. *Physical Review B*, 87(23):235312, 2013.

[53] J Bardeen and WJPR Shockley. Deformation potentials and mobilities in non-polar crystals. *Physical review*, 80(1):72, 1950.

[54] Hartwin Peelaers and Chris G Van de Walle. Effects of strain on band structure and effective masses in mos 2. *Physical Review B*, 86(24):241401, 2012.

[55] Fengcheng Wu, Timothy Lovorn, and Allan H MacDonald. Topological exciton bands in moiré heterojunctions. *Physical review letters*, 118(14):147401, 2017.

[56] Fengcheng Wu, Fanyao Qu, and Allan H MacDonald. Exciton band structure of monolayer mos 2. *Physical Review B*, 91(7):075310, 2015.

[57] Samuel Brem, Kai-Qiang Lin, Roland Gillen, Jonas M Bauer, Janina Maultzsch, John M Lupton, and Ermin Malic. Hybridized intervalley moiré excitons and flat bands in twisted wse 2 bilayers. *Nanoscale*, 12(20):11088–11094, 2020.

[58] Xiao-Xiao Zhang, Yumeng You, Shu Yang Frank Zhao, and Tony F Heinz. Experimental evidence for dark excitons in monolayer wse 2. *Physical review letters*, 115(25):257403, 2015.

[59] Thorsten Deilmann and Kristian Sommer Thygesen. Finite-momentum exciton landscape in mono-and bilayer transition metal dichalcogenides. *2D Materials*, 6(3):035003, 2019.

[60] Joakim Hagel, Samuel Brem, Christopher Linderälv, Paul Erhart, and Ermin Malic. Exciton landscape in van der waals heterostructures. *Physical Review Research*, 3(4):043217, 2021.

[61] Roland Gillen and Janina Maultzsch. Interlayer excitons in mose 2/wse 2 heterostructures from first principles. *Physical Review B*, 97(16):165306, 2018.

[62] Xiaobo Lu, Xiaoqin Li, and Li Yang. Modulated interlayer exciton properties in a two-dimensional moiré crystal. *Physical Review B*, 100(15):155416, 2019.

[63] Yuan Cao, Valla Fatemi, Shiang Fang, Kenji Watanabe, Takashi Taniguchi, Efthimios Kaxiras, and Pablo Jarillo-Herrero. Unconventional superconductivity in magic-angle graphene superlattices. *Nature*, 556(7699):43–50, 2018.

[64] Yuan Cao, Valla Fatemi, Ahmet Demir, Shiang Fang, Spencer L Tomarken, Jason Y Luo, Javier D Sanchez-Yamagishi, Kenji Watanabe, Takashi Taniguchi, Efthimios Kaxiras, et al. Correlated insulator behaviour at half-filling in magic-angle graphene superlattices. *Nature*, 556(7699):80–84, 2018.

[65] Y Cao, JY Luo, V Fatemi, S Fang, JD Sanchez-Yamagishi, K Watanabe, T Taniguchi, E Kaxiras, and Pablo Jarillo-Herrero. Superlattice-induced insulating states and valley-protected orbits in twisted bilayer graphene. *Physical review letters*, 117(11):116804, 2016.

[66] Aviram Uri, Sameer Grover, Yuan Cao, John A Crosse, Kousik Bagani, Daniel Rodan-Legrain, Yuri Myasoedov, Kenji Watanabe, Takashi Taniguchi, Pilkyung Moon, et al. Mapping the twist-angle disorder and landau levels in magic-angle graphene. *Nature*, 581(7806):47–52, 2020.

[67] H Wang and K Kalantar-Zadeh. Hybrid nanomaterials of sns/carbon nanostructures for supercapacitor applications. *Nanotechnology*, 7:699–712, 2012.

[68] Hao Chen, Jinde Yin, Jingwei Yang, Xuejun Zhang, Mengli Liu, Zike Jiang, Jinzhang Wang, Zhipei Sun, Tuan Guo, Wenjun Liu, et al. Transition-metal dichalcogenides heterostructure saturable absorbers for ultrafast photonics. *Optics letters*, 42(21):4279–4282, 2017.

[69] Jingwen Zhou, Jian Qin, Lichao Guo, Naiqin Zhao, Chunsheng Shi, En-zuo Liu, Fang He, Liying Ma, Jiajun Li, and Chunnian He. Scalable synthesis of high-quality transition metal dichalcogenide nanosheets and their application as sodium-ion battery anodes. *Journal of Materials Chemistry A*, 4(44):17370–17380, 2016.

[70] Eunjeong Yang, Hyunjun Ji, and Yousung Jung. Two-dimensional transition metal dichalcogenide monolayers as promising sodium ion battery anodes. *The Journal of Physical Chemistry C*, 119(47):26374–26380, 2015.

[71] Kenan Zhang, Tianning Zhang, Guanghui Cheng, Tianxin Li, Shuxia Wang, Wei Wei, Xiaohao Zhou, Weiwei Yu, Yan Sun, Peng Wang, et al. Interlayer transition and infrared photodetection in atomically thin type-ii mote2/mos2 van der waals heterostructures. *ACS nano*, 10(3):3852–3858, 2016.

[72] Haijie Tan, Wenshuo Xu, Yuewen Sheng, Chit Siong Lau, Ye Fan, Qu Chen, Martin Tweedie, Xiaochen Wang, Yingqiu Zhou, and Jamie H Warner. Lateral graphene-contacted vertically stacked ws2/mos2 hybrid photodetectors with large gain. *Advanced Materials*, 29(46):1702917, 2017.

[73] Toshiki Akama, Wakana Okita, Reito Nagai, Chao Li, Toshiro Kaneko, and Toshiaki Kato. Schottky solar cell using few-layered transition metal dichalcogenides toward large-scale fabrication of semitransparent and flexible power generator. *Scientific reports*, 7(1):11967, 2017.

[74] A Thilagam. Transition-metal dichalcogenide heterostructure solar cells: a numerical study. *Journal of Mathematical Chemistry*, 55:50–64, 2017.

[75] Xinyi Chia and Martin Pumera. Characteristics and performance of two-dimensional materials for electrocatalysis. *Nature Catalysis*, 1(12):909–921, 2018.

[76] Jianping Shi, Rui Tong, Xiebo Zhou, Yue Gong, Zhepeng Zhang, Qingqing Ji, Yu Zhang, Qiyi Fang, Lin Gu, Xina Wang, et al. Temperature-mediated selective growth of mos2/ws2 and ws2/mos2 vertical stacks on au foils for direct photocatalytic applications. *Advanced Materials*, 28(48):10664–10672, 2016.

[77] X Tong, Y Qi, J Chen, N Wang, and Q Xu. Chemnanomat 2017, 3, 466–471. *Ren, Q. Xu, C. Wang, X. Zheng, Y. Jia, Y. Qi, Y. Zhou, X. Yang, Z. Zhang, ChemNanoMat*, 3:632–638, 2017.

[78] Shixuan Wang, Xuehao Cui, Chang'e Jian, Haowei Cheng, Mengmeng Niu, Jia Yu, Jiaxu Yan, and Wei Huang. Stacking-engineered heterostructures in transition metal dichalcogenides. *Advanced Materials*, 33(16):2005735, 2021.

[79] Thomas Heine. Transition metal chalcogenides: ultrathin inorganic materials with tunable electronic properties. *Accounts of chemical research*, 48(1):65–72, 2015.

[80] Jiangang He, Kerstin Hummer, and Cesare Franchini. Stacking effects on the electronic and optical properties of bilayer transition metal dichalcogenides mos 2, mose 2, ws 2, and wse 2. *Physical Review B*, 89(7):075409, 2014.

[81] Jun Kang, Sefaattin Tongay, Jian Zhou, Jingbo Li, and Junqiao Wu. Band offsets and heterostructures of two-dimensional semiconductors. *Applied Physics Letters*, 102(1), 2013.

[82] Hoseok Heo, Ji Ho Sung, Soonyoung Cha, Bo-Gyu Jang, Joo-Youn Kim, Gangtae Jin, Donghun Lee, Ji-Hoon Ahn, Myoung-Jae Lee, Ji Hoon Shim, et al. Interlayer orientation-dependent light absorption and emission in monolayer semiconductor stacks. *Nature communications*, 6(1):7372, 2015.

[83] Yingqiu Zhou, Wenshuo Xu, Yuewen Sheng, Hefu Huang, Qianyang Zhang, Linlin Hou, Viktoryia Shautsova, and Jamie H Warner. Symmetry-controlled reversible photovoltaic current flow in ultrathin all 2d vertically stacked graphene/mos2/ws2/graphene devices. *ACS applied materials & interfaces*, 11(2):2234–2242, 2019.

[84] David A Ruiz-Tijerina and Vladimir I Fal'ko. Interlayer hybridization and moiré superlattice minibands for electrons and excitons in heterobilayers of transition-metal dichalcogenides. *Physical Review B*, 99(12):125424, 2019.

[85] Hongyi Yu, Gui-Bin Liu, and Wang Yao. Brightened spin-triplet interlayer excitons and optical selection rules in van der waals heterobilayers. *2D Materials*, 5(3):035021, 2018.

[86] Tomasz Woźniak, Paulo E Faria Junior, Gotthard Seifert, Andrey Chaves, and Jens Kunstmann. Exciton g factors of van der waals heterostructures from first-principles calculations. *Physical Review B*, 101(23):235408, 2020.

[87] Simon Ovesen, Samuel Brem, Christopher Linderälv, Mikael Kuisma, Tobias Korn, Paul Erhart, Malte Selig, and Ermin Malic. Interlayer exciton dynamics in van der waals heterostructures. *Communications Physics*, 2(1):23, 2019.

[88] John R Schaibley, Hongyi Yu, Genevieve Clark, Pasqual Rivera, Jason S Ross, Kyle L Seyler, Wang Yao, and Xiaodong Xu. Valleytronics in 2d materials. *Nature Reviews Materials*, 1(11):1–15, 2016.

[89] Samuel Brem and Ermin Malic. Terahertz fingerprint of monolayer wigner crystals. *Nano letters*, 22(3):1311–1315, 2022.

[90] Eva Y Andrei, Dmitri K Efetov, Pablo Jarillo-Herrero, Allan H MacDonald, Kin Fai Mak, T Senthil, Emanuel Tutuc, Ali Yazdani, and Andrea F Young. The marvels of moiré materials. *Nature Reviews Materials*, 6(3):201–206, 2021.

[91] Kha Tran, Galan Moody, Fengcheng Wu, Xiaobo Lu, Junho Choi, Kyounghwan Kim, Amritesh Rai, Daniel A Sanchez, Jiamin Quan, Akshay Singh, et al. Evidence for moiré excitons in van der waals heterostructures. *Nature*, 567(7746):71–75, 2019.

[92] Chenhao Jin, Emma C Regan, Aiming Yan, M Iqbal Bakti Utama, Danqing Wang, Sihan Zhao, Ying Qin, Sijie Yang, Zhiren Zheng, Shenyang Shi, et al. Observation of moiré excitons in wse2/ws2 heterostructure superlattices. *Nature*, 567(7746):76–80, 2019.

[93] Evgeny M Alexeev, David A Ruiz-Tijerina, Mark Danovich, Matthew J Hamer, Daniel J Terry, Pramoda K Nayak, Seongjoon Ahn, Sangyeon Pak, Juwon Lee, Jung Inn Sohn, et al. Resonantly hybridized excitons in moiré superlattices in van der waals heterostructures. *Nature*, 567(7746):81–86, 2019.

[94] Michael Förg, Anvar S Baimuratov, Stanislav Yu Kruchinin, Ilia A Vovk, Johannes Scherzer, Jonathan Förste, Victor Funk, Kenji Watanabe, Takashi Taniguchi, and Alexander Högele. Moiré excitons in mose2-wse2 heterobilayers and heterotrilayers. *Nature communications*, 12(1):1–7, 2021.

[95] Willy Knorr, Samuel Brem, Giuseppe Meneghini, and Ermin Malic. Polaron-induced changes in moiré exciton propagation in twisted van der waals heterostructures, 2024.

[96] Fengcheng Wu, Timothy Lovorn, and AH MacDonald. Theory of optical absorption by interlayer excitons in transition metal dichalcogenide heterobilayers. *Physical Review B*, 97(3):035306, 2018.

[97] Andor Kormányos, Guido Burkard, Martin Gmitra, Jaroslav Fabian, Viktor Zólyomi, Neil D Drummond, and Vladimir Fal'ko. k· p theory for two-dimensional transition metal dichalcogenide semiconductors. *2D Materials*, 2(2):022001, 2015.

[98] Charles Kittel and Ching-yao Fong. *Quantum theory of solids*. Wiley, 1987.

[99] Robert Wallauer, Raul Perea-Causin, Lasse Münster, Sarah Zajusch, Samuel Brem, Jens Güdde, Katsumi Tanimura, Kai-Qiang Lin, Rupert Huber, Ermin Malic, et al. Momentum-resolved observation of exciton formation dynamics in monolayer ws2. *Nano Letters*, 21(13):5867–5873, 2021.

[100] Dieter Jaksch, Christoph Bruder, Juan Ignacio Cirac, Crispin W Gardiner, and Peter Zoller. Cold bosonic atoms in optical lattices. *Physical Review Letters*, 81(15):3108, 1998.

[101] Dieter Jaksch and Peter Zoller. The cold atom hubbard toolbox. *Annals of physics*, 315(1):52–79, 2005.

[102] Markus Greiner, Olaf Mandel, Tilman Esslinger, Theodor W Hänsch, and Immanuel Bloch. Quantum phase transition from a superfluid to a mott insulator in a gas of ultracold atoms. *nature*, 415(6867):39–44, 2002.

[103] Frank Ortmann, Friedhelm Bechstedt, and Karsten Hannewald. Theory of charge transport in organic crystals: Beyond holstein's small-polaron model. *Physical Review B*, 79(23):235206, 2009.

[104] Di Huang, Junho Choi, Chih-Kang Shih, and Xiaoqin Li. Excitons in semiconductor moiré superlattices. *Nature Nanotechnology*, 17(3):227–238, 2022.

[105] Long Yuan, Biyuan Zheng, Jens Kunstmann, Thomas Brumme, Agnieszka Beata Kuc, Chao Ma, Shibin Deng, Daria Blach, Anlian Pan, and Libai Huang. Twist-angle-dependent interlayer exciton diffusion in ws2–wse2 heterobilayers. *Nature materials*, 19(6):617–623, 2020.

[106] Hyobin Yoo, Rebecca Engelke, Stephen Carr, Shiang Fang, Kuan Zhang, Paul Cazeaux, Suk Hyun Sung, Robert Hovden, Adam W Tsen, Takashi Taniguchi, et al. Atomic and electronic reconstruction at the van der waals interface in twisted bilayer graphene. *Nature materials*, 18(5):448–453, 2019.

[107] Daniel Erkensten, Samuel Brem, and Ermin Malic. Exciton-exciton interaction in transition metal dichalcogenide monolayers and van der waals heterostructures. *Physical Review B*, 103(4):045426, 2021.

[108] Thomas Siday, Fabian Sandner, Samuel Brem, Martin Zizlsperger, Raul Perea-Causin, Felix Schiegl, Svenja Nerreter, Markus Plankl, Philipp Merkl, Fabian

Mooshammer, et al. Ultrafast nanoscopy of high-density exciton phases in wse2. *Nano Letters*, 22(6):2561–2568, 2022.

[109] Samuel Brem and Ermin Malic. Bosonic delocalization of dipolar moiré excitons. *Nano Letters*, 2023.

[110] Sajedeh Manzeli, Adrien Allain, Amirhossein Ghadimi, and Andras Kis. Piezoresistivity and strain-induced band gap tuning in atomically thin mos2. *Nano letters*, 15(8):5330–5335, 2015.

[111] Zhiwei Li, Yawei Lv, Liwang Ren, Jia Li, Lingan Kong, Yujia Zeng, Quanyang Tao, Ruixia Wu, Huifang Ma, Bei Zhao, et al. Efficient strain modulation of 2d materials via polymer encapsulation. *Nature communications*, 11(1):1151, 2020.

[112] Wei Wang and Xuedan Ma. Strain-induced trapping of indirect excitons in mose2/wse2 heterostructures. *ACS Photonics*, 7(9):2460–2467, 2020.

[113] Wei Li, Tianxing Wang, Xianqi Dai, Xiaolong Wang, Caiyun Zhai, Yaqiang Ma, Shanshan Chang, and Yanan Tang. Electric field modulation of the band structure in mos2/ws2 van der waals heterostructure. *Solid State Communications*, 250:9–13, 2017.

[114] Fang Zhang, Wei Li, and Xianqi Dai. Modulation of electronic structures of mose2/wse2 van der waals heterostructure by external electric field. *Solid State Communications*, 266:11–15, 2017.

Erklärung des Eigenanteils an den erfolgten Publikationen

Willy Knorr hatte folgenden Anteil an den folgenden Publikationen:

Publikation 1: **Willy Knorr**, Samuel Brem, Giuseppe Meneghini, Ermin Malic, Exciton transport in a moiré potential: from hopping to dispersive regime, Physical Review Materials, 2022

Willy Knorr: Durchführung der formalen Analyse und der allgemeinen Untersuchungen. Dazu gehören die Durchführung der numerischen Simulationen und die Interpretation der Ergebnisse. Erstellen aller Abbildungen. Darüber hinaus, schreiben sowie Review & Editing Prozess des Manuscripts/Supplemental Material.

Samuel Brem: Konzeptualisierung und direkte Supervision. Sowie Beteiligung am Schreib, Review & Editing Prozess des Papers.

Giuseppe Menephini: Unterstützung bei numerischen Simulationen sowie Beteiligung an Interpretation der Ergebnisse. Feedback zu Abbildungen.

Ermin Malic: Konzeptualisierung, Beschaffung von Fördermitteln, Projektadministration , Supervision, sowie Feedback zum Manuskript und Unterstützung im Review & Editing Prozess.

Publikation 2: **Willy Knorr**, Samuel Brem, Giuseppe Meneghini, Ermin Malic, Polaron-induced changes in moiré exciton propagation in twisted van der Waals heterostructures, Review Process

Willy Knorr: Durchführung der formalen Analyse und der allgemeinen Untersuchungen. Dazu gehören die Durchführung der numerischen Simulationen und die Interpretation der Ergebnisse. Erstellen aller Abbildungen. Darüber hinaus, schreiben sowie Review & Editing Prozess des Manuscripts/Supplemental Material.

Samuel Brem: Konzeptualisierung und direkte Supervision. Sowie Beteiligung am Schreib, Review & Editing Prozess des Papers.

Giuseppe Menephini: Unterstützung bei numerischen Simulationen sowie Beteiligung an Interpretation der Ergebnisse. Feedback zu Abbildungen.

Ermin Malic: Konzeptualisierung, Beschaffung von Fördermitteln, Projektadministration , Supervision, sowie Feedback zum Manuskript und Unterstützung im Review & Editing Prozess.

Die vorliegende Einschätzung über die erbrachte Eigenleistung wurde mit den am Artikel beteiligten Ko-Autoren/Ko-Autorinnen einvernehmlich abgestimmt.